Monthly Notices of the ROYAL ASTRONOMICAL SOCIETY

MNRAS **543,** 3503–3526 (2025) https://doi.org/10.1093/mnras/staf1311
Advance Access publication 2025 October 16

Impact of mass transfer on the orbital evolution of a white dwarf close to an intermediate-mass black hole

Yang Yang ,[1,2]★ Jie Yang ,[3,4,5,6]★ Xian Chen [1,2]★ and Zi-Han Zhang[7,8,9]

[1]*Astronomy Department, School of Physics, Peking University, Beijing 100871, China*
[2]*Kavli Institute for Astronomy and Astrophysics, Peking University, Beijing 100871, China*
[3]*School of Physical Science and Technology, Lanzhou University, Lanzhou 730000, China*
[4]*Institute of Theoretical Physics & Research Center of Gravitation, Lanzhou University, Lanzhou 730000, China*
[5]*Key Laboratory of Quantum Theory and Applications of MoE, Lanzhou University, Lanzhou 730000, China*
[6]*Lanzhou Center for Theoretical Physics & Key Laboratory of Theoretical Physics of Gansu Province, Lanzhou University, Lanzhou 730000, China*
[7]*International Centre for Theoretical Physics Asia-Pacific, University of Chinese Academy of Sciences, Beijing 100190, China*
[8]*School of Physical Sciences, University of Chinese Academy of Sciences, Beijing 100049, China*
[9]*Taiji Laboratory for Gravitational Wave Universe, University of Chinese Academy of Sciences, Beijing 100049, China*

Accepted 2025 August 5. Received 2025 July 12; in original form 2025 February 6

ABSTRACT

Extreme mass-ratio inspirals of low-mass white dwarfs (WDs; 0.1–0.3 $\mathrm{M}_{\odot}$) around spinning intermediate-mass black holes (IMBHs; 10^3–$10^5\ \mathrm{M}_{\odot}$) offer unique opportunities for multimessenger astronomy, emitting both gravitational waves (GWs) and electromagnetic signals. Yet, despite their astrophysical relevance, theoretical models often omit key interactions between relativistic dynamics and phase-dependent mass transfer (MT). In this study, we integrate a perturbed Keplerian formalism with post-Newtonian corrections to simulate the relativistic orbit of a WD around a rotating IMBH, explicitly resolving the narrow phase near pericentre where Roche-lobe overflow initiates MT. We find that GW emission and MT exert competing influences on the orbit: MT episodes can increase both orbital period and eccentricity, potentially enabling the WD to avoid complete tidal disruption and even escape. We further quantify the GW phase evolution induced by MT, identifying parameter regimes in which GW detectors could observe a 1 rad phase shift over observational time-scales. Finally, we propose that the orbital expansion driven by MT may lead to the disappearance of quasi-periodic eruptions. Our results underscore the necessity of jointly modelling relativistic effects and dynamic MT in WD–IMBH systems.

Key words: black hole physics – gravitational waves – galaxies: active – X-rays: galaxies.

1 INTRODUCTION

An extreme mass-ratio inspiral (EMRI) involves a massive black hole (MBH) and a compact object (CO), such as a white dwarf (WD), neutron star, or stellar-mass black hole (BH), moving along a tightly bound orbit around the MBH (Hils & Bender 1995; Amaro-Seoane et al. 2007). EMRIs are important sources for future space-based gravitational wave (GW) detectors, such as the Laser Interferometer Space Antenna (LISA) (Barack & Cutler 2004; Gair 2009; Berry & Gair 2012; Amaro-Seoane et al. 2017; Gair et al. 2017). Their GW signals contain rich information about the formation and evolution of stars around MBHs (Amaro-Seoane et al. 2007; Amaro-Seoane 2018), and they also offer a unique opportunity to test general relativity (GR) in the strong-gravity regime (Barsanti 2024; Speri 2024).

Among the various types of EMRIs, WDs inspiralling towards intermediate-mass black holes (IMBHs; 10^3–$10^5\mathrm{M}_{\odot}$) stand out as a special type, not only because their formation channel was recognized relatively early (Hils & Bender 1995; Freitag 2001; Bogdanović, Cheng & Amaro-Seoane 2014), but also because the end products are luminous electromagnetic (EM) flares from the tidal disruption of the WDs by the IMBHs (Luminet & Pichon 1989; Ivanov, P. B. & Papaloizou, J. C. B. 2007; Zalamea, Menou & Beloborodov 2010). Such EM counterparts associated with GW signals could enable precise measurements of the geometry of the Universe (Menou, Haiman & Kocsis 2008; Sesana et al. 2008).

King (2020) suggested that quasi-periodic eruptions (QPEs), a type of X-ray transient recently discovered (e.g. Miniutti et al. 2019; Giustini, Margherita, Miniutti, Giovanni & Saxton, Richard D. 2020; Arcodia et al. 2021; Chakraborty et al. 2021; Arcodia, R. et al. 2022; Miniutti, G. et al. 2023a, b; Arcodia, R. et al. 2024; Giustini, Margherita et al. 2024), are produced by WD–IMBH systems. QPEs are hypothesized to result from periodic mass transfer (MT) episodes involving low-mass stars on bound orbits around MBHs, where the stars narrowly avoid full tidal disruption. Several lines of reasoning suggest that low-mass WDs are particularly plausible candidates for the donor star in such systems. First, low-mass WDs are structurally favourable for producing recurrent QPEs. Their relatively large radii, governed by the mass–radius relation $R_{\mathrm{WD}} \propto M_{\mathrm{WD}}^{-1/3}$, render them

---

★ E-mail: yangjiev@lzu.edu.cn (JY); yangyang24@stu.pku.edu.cn (YY); xian.chen@pku.edu.cn (XC)

© The Author(s) 2025.
Published by Oxford University Press on behalf of Royal Astronomical Society. This is an Open Access article distributed under the terms of the Creative Commons Attribution License (https://creativecommons.org/licenses/by/4.0/), which permits unrestricted reuse, distribution, and reproduction in any medium, provided the original work is properly cited.

Downloaded from https://academic.oup.com/mnras/article/543/4/3503/8287737 by guest on 06 February 2026

more susceptible to partial tidal stripping at wider orbital separations, reducing the probability of complete disruption. This allows for repeated stable mass-loss episodes over many orbits, consistent with the observed recurrence of QPEs (Chen et al. 2022; King 2022; Krolik & Linial 2022; Wang et al. 2022; Zhao, Z. Y. et al. 2022; Linial & Sari 2023; Lu & Quataert 2023; Garain & Sarkar 2024). Secondly, main-sequence (MS) stars undergoing Roche-lobe overflow must orbit at much greater separations, leading to lower GW emission and less efficient MT (King 2022). This results in lower accretion luminosities, which may be inconsistent with the energetics inferred from QPE light curves. Thirdly, Cufari, Coughlin & Nixon (2022) demonstrated that the direct formation of QPE binaries via single scattering events involving MS stars is unlikely, as the energy dissipated in such interactions often exceeds the star's binding energy. Instead, they suggested that QPE binaries might form through the Hills (1988) mechanism, in which a stellar binary is tidally disrupted by an MBH, with one component captured and the other ejected as a hypervelocity star.

To produce a stripped mass consistent with QPE signals, the WD must have a sufficiently large radius – exceeding its corresponding Roche radius, which requires its mass to be unusually low. Specifically, the WD mass must lie well below the lower limit ($\sim 0.5\mathrm{M}_\odot$) expected from single-star evolution. The occurrence of QPEs implies a high formation rate of low-mass WDs, which likely originate from binary evolution (Istrate, A. G. et al. 2014; Chen et al. 2017; Sun & Arras 2018; Li et al. 2019). The plausible formation channels are binary stable MT and common envelope evolution. Alternatively, King (2020) proposes the possibility that an IMBH directly captures the red giant and is partially stripped away. The remaining core evolves into a low-mass WD.

However, not all the observational properties of QPEs have been explained by the WD–IMBH interaction. First, in several QPEs, the time between consecutive eruptions alternates between long and short durations (Miniutti et al. 2019). It has been suggested that this 'long-short behaviour' may result from variations in the amount of mass stripped from the WD (King 2022), but a detailed model is still lacking. Secondly, in the case of GSN 069, QPEs disappeared for about 2 yr before reappearing (Miniutti, G. et al. 2023a, b). This behaviour is not predicted by the WD–IMBH model either.

The model for QPEs drives orbits gradually inwards under the emission of GWs; however, a key prediction of this model – a secular increase in QPE luminosity due to the intensifying MT rate – appears inconsistent with long-term monitoring of sources such as GSN 069, where no significant brightening has been observed. To address this discrepancy, Wang, Di (2024) proposed a hybrid scenario in which tidal stripping is coupled with dynamical interactions between the WD and a remnant accretion disc formed by a preceding TDE. In this framework, the WD intersects the fallback disc during its orbit, and the resulting hydrodynamical drag moderates the MT rate. This interaction not only prevents the WD from undergoing rapid disruption, but also enables the system to maintain a relatively stable QPE luminosity. Despite its promise, the detailed impact of WD–disc interactions remains poorly constrained, particularly across a wide range of orbital eccentricities and disc configurations. Furthermore, not all QPE-hosting systems are expected to retain a disc, and mutual inclination between the disc plane and the binary orbit is likely. Given the inherent complexity and transient nature of post-TDE accretion structures, we focus in this work on exploring the long-term evolution of WD–IMBH binaries in the absence of a disc, with the aim of systematically evaluating the effectiveness and generality of the MT mechanism across a broad parameter space.

Our study is motivated by key limitations in current models of QPEs involving WD–IMBH systems, particularly the incomplete treatment of relativistic orbital dynamics and the MT process. These prevents direct comparisons of model predictions with observed QPE light curves.

First, the effects of GR have not been fully accounted for. What has been included in the model (e.g. Zalamea et al. 2010; King 2020) is the secular decay of the orbital semimajor axis and eccentricity due to GW radiation, but the derivation of the formulae is based on the Keplerian orbit approximation (Peters 1964). Such a model fails to capture the relativistic precession of the orbital pericentre or the variation in the orientation of the orbital angular momentum due to frame dragging if the central IMBH is spinning. These effects could introduce new characteristic frequencies into the orbit of the WD, as well as change our viewing angle of the system. Hence, they may be important for explaining the occurrence times or luminosities of the eruptions. The relevance of these effects is corroborated by the high orbital eccentricities (i.e. small pericentre distances) inferred for the WD orbits in QPEs (Chen et al. 2022; King 2022, 2023).

We need to capture relativistic corrections over each orbital cycle, and can attach MT in the form of force together. The post-Newtonian (PN) form and the perturbed Kepler method (Efroimsky 2005; Poisson & Will 2014) provide a good way to do this. The PN expansion introduces relativistic acceleration terms that modify key orbital elements – including the semimajor axis, eccentricity, and orbital phase. These modifications are naturally embedded within the perturbed Keplerian formalism, which yields a set of coupled differential equations describing the time evolution of orbital parameters. Crucially, differential equations allows us to incorporate external perturbative forces, such as those arising from asymmetric MT (Wang, Di 2024).

Secondly, MT from the WD to the IMBH is inevitable and is suspected to be responsible for stabilizing the long-term evolution of the binary (King 2022). However, the detailed mechanism remains unclear. Recent studies Wang et al. (2022) and King (2020, 2022, 2023) use the orbital-averaged dynamical equations derived for stellar binaries (Sepinsky, Kalogera & Rasio 2007b) to model the secular evolution of a WD–IMBH binary. But the analyses from Sepinsky, Willems & Kalogera (2007a) and Sepinsky et al. (2007b) did not focus on the EMRI system, and the discussion of angular momentum transfer is not sufficient. Since MT in the WD–IMBH scenario occurs mainly at pericentre due to the aforementioned high eccentricity, the validity of the orbital average remains unverified.

Because high-eccentricity WD–IMBH systems are highly dependent on rapid phase changes, the Roche lobe overflow of MT occurs only in a narrow phase window near pericentre. We need a dynamics treatment that is suitable for handling changes within the concentrated phase range. Sepinsky et al. (2007b) provide a method to treat high-eccentricity accretion dynamics, modelling this behaviour by treating the MT rate as a spike function near pericentre. The MT rate is expressed as a power-law expansion of the difference between the WD radius and the instantaneous Roche lobe radius, thus achieving a continuous and differentiable dynamical description.

MT process is expected to exert a dynamical influence on the orbital evolution of a WD–IMBH system. In particular, the anisotropic ejection of matter from the donor can impart a recoil force, which may become comparable to – or under certain conditions even exceed – the backreaction from GW emission. Although GW radiation typically drives orbital circularization and inspiral, the MT-induced force can act in the opposite direction, potentially increasing the semimajor axis or enhancing orbital eccentricity. These considerations suggest a potentially rich interplay between GW-driven contraction and

Downloaded from https://academic.oup.com/mnras/article/543/4/3503/8287737 by guest on 06 February 2026

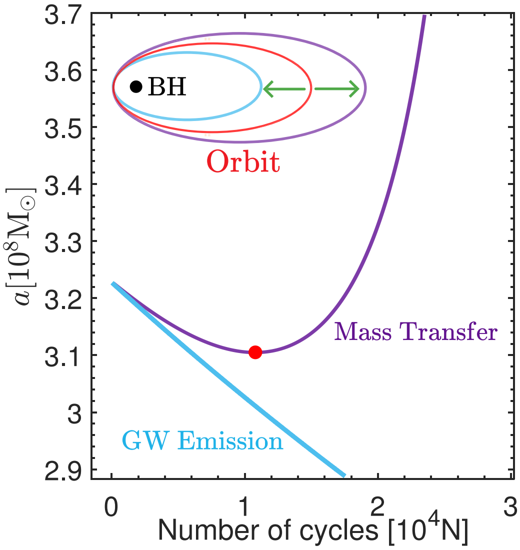

Figure 1. Simulation result of semimajor axis in a high eccentricity WD–IMBH system. The mass of the WD is $0.15\mathrm{M}_\odot$ and the mass of the IMBH is $4 \times 10^5\mathrm{M}_\odot$; the initial eccentricity is 0.99. A more detailed diagram can be seen in Fig. 8.

MT-driven expansion in high-eccentricity EMRIs. The interaction between these competing effects is likely to affect the orbital evolution as shown in Fig. 1. In the late stages of binary evolution, the MT force is likely to exceed the gravitational reaction force, which can be expected to lead to the dynamical ejection of the WD from the gravitational potential of the IMBH.

This paper is structured as follows. In Section 2, using the perturbed Kepler method, we describe the motion of the WD in the IMBH's relative coordinate system. We assume that all acceleration terms can be expressed in terms of the required parameters. In Section 3, we introduce the WD state formulae (Zalamea et al. 2010), the MT Roche lobe accretion model (Kolb & Ritter 1990; Sepinsky et al. 2007a; Cehula & Pejcha 2023), and the dynamics of eccentric binaries under MT (Sepinsky et al. 2007b). In Section 4, we introduce the initial angular parameter representation, aligning the spin angular momentum of the IMBH with the z-axis in a fixed Cartesian coordinate system, and then numerically compute the short-term orbital evolution using the PN method and the perturbed Kepler method with MT. In Section 5, we analyse the combined effects of MT and gravitational radiation on the long-term orbital evolution, using the time-averaged rate of change over one period. We describe the orbital evolution starting from the point where the Roche lobe radius at pericentre equals the WD radius. In Section 6, for the GW signal, we compute the time required for the orbital phase to change by 1 rad due to the MT effect, and identify the initial parameters that enable the detection of phase differences within 5 yr. In Sections 7and 8, we discuss and summarize our results.

2 THEORY OF ORBITAL DYNAMICS

2.1 The general form of relative acceleration

In this study, we model the orbital dynamics of a WD–IMBH binary system by treating both relativistic corrections and MT effects as perturbations to the classical Newtonian two-body problem. The relative acceleration between the WD and the IMBH is thus expressed as

$$\boldsymbol{a} = \frac{\mathrm{d}\boldsymbol{v}}{\mathrm{d}t} = -\frac{Gm}{r^2}\boldsymbol{n} + \boldsymbol{f}, \tag{1}$$

where $\boldsymbol{a} = \boldsymbol{a}_1 - \boldsymbol{a}_2$ denotes the relative acceleration of the WD with respect to the IMBH, $m = m_1 + m_2$ is the total mass of the system, and m_1 and m_2 are the masses of the WD and the IMBH, respectively. The vector $\boldsymbol{f}$ represents the perturbative accelerations arising from relativistic corrections and MT effects. To facilitate a systematic perturbative analysis, $\boldsymbol{f}$ is decomposed into components along a natural orthonormal triad: $\boldsymbol{f} = \mathcal{R}\boldsymbol{n} + \mathcal{S}\boldsymbol{\lambda} + \mathcal{W}\boldsymbol{\ell}$. Here, $\boldsymbol{n} = \boldsymbol{r}/r$ is the unit vector of the binary star relative position vector, $\boldsymbol{\ell} = \boldsymbol{n} \times \boldsymbol{v}/\,|\boldsymbol{n} \times \boldsymbol{v}|$ is the unit vector normal to the orbital plane, and $\boldsymbol{\lambda} = \boldsymbol{\ell} \times \boldsymbol{n}$ lies within the orbital plane. This decomposition provides a convenient basis for quantifying the secular evolution of orbital elements under the influence of the perturbing forces.

The relativistic motion of point particles in the system is described using a modified geodesic equation, following the PN formalism outlined by Blanchet (2024). The Newtonian-like equations of motion (EOMs) for individual bodies are provided in their equation (339), while the EOM governing the relative dynamics of the two-body system is given in their equation (357).

To incorporate spin effects, we adopt the treatment of Tagoshi, Ohashi & Owen (2001) for the case in which body A possesses spin angular momentum $\boldsymbol{S}_\mathrm{A}$. In their formalism, the relative acceleration $\boldsymbol{a}$ includes contributions from the spin–orbit coupling term $\boldsymbol{a}_\mathrm{SO}$, the spin–spin interaction term $\boldsymbol{a}_\mathrm{SS}$, and the PN spin–orbit correction $\boldsymbol{a}_\mathrm{SOPN}$, as given in their equation (5.15). The evolution of the spin vector is governed by the spin precession equation (their equation 2.17).

In addition to the relativistic and spin effects, we include the influence of MT through an additional acceleration term $\boldsymbol{f}_\mathrm{MT}$, provided in equation (14) of Sepinsky et al. (2007b). A detailed formulation and discussion of this term will be presented in Section 3.3.

Combining the above considerations, the total perturbative acceleration $\boldsymbol{f}$ is given by

$$\boldsymbol{f} = -\frac{Gm}{r^2}(\mathcal{A}\boldsymbol{n} + \mathcal{B}\boldsymbol{v}) + \boldsymbol{a}_\mathrm{SO} + \boldsymbol{a}_\mathrm{SS} + \boldsymbol{a}_\mathrm{SOPN} + \boldsymbol{f}_\mathrm{MT} + \mathcal{O}(c^{-8}), \tag{2}$$

where $\mathcal{A}$ and $\mathcal{B}$ are functions of $\boldsymbol{r}$ and $\boldsymbol{v}$, given in equations (358) and (359) of Blanchet (2024). To fully describe the system's dynamics, we also consider the spin precession equations (equation 2.17 of Tagoshi et al. 2001) and the evolution of mass m_1 and m_2 due to MT. A comprehensive set of calculation parameters and further details will be provided in the subsequent section. This framework enables a detailed analysis of the orbital dynamics of WD–IMBH systems, accounting for both relativistic effects and MT processes.

2.2 Perturbed Kepler method

To characterize the relative motion between the WD and the IMBH, we adopt a coordinate system as illustrated in Fig. 2, utilizing the orbital angles (ϕ, f, ω, Ω, ι) as defined by Poisson & Will (2014), to describe the relative motion between the WD and the IMBH.

For the unperturbed Keplerian orbit ($\boldsymbol{f} = \boldsymbol{0}$), the orbital plane remains fixed without precession, implying that $\dot{\Omega} = \dot{\iota} = \dot{\omega} = 0$ and

Downloaded from https://academic.oup.com/mnras/article/543/4/3503/8287737 by guest on 06 February 2026

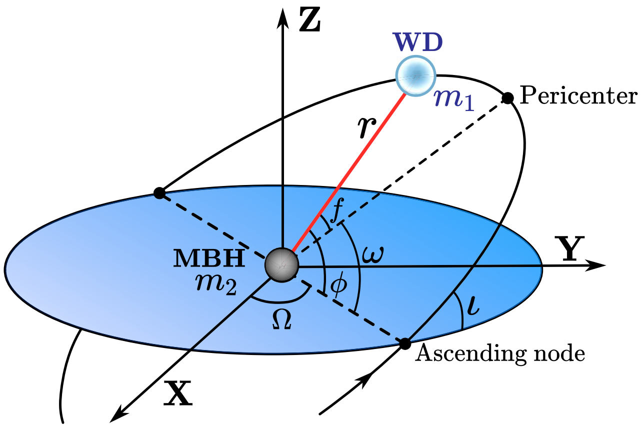

Figure 2. Definition of the relative coordinate and the angle parameters. The origin of the relative coordinate system is placed at mass m_2, while mass m_1 follows an orbit defined by $\boldsymbol{r} = r^X \boldsymbol{e}_X + r^Y \boldsymbol{e}_Y + r^Z \boldsymbol{e}_Z$. For a quasi-Keplerian orbit, the system has pericentre and an ascending node, where the ascending node is the point of intersection of the orbit with the OXY plane. The parameters are as follows: ι is the inclination of the orbital plane relative to the OXY plane; Ω is the longitude of the ascending node, the angle between the ascending node and the positive x-axis; ω is the argument of pericentre, the angle between the ascending node and the pericentre; f is the phase angle of m_1 relative to the pericentre. The angle ϕ is defined as $\phi = \omega + f$. The basis vectors $\boldsymbol{e}_X$, $\boldsymbol{e}_Y$, $\boldsymbol{e}_Z$ define the Cartesian coordinate system with coordinates (X, Y, Z).

$\dot{\phi} = \dot{f}$. The classical Keplerian EOM are then given by

$$\begin{aligned} r &= \frac{p}{1 + e\cos f}, \\ \dot{r} &= \sqrt{\frac{Gm}{p}}\, e \sin f, \quad \dot{\phi} = \sqrt{\frac{Gm}{p^3}} \left(1 + e\cos f\right)^2, \\ v^2 &= \frac{Gm}{p}\left[e^2 \sin^2 f + (1 + e\cos f)^2\right], \end{aligned} \tag{3}$$

where p is the semilatus rectum and e is the eccentricity.

In the presence of perturbative accelerations ($\boldsymbol{f} \neq \boldsymbol{0}$), we propose that the Keplerian EOM (3) remains unchanged, but the orbital elements (p, e, f, ω, Ω, ι) evolve over time. The evolution of these parameters is governed by the components ($\mathcal{R}$, $\mathcal{S}$, $\mathcal{W}$) in the perturbation acceleration $\boldsymbol{f}$. The differential equations for the orbital elements follow the formalism presented in Poisson & Will (2014):

$$\frac{\mathrm{d}p}{\mathrm{d}t} = \sqrt{\frac{p}{Gm}} \frac{2p}{1+e\cos f} \mathcal{S}, \tag{4a}$$

$$\frac{\mathrm{d}e}{\mathrm{d}t} = \sqrt{\frac{p}{Gm}} \left[\sin f \mathcal{R} + \frac{2\cos f + e\left(1+\cos^2 f\right)}{1+e\cos f} \mathcal{S}\right], \tag{4b}$$

$$\begin{aligned} \frac{\mathrm{d}f}{\mathrm{d}t} = {} & \sqrt{\frac{Gm}{p^3}} (1 + e\cos f)^2 \\ & + \sqrt{\frac{p}{Gm}} \frac{1}{e} \left[\cos f \mathcal{R} - \frac{2 + e\cos f}{1 + e\cos f} \sin f \mathcal{S}\right], \end{aligned} \tag{4c}$$

$$\begin{aligned} \frac{\mathrm{d}\omega}{\mathrm{d}t} = {} & \sqrt{\frac{p}{Gm}} \frac{1}{e} \left[-\cos f \mathcal{R} + \frac{2+e\cos f}{1+e\cos f} \sin f \mathcal{S} \right. \\ & \left. - \cot\iota \frac{e\sin(\omega+f)}{1+e\cos f} \mathcal{W}\right], \end{aligned} \tag{4d}$$

$$\frac{\mathrm{d}\Omega}{\mathrm{d}t} = \sqrt{\frac{p}{Gm}} \frac{\sin(\omega+f)}{1+e\cos f} \csc\iota \; \mathcal{W}, \tag{4e}$$

$$\frac{\mathrm{d}\iota}{\mathrm{d}t} = \sqrt{\frac{p}{Gm}} \frac{\cos(\omega+f)}{1+e\cos f} \mathcal{W}. \tag{4f}$$

To express the evolution of the spin angular momentum vector within the natural orthonormal triad ($\boldsymbol{n}$, $\boldsymbol{\lambda}$, $\boldsymbol{\ell}$), we derive the time derivatives of these basis vectors, incorporating the effects of relativistic precession. This approach facilitates the projection of spin dynamics onto the orbital frame, which is particularly advantageous for analysing systems with eccentric orbits and spin-orbit coupling. The time derivatives of the basis vectors are given by

$$\dot{\boldsymbol{n}} = \dot{f}_{\mathrm{N}} \boldsymbol{\lambda}, \quad \dot{\boldsymbol{\lambda}} = -\dot{f}_{\mathrm{N}} \boldsymbol{n} + \dot{f}_{\mathrm{N}} \mathcal{W}_f \boldsymbol{\ell}, \quad \dot{\boldsymbol{\ell}} = -\dot{f}_{\mathrm{N}} \mathcal{W}_f \boldsymbol{\lambda}, \tag{5}$$

where

$$\dot{f}_{\mathrm{N}} := \sqrt{\frac{Gm}{p^3}} \left(1 + e\cos f\right)^2, \quad \mathcal{W}_f := \frac{p^2 \mathcal{W}}{Gm \left(1 + e\cos f\right)^3}. \tag{6}$$

Here, $\dot{f}_{\mathrm{N}}$ has the same form as $\dot{\phi}$ in equation (3). Introducing the dimensionless parameter $\mathcal{W}_f$ facilitates the simplification of equation (5) in scenarios where $\mathcal{W} \neq 0$. Equation (5) enables the decomposition of the spin precession equation into components aligned with the natural basis, thereby allowing for a detailed analysis of the spin dynamics influenced by relativistic corrections.

The spin angular momentum $\boldsymbol{S}_{\mathrm{A}}$ ($\mathrm{A} = 1, 2$) can be expressed as $S_{\mathrm{A}n}\boldsymbol{n} + S_{\mathrm{A}\lambda}\boldsymbol{\lambda} + S_{\mathrm{A}\ell}\boldsymbol{\ell}$. We obtain the differential equations for the spin components $S_{\mathrm{A}n}$, $S_{\mathrm{A}\lambda}$, and $S_{\mathrm{A}\ell}$:

$$\frac{\mathrm{d}S_{\mathrm{A}n}}{\mathrm{d}t} = (\boldsymbol{\Omega}_{\mathrm{A}} \times \boldsymbol{S}_{\mathrm{A}})_n + \dot{f}_{\mathrm{N}} S_{\mathrm{A}\lambda}, \tag{7a}$$

$$\frac{\mathrm{d}S_{\mathrm{A}\lambda}}{\mathrm{d}t} = (\boldsymbol{\Omega}_{\mathrm{A}} \times \boldsymbol{S}_{\mathrm{A}})_\lambda - \dot{f}_{\mathrm{N}} S_{\mathrm{A}n} + \dot{f}_{\mathrm{N}} \mathcal{W}_f S_{\mathrm{A}\ell}, \tag{7b}$$

$$\frac{\mathrm{d}S_{\mathrm{A}\ell}}{\mathrm{d}t} = (\boldsymbol{\Omega}_{\mathrm{A}} \times \boldsymbol{S}_{\mathrm{A}})_\ell - \dot{f}_{\mathrm{N}} \mathcal{W}_f S_{\mathrm{A}\lambda}, \tag{7c}$$

where $\boldsymbol{\Omega}_{\mathrm{A}}$ denotes the rates at which the spin angular momentum rotates around the total angular momentum.

Therefore, a comprehensive set of differential equations governing the dynamics of the inspiralling binary system with the MT process can be derived. This includes the following variables:

$$\left\{\dot{p}, \dot{e}, \dot{f}, \dot{\omega}, \dot{\Omega}, \dot{\iota}, \dot{S}_{1n}, \dot{S}_{1\lambda}, \dot{S}_{1\ell}, \dot{S}_{2n}, \dot{S}_{2\lambda}, \dot{S}_{2\ell}, \dot{m}_1, \dot{m}_2\right\}.$$

3 MT FOR ECCENTRIC BINARY

To complete the orbital evolution analysis of the WD–IMBH system, we incorporate the MT rate ($\dot{m}_1$, $\dot{m}_2$) and the associated perturbative acceleration $\boldsymbol{f}_{\mathrm{MT}}$. In our study of the mass stripping of WD, we utilize the WD model proposed by Zalamea et al. (2010) to characterize the surface properties of the WD in Section 3.1. The MT rate $\dot{m}_1$ is introduced in Section 3.2 following theory outlined by Kolb & Ritter (1990), Jackson et al. (2017), and Cehula & Pejcha (2023). Our application of the Lagrangian point L1 and its corresponding equivalent Roche radius refers to Sepinsky et al. (2007a). To calculate $\boldsymbol{f}_{\mathrm{MT}}$, we use the analysis of the conservation of orbital angular momentum derived in Section 3.3. We extend this analysis to the case where it may not be conserved.

3.1 Hydrostatic equilibrium model of WD

In the following text, we assume that the polytropic equation of state (EOS) for the surface layer of the WD is $P = K\rho^{\Gamma}$, where $\Gamma = 5/3$ and $K \equiv (3/\pi)^{2/3} h^2 / 20 m_{\mathrm{e}} \left(\mu_{\mathrm{e}} m_{\mathrm{p}}\right)^{5/3}$. Here, h is the Planck constant, m_{e} is the electron mass, m_{p} is the proton mass, and $\mu_{\mathrm{e}} \approx 2$ is the mean molecular weight per electron. The WD's radius can be expressed as (Zalamea et al. 2010):

$$R_{\mathrm{WD}}(M_{\mathrm{WD}}) \approx 6120 \frac{G\mathrm{M}_{\odot}}{c^2} \left(\frac{M_{\mathrm{WD}}}{M_{\mathrm{Ch}}}\right)^{-1/3} \left(1 - \frac{M_{\mathrm{WD}}}{M_{\mathrm{Ch}}}\right)^{0.447}, \tag{8}$$

Downloaded from https://academic.oup.com/mnras/article/543/4/3503/8287737 by guest on 06 February 2026

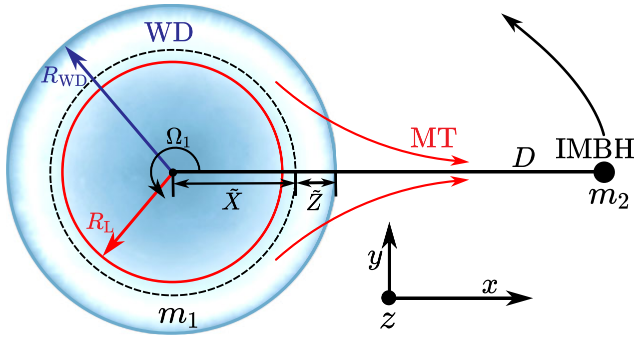

Note: Figure not drawn to scale.

Figure 3. The top view of the instantaneous orbital plane. The directions of x, y, z are determined by the line connecting the CM and the rotation axis of WD. The donor (WD) has mass m_1, and the accretor (IMBH) has mass m_2. The parameters are as follows: $R_{\rm WD}$ is the radius of WD, $R_{\rm L}$ is the Roche-lobe radius. $\tilde{Z}$ is the depth beneath the donor surface, $\tilde{X} = R_{\rm WD} - \tilde{Z}$ is the distance from the CM of the donor to the mass element, D is the distance from the CM of the donor to the accretor, and Ω_1 is the spin angular velocity of the donor. The Schwarzschild radius of the IMBH is much larger than the WD radius, so it is not drawn to scale.

where $M_{\rm Ch}$ is the Chandrasekhar mass.

Assuming a quasi-static equilibrium and incorporating tidal and rotational potentials, the modified hydrostatic equilibrium equation can be integrated using the polytropic EOS. Applying the boundary condition at the photosphere yields the following density distribution:

$$\begin{aligned}\rho^{\Gamma-1}(\tilde{Z}) = \rho_{\rm ph}^{\Gamma-1} + \frac{\Gamma-1}{K\Gamma}\Bigg\{&\frac{Gm_1}{R_{\rm WD}}\left(\frac{R_{\rm WD}}{R_{\rm WD}-\tilde{Z}} - 1\right)\\ &-\frac{1}{2}\Omega_1^2(2R_{\rm WD}-\tilde{Z})\tilde{Z}\\ &+\frac{Gm_2}{D}\left[\frac{\tilde{Z}}{D} + \frac{D}{D-R_{\rm WD}+\tilde{Z}} - \frac{D}{D-R_{\rm WD}}\right]\Bigg\},\end{aligned} \tag{9}$$

where $(m_1, m_2, R_{\rm WD}, D, \tilde{Z}, \tilde{X}, \Omega_1)$ are described in Fig. 3.

The surface (photosphere) density $\rho_{\rm ph}$ of a WD is challenging to determine directly due to the presence of an overlying non-degenerate atmosphere. This parameter is influenced by factors such as metallicity, evolutionary stage, boundary conditions, and the EOS (Cehula & Pejcha 2023). To facilitate analysis, we introduce a dimensionless surface equivalent depth, ξ_0, as an adjustable parameter:

$$\rho_{\rm ph} := \left[\frac{\Gamma-1}{K\Gamma}\left(\frac{GM_{\rm WD}}{R_{\rm WD}}\frac{\xi_0}{1-\xi_0}\right)\right]^{\frac{1}{\Gamma-1}}. \tag{10}$$

This formulation equates $\rho_{\rm ph}$ to the density at a depth $\tilde{Z} = \xi_0 R_{\rm WD}$ in a non-rotating WD absent tidal effects, providing a convenient framework for subsequent mathematical treatments. Observational data indicate that the outermost layers of WDs possess relatively low densities, typically ranging from 10^{-5} to $10^{-3}\,{\rm g\,cm^{-3}}$ (Seymour 1984; Ritter 1988). We posit that this tenuous atmosphere is stripped away before the WD reaches pericentre and is not replenished within a single orbital cycle. Consequently, the exposed surface comprises a denser hydrogen or helium layer, with densities estimated between 10 and $10^4\,{\rm g\,cm^{-3}}$ (Seymour 1984). While a minimum density of $10\,{\rm g\,cm^{-3}}$ is considered, the actual value is likely substantially higher. Using equation (8), the parameter ξ_0 can be estimated as

$$\begin{aligned}\xi_0 &= \frac{P_{\rm ph}/\rho_{\rm ph}}{c^2}\frac{R_{\rm WD}}{GM_{\rm WD}/c^2}\frac{\Gamma}{\Gamma-1}\\ &\approx 3.5\times10^{-3}\left(\frac{\rho_{\rm ph}}{10\,{\rm g\,cm^{-3}}}\right)^{2/3}\left(\frac{M_{\rm WD}}{0.15\,{\rm M_\odot}}\right)^{-4/3}.\end{aligned} \tag{11}$$

This estimation provides a practical means to relate the surface density to the structural parameters of the WD, facilitating further analysis of MT processes in WD–IMBH systems.

3.2 MT model

With the density distribution of the WD, the transferred mass rate from the WD to the IMBH can be determined. Following the framework established by Cehula & Pejcha (2023), we divide the MT process over one orbital period into two phases: isothermal (optically thin) and adiabatic (optically thick) accretion. The transition between these two phases is continuous and is related to the Roche radius $R_{\rm L}$ of the Roche lobe model.

If the donor (WD) is Roche-lobe underfilling ($R_{\rm WD} < R_{\rm L}$), the MT stream is isothermal (Lubow & Shu 1975; Ritter 1988; Jackson et al. 2017). The prescription assumes that, even if $R_{\rm WD} < R_{\rm L}$, the density profile of donor's atmosphere extends above its photosphere to the first Lagrange point L1. The gas above the photosphere is optically thin to radiation from the donor, but is in equilibrium with the surrounding radiation field (Cehula & Pejcha 2023). After the gas passes through L1, it accretes supersonically on to the accretor (Lubow & Shu 1975). Conversely, if the donor is Roche-lobe overflowing ($R_{\rm WD} > R_{\rm L}$), the MT is optically thick and adiabatic (Kolb & Ritter 1990; Pavlovskii & Ivanova 2015; Marchant, Pablo et al. 2021). It is assumed that there is no energy transport within the gas and between the gas and the surrounding radiation field.

According to our considerations, we first give the formula for the MT rate we use. When $R_{\rm WD} < R_{\rm L}$, the Roche lobe is underfilling, the MT rate is

$$\dot{m}_1^{\rm iso} = -\frac{2\pi}{\sqrt{BC}}\frac{\rho_{\rm ph}}{\exp(1/2)}c_{\rm T}^3\cdot\exp\left(-\frac{\phi_1-\phi_{\rm ph}}{c_{\rm T}^2}\right). \tag{12}$$

When $R_{\rm WD} > R_{\rm L}$, the MT rate is

$$\dot{m}_1^{\rm adi} = -\frac{2\pi}{\sqrt{BC}}\left\{\frac{\rho_{\rm ph}}{\exp(1/2)}c_{\rm T}^3 + F(K,\Gamma)\left(P_{\rm L}^{\frac{3\Gamma-1}{2\Gamma}} - P_{\rm ph}^{\frac{3\Gamma-1}{2\Gamma}}\right)\right\}. \tag{13}$$

We begin to explain the physical quantities involved in equations (12) and (13), as detailed in Cehula & Pejcha (2023). Here, the surface density $\rho_{\rm ph}$ is determined by equation (10), while the sound speed $c_{\rm T}$ is given by $c_{\rm T}^2 = \Gamma P_{\rm ph}/\rho_{\rm ph}$. In equation (12), ϕ_1 represents the specific potential at the Lagrange point L1 within the rotating frame, and $\phi_{\rm ph}$ corresponds to the potential at the WD's surface. Both points lie along the line connecting the centre of mass (CM) of the binary components. The position of L1, accounting for orbital eccentricity and asynchronous rotation, can be determined following the methodology of Sepinsky et al. (2007a). Equation (13) involves the pressures $P_{\rm L} = P\left(\tilde{Z} = R_{\rm WD} - R_{\rm L}\right)$ and $P_{\rm ph} = P\left(\tilde{Z} = 0\right)$. The corresponding density profile is described by equation (9). The factor $2\pi/\sqrt{\rm BC}$ arises from the three-dimensional expansion of the effective potential near L1. The coefficients B and C define the effective cross-sectional area through which MT occurs; they satisfy (Cehula & Pejcha 2023)

$$\phi = \phi^x(x) + \frac{B}{2}y^2 + \frac{C}{2}z^2 + \mathcal{O}\left(y^3, z^3\right), \tag{14}$$

Downloaded from https://academic.oup.com/mnras/article/543/4/3503/8287737 by guest on 06 February 2026

where x represents the distance from point L1 on the line connecting the CM, i.e. $x = \tilde{X} - \tilde{X}_1 D$. Here, y and z are shown in Fig. 3. The function $F(K, \Gamma)$, dependent on K and Γ, is expressed as

$$F(K, \Gamma) = K^{\frac{1}{2\Gamma}} \left(\frac{2}{\Gamma + 1}\right)^{\frac{\Gamma+1}{2(\Gamma-1)}} \left(\frac{2\Gamma^{3/2}}{3\Gamma - 1}\right). \tag{15}$$

While we delineate the MT rate into isothermal and adiabatic phases, the transition between these regimes is inherently continuous. This continuity ensures that $\dot{m}_1^{\rm iso} = \dot{m}_1^{\rm adi}$ precisely when the WD's radius equals its Roche lobe radius ($R_{\rm WD} = R_{\rm L}$), thereby maintaining a smooth MT rate across the transition. Notably, near pericentre in highly eccentric orbits, the adiabatic MT rate significantly exceeds the isothermal rate at the point where $R_{\rm WD} = R_{\rm L}$, i.e. $\dot{m}_1^{\rm adi}(r_{\rm p}) \gg \dot{m}_1^{\rm iso}(R_{\rm WD} = R_{\rm L})$. Conversely, at orbital phases far from pericentre, where $(\phi_1 - \phi_{\rm ph})/c_{\rm T}^2 \gg 1$, the exponential term in equation (12) diminishes towards zero, rendering the MT rate negligible.

So far, we have given complete expression for the MT rate. However, to accurately determine the onset of MT, it is essential to evaluate the Roche lobe radius $R_{\rm L}$ of WD. The Roche lobe radius can be written as $R_{\rm L} = f(A, q)\, D$, where $f(A, q)$ is a dimensionless function of $A = \Omega_1^2 D^3/Gm$ and the mass ratio is $q = m_1/m_2$. The factor A represents the ratio of the centrifugal potential by self-rotation to the gravitational potential. In the specific context of a WD donor in a highly eccentric orbit around an IMBH, the spin angular velocity Ω_1 of the WD is typically negligible compared to the orbital angular velocity at pericentre. This condition implies $A \to 0$ at pericentre, satisfying $\Omega_1 r_{\rm p}/c \ll \sqrt{{\rm R_s}/r_{\rm p}}$. Under this approximation, $f(A, q)$ can be expanded to zeroth-order in A, yielding

$$f(A, q) = \frac{0.5439 - 0.0245 \exp\left[-(0.5 + \log_{10} q)^2\right]}{0.6 + \ln\left(1 + q^{1/3}\right) q^{-2/3}} + \mathcal{O}(A). \tag{16}$$

The fitting formula used to expand to get equation (16) is the equation (48) of Sepinsky et al. (2007a). This expression offers a refined estimate of the Roche lobe radius, accounting for the effects of asynchronism and orbital eccentricity, and is particularly applicable to systems where the donor's rotation is significantly slower than the orbital motion.

3.3 Dynamics under MT

Now, only $\boldsymbol{f}_{\rm MT}$ remains undecided. We analyse from the perspective of the conservation and redistribution of orbital angular momentum $J_{\rm orb}$ (King 2020, 2022). MT results in the formation of an accretion disc, or the angular momentum might be lost from the system. Orbital angular momentum loss also occurs when binary total mass conservation. Part of the angular momentum of the ejected/accreted mass may be transferred to the donor/accretor's spin angular momentum.

To account for both conservative and non-conservative MT processes, we introduce two functions, $\tilde{f}$ and $\tilde{g}$, representing these distinct influences. We define the orbital angular momentum loss due to MT as

$$\frac{\dot{J}_{\rm orb}}{J_{\rm orb}} := \gamma \tilde{f}(\alpha, q, \gamma) \frac{\dot{m}_1}{m_1} + (1 - \gamma) \tilde{g}(\beta, q, \gamma) \frac{\dot{m}}{m}. \tag{17}$$

The functions $\tilde{f}(\alpha, q, \gamma)$ and $\tilde{g}(\beta, q, \gamma)$ represent $J_{\rm orb}$ loss for conservative and non-conservative MT processes, respectively. The constants α and β control the $J_{\rm orb}$ loss in these functions. These functions satisfy the conditions $\tilde{f}(0, q, \gamma) = \tilde{g}(0, q, \gamma) = 0$, indicating no $J_{\rm orb}$ loss when α and β vanish.

Now, we start to derive the component of the $\boldsymbol{f}_{\rm MT}$. Using the definition $J_{\rm orb} = m\eta\sqrt{Gmp}$, where $\eta = m_1 m_2/m^2$. The time derivative of $J_{\rm orb}$ can be expressed as

$$\frac{\dot{J}_{\rm orb}}{J_{\rm orb}} = \frac{\dot{m}_1}{m_1} + \frac{\dot{m}_2}{m_2} - \frac{1}{2}\frac{\dot{m}}{m} + \sqrt{\frac{r}{Gm(1 + e\cos f)}}\mathcal{S}, \tag{18}$$

where $\mathcal{S}$ arises from ${\rm d}p/{\rm d}t$ in equation (4a). Here, $\dot{m}_1$ and $\dot{m}_2$ are from ${\rm d}\eta/{\rm d}t$. In addition, based on the previous assumptions for $\dot{m}_2 = -\gamma \dot{m}_1$, we can rewrite these mass derivative using γ and q,

$$\frac{\dot{m}_1}{m_1} + \frac{\dot{m}_2}{m_2} - \frac{1}{2}\frac{\dot{m}}{m} = \frac{\dot{m}_1}{m_1}\frac{2(1 - \gamma q^2) + q(1 - \gamma)}{2(1 + q)}. \tag{19}$$

Equation (18) represents a generalized expression determined by the system's intrinsic parameters, while equation (17) serves as an additional relation capturing the possible non-conservation of $J_{\rm orb}$ induced by MT. These two equations are inherently independent. By equating their right-hand sides and expressing $\dot{m}_2$ and $\dot{m}$ in terms of γ, q, and $\dot{m}_1$, we can formulate the function $\mathcal{S}$. This function represents the component of the MT-induced force $\boldsymbol{f}_{\rm MT}$ along the direction $\boldsymbol{\lambda}$ and can be expressed as a function of q, γ, $\tilde{f}$, and $\tilde{g}$:

$$\begin{aligned}\mathcal{S} &= \left(-\frac{\dot{m}_1}{m_1}\right) r\dot{f}_{\rm N}\left\{\frac{2(1 - \gamma q^2) + q(1 - \gamma)[1 - 2(1 - \gamma)\tilde{g}]}{2(1 + q)} - \gamma\tilde{f}\right\} \\ &:= \left(-\frac{\dot{m}_1}{m_1}\right) r\dot{f}_{\rm N}(1 - q)\tilde{h}(q, \gamma, \alpha, \beta). \end{aligned} \tag{20}$$

For $\gamma = 1$ and $\alpha = 0$, corresponding to mass conservation ($\dot{m} = 0$) and no $J_{\rm orb}$ loss (i.e. the right-hand side of equation 17 is zero), we find $\tilde{h}(q, 1, 0, \beta) = 1$, consistent with previous results. Therefore, equation (20) gives the dynamics of the MT effect.

However, using the analysis of orbital angular momentum only provides the acceleration in the direction of $\boldsymbol{\lambda}$ for the MT process, because $\dot{J}_{\rm orb}/J_{\rm orb}$ in equation (18) only have the function $\mathcal{S}$. The form of $\mathcal{R}$ in the radial direction $\boldsymbol{n}$ cannot be derived from orbital angular momentum (equation 18).

For the following reasons, we can assume that the MT process does not induce acceleration in the radial direction. Because the orbit has high eccentricity, the MT process occurs exclusively at pericentre, i.e. $\dot{m}_1 \propto \delta(f)$, then $\mathcal{R}$ does not need to be determined. This is because the coefficient of $\mathcal{R}$ in ${\rm d}e/{\rm d}t$ in equation (4b) contains $\sin f$, which vanishes at $f = 0$, and is an odd function. In addition, according to equation (4), for the pericentre distance variation, $\dot{r}_{\rm p} = \left(\dot{p} - \dot{e}\, r_{\rm p}\right)\left(r_{\rm p}/p\right)$, it is

$$\frac{{\rm d}r_{\rm p}}{{\rm d}t} = \sqrt{\frac{r_{\rm p}^3}{Gm(1 + e)}}\left[-\sin f\,\mathcal{R} + \frac{2(2 + e + e\cos f)}{1 + e\cos f}\sin^2\frac{f}{2}\,\mathcal{S}\right]. \tag{21}$$

The presence of the terms ($\sin f$) and ($\sin^2 f/2$) in the equation causes the variations of $r_{\rm p}$ to be much smaller than those of p. Therefore, assuming $\mathcal{R} = 0$ is a reasonable simplification for high-eccentricity systems.

Several important aspects warrant further discussion. First, the additional acceleration term $\boldsymbol{f}_{\rm MT}$ given in equation (20) is derived within a classical Galilean framework. Here, the orbital angular momentum $J_{\rm orb}$ is approximated to Newtonian (0PN) as $\boldsymbol{J}_{\rm orb} = \sum m_i \boldsymbol{y}_i \times \boldsymbol{v}_i$. However, near pericentre, where $r_{\rm p} < 10\ {\rm Gm}^{-2}$ and characteristic velocities reach $0.1c$, this approximation may introduce non-negligible errors. Such limitations highlight the necessity for a fully relativistic treatment of MT-induced perturbations, which should be pursued in future work. Secondly, it is notable that some previous studies, particularly those not focused on orbital angular momentum evolution (e.g. Zalamea

Downloaded from https://academic.oup.com/mnras/article/543/4/3503/8287737 by guest on 06 February 2026

et al. 2010), assume that MT does not induce any perturbative acceleration. This corresponds to setting $\mathcal{S} = 0$ in equation (18). Under such assumptions, $J_{\rm orb}$ is not conserved. Assuming mass conservation ($\gamma = 1$) and an extreme mass ratio ($q \ll 1$), equation (18) is $\dot{J}_{\rm orb}/J_{\rm orb} \approx \dot{m}_1/m_1$, implying that the angular momentum associated with the transferred mass is entirely lost from the system. This is the maximum limit of $J_{\rm orb}$ loss when mass conservation.

In Sections 4, 5, and 6, we restrict our analysis to scenarios where total mass and $J_{\rm orb}$ are conserved, corresponding to $\tilde{h} = 1$. Consequently, we do not specify explicit forms for the functions $\tilde{f}(\alpha, q, \gamma)$ and $\tilde{g}(\beta, q, \gamma)$ introduced in the generalized conservation laws. A more detailed discussion on how deviations from these conservation assumptions could affect the long-term orbital evolution will be presented in Section 7.3.

4 SHORT-TERM ORBITAL EVOLUTION USING PN METHOD

In this section, we analyse the orbital dynamics of an EMRI system as described in Section 2. We adopt the PN method rather than the Kerr space–time geodesic approach because it provides a specific form of the perturbation acceleration, as shown in equation (2). The acceleration $\boldsymbol{f}_{\rm MT}$ from MT can be directly added to this perturbation. Such a simulation is simple. In contrast, converting the geodesic equation into an acceleration form and applying the perturbed Kepler method is challenging, as is incorporating the effect of gravitational radiation into geodesics.

Section 4.1 establishes the relationship between the latitude angle ψ, and the orbital elements $(f, \omega, \phi, \Omega, \iota)$. Here, ψ is the angle between the instantaneous orbital plane and the equatorial plane, which is perpendicular to the IMBH's spin axis. Section 4.2 indicates the upper limit of the mass of a WD in this system. Section 4.3 includes the MT process and compares the effects of MT and gravitational radiation on key orbital parameters.

4.1 Angular relationship in relative coordinate

We adopt the relative coordinate system illustrated in Fig. 2, where the Cartesian axes (X,Y,Z) correspond to the spherical coordinates (r, θ, φ), with the transformation $(r^X, r^Y, r^Z) = r\,(\sin\theta\cos\varphi, \sin\theta\sin\varphi, \cos\theta)$. From this definition, the polar angle θ can be written as $\theta = \cos^{-1}(\sin\iota\sin\phi)$. Here, θ is the polar angle, while its complement $\psi = \pi/2 - \theta$ is referred to as the latitude.

We align the spin axis of the IMBH along the z-axis and place the WD at pericentre at the initial time, setting $f_0 = \phi_0 - \omega_0 = 0$. Additionally, we choose $\varphi_0 = \pi/2$. Throughout, a subscript 0 denotes quantities evaluated at the initial time. The orbital angular parameters are then determined as $\Omega_0 = \pi/2 - \varphi_0$, $\iota_0 = \pi/2 - \theta_0$, $\phi_0 = \varphi_0$, $\omega_0 = \phi_0 - f_0$.

The spin orientation of a body is described using angles ϑ and φ in conjunction with the basis vectors $\boldsymbol{n}$, $\boldsymbol{\lambda}$, $\boldsymbol{\ell}$, such that

$$\frac{\boldsymbol{S}_{\rm A}}{|\boldsymbol{S}_{\rm A}|} := \sin\vartheta_{\rm A}\cos\varphi_{\rm A}\boldsymbol{n} + \sin\vartheta_{\rm A}\sin\varphi_{\rm A}\boldsymbol{\lambda} + \cos\vartheta_{\rm A}\boldsymbol{\ell}, \tag{22}$$

where $|\boldsymbol{S}_{\rm A}| := \chi_{\rm A} G m_{\rm A}^2/c$, and $\chi_{\rm A}$ is the dimensionless spin size parameter, generally ranging from 0 to 1. The initial spin $\boldsymbol{S}_{20}$ of the IMBH can be expressed as $|\boldsymbol{S}_{20}|(\cos\theta_0\boldsymbol{n} + \sin\theta_0\boldsymbol{\iota})$. Comparing with equation (22), the initial angles satisfy $\vartheta_{20} = \frac{\pi}{2} - \theta_0 = \iota_0$ and $\varphi_{20} = 0$. In the context of Kerr space–time, the quantity $|\psi_0| = |\pi/2 - \theta_0|$ represents the maximum latitude of the corresponding geodesic motion (Schmidt 2002; Fujita & Hikida 2009).

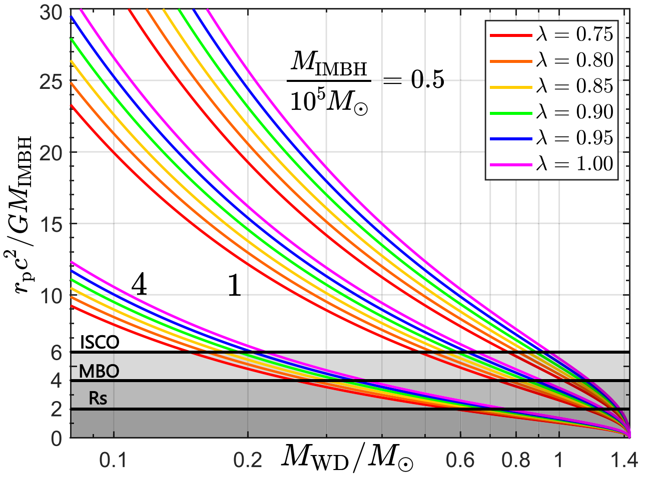

Figure 4. The pericentre distance $r_{\rm p}$ for Roche-lobe overflow given by $r_{\rm p} = \lambda R_{\rm WD}(M_{\rm WD})/f(A, q)$, is shown as a function of $M_{\rm WD}$ for fixed values of $M_{\rm IMBH}/10^5{\rm M}_\odot = 0.5$, 1, 4. Here, $\lambda \le 1$ ensures $R_{\rm L} \le R_{\rm WD}$ at pericentre. The three black lines represent different distances: ISCO is the innermost stable circular orbit of a Schwarzschild BH, $r_{\rm ISCO} = 6GM_{\rm IMBH}/c^2$; MBO is the marginally bound orbit, $r_{\rm MBO} = 4GM_{\rm IMBH}/c^2$; R$_{\rm s}$ is the Schwarzschild radius, ${\rm R}_{\rm s} = 2GM_{\rm IMBH}/c^2$.

In general, the initial angle conditions are

$$\Omega_0 = 0, \quad \psi_0 = \iota_0 = \frac{\pi}{2} - \theta_0, \quad \phi_0 = \frac{\pi}{2}, \quad \omega_0 = \frac{\pi}{2}, \quad f_0 = 0,$$
$$\vartheta_{20} = \frac{\pi}{2} - \theta_0, \quad \varphi_{20} = 0. \tag{23}$$

4.2 Upper mass limit of WD

To carry out the simulations, the mass of the companion star must be specified. For a given IMBH mass $M_{\rm IMBH}$, there exists an upper limit on the WD mass $M_{\rm WD}$ that permits Roche-lobe overflow without resulting in direct infall into the IMBH. This limit arises because the WD radius $R_{\rm WD}(M_{\rm WD})$ decreases with increasing mass, allowing Roche-lobe overflow to occur at a smaller pericentre distance, satisfying $r_{\rm p} \le R_{\rm WD}/f(A, q)$. However, the pericentre distance $r_{\rm p}$ cannot be reduced indefinitely, as excessively small values would cause the WD to plunge directly into the IMBH.

A minimum pericentre distance, $r_{\rm p}^{\rm bound} \le r_{\rm p}$, must be maintained to ensure a bound orbit. The limiting WD mass is determined by the condition $R_{\rm WD} = f(A, q) r_{\rm p}$, evaluated at $r_{\rm p} = r_{\rm p}^{\rm bound}$.

In Fig. 4, we illustrate the relationship between the pericentre distance $r_{\rm p}$ and the WD mass $M_{\rm WD}$ required for Roche-lobe overflow, where $\lambda := f(A, q) r_{\rm p}/R_{\rm WD} \le 1$, for a fixed IMBH mass. Imposing the bound orbit condition $r_{\rm p}^{\rm bound} = r_{\rm ISCO}$, we find that the maximum WD mass compatible with Roche-lobe overflow is constrained to $M_{\rm WD} < 0.2\,{\rm M}_\odot$ when $M_{\rm IMBH} = 4 \times 10^5\,{\rm M}_\odot$. This constraint underscores the necessity of a highly eccentric orbit, finely tuned to match the QPE period, for MT to occur – implying that the donor star should be a low-mass WD.

4.3 Orbital evolution with MT

In this subsection, we analyse the orbits using the PN method with the MT processes. The pericentre distance $r_{\rm p}$ and radial eccentricity $e_{\rm r} := \left(r_{\rm a} - r_{\rm p}\right) / \left(r_{\rm a} + r_{\rm p}\right)$ can be roughly determined. First, MT requires the Roche lobe radius, $R_{\rm Lp} = f(A, q) r_{\rm p} \lesssim R_{\rm WD}(M_{\rm WD})$, as outlined in Section 4.2, with $M_{\rm WD} < M_{\rm WD}^{\rm limit}(M_{\rm IMBH}, r_{\rm p}^{\rm bound}) \ll M_{\rm ch}$,

Downloaded from https://academic.oup.com/mnras/article/543/4/3503/8287737 by guest on 06 February 2026

which directly constrains the range of r_p. Secondly, due to the Hills mechanism, and to match the periods observed in QPE light curves (Miniutti et al. 2019; Miniutti, G. et al. 2023a), the radial eccentricity $e_r > 0.95$ (Chen et al. 2022; Wang et al. 2022; Wang, Di 2024).

We assume that the spin of the low-mass WD can be ignored, setting $\chi_1 = 0$. We also set the mass $m_1 = M_{\rm WD} = 0.15\,{\rm M}_\odot$, $m_2 = M_{\rm IMBH} = 4 \times 10^5\,{\rm M}_\odot$, and $q = m_1/m_2 = 3.75 \times 10^{-7}$.

The initial pericentre distance r_{p0} is set based on the relationship between $R_{\rm Lp}$ and $R_{\rm WD}$, i.e. $R_{\rm Lp} = f(A, q) r_p := (1-\epsilon) R_{\rm WD} < R_{\rm WD}$. Here, to quantify the degree of overflow, we define a dimensionless overflow parameter, $\epsilon(r_p, M_{\rm WD}, q) = 1 - r_p C_L(q)/R_{\rm WD}(M_{\rm WD})$, where $C_L = f(A = 0, q)$ characterizes the Roche geometry. We set the initial overflow parameter to $\epsilon_0 = 5 \times 10^{-3}$, yielding $r_{p0} \simeq 3.1502 \times 10^6\ {\rm GM}_\odot\, c^{-2} \simeq 7.875\ {\rm Gm}_2\, c^{-2} \simeq 253.87 R_{\rm WD}(M_{\rm WD})$. The value of r_{p0} is fixed in all subsequent calculations. For the initial radial eccentricity, we adopt $e_{r0} = 0.99$, consistent with the orbit of the QPE, when assume zero MBH spin ($\chi_2 = 0$). Because lower χ_2 and higher initial latitude ψ_0 lead to higher initial e_r.

For initial angular configurations, we use the angular relationships described in Section 4.1. We only need to adjust initial latitude ψ_0 and IMBH spin parameter χ_2. We set $\psi_0 = 0^\circ, 28^\circ, 56^\circ$, and 84°, and $\chi_2 = 0$, 0.3, 0.6, and 0.9. The only remaining parameter introduced is ξ_0, which regulates the WD surface density $\rho_{\rm ph}$ in equation (10). According to the result of equation (11), we set $\xi_0 = 3.98 \times 10^{-3}$. To summarize, all the initial parameters that need to be determined independently include $\{e_{r0}, M_{\rm WD}, M_{\rm IMBH}, \epsilon_0, \psi_0, \chi_2, \xi_0\}$.

To illustrate the impact of MT on orbital dynamics, we examine the evolution of the radial eccentricity e_r, under scenarios with and without MT. As shown in Fig. 5, GW emission alone leads to a gradual decrease in e_r, with a rate of change $\delta e_r^{\rm GW} \approx -10^{-7}$ per cycle. In contrast, when MT is included, the eccentricity increases, with $\delta e_r^{\rm GW+MT} \approx 10^{-5}$ per cycle.

This pronounced eccentricity growth driven by MT highlights its dominant influence on the orbital evolution under the current parameter regime. The perturbative acceleration associated with MT, as described by equation (4b), exerts a significantly stronger effect on the orbital parameters than the eccentricity damping caused by GW radiation. These results underscore the necessity of incorporating MT effects in models aiming to accurately capture the dynamical behaviour of such systems.

In addition, there are some relativistic effects brought by IMBH spin. In Fig. 5, the lower χ_2 and higher initial ψ_0 lead to higher initial e_r. This relationship arises because, at a fixed pericentre distance, the IMBH's spin can transfer orbital energy to the companion star. For prograde orbits – those aligned with the IMBH's spin – the enhanced frame-dragging effect leads to increased orbital velocities, reduced semimajor axes, and consequently, lower orbital periods and eccentricities. Conversely, orbits with higher inclinations, deviating from the equatorial plane, reduce this spin-induced effect, resulting in eccentricities that more closely resemble scenarios without spin. This behaviour aligns with PN predictions, where spin-orbit coupling induces variations in orbital elements, contingent on the spin magnitude and orbital orientation.

The change of eccentricity in Fig. 5 is not monotonous, but has obvious fluctuations. The higher χ_2 and initial ψ_0 enhance the jitter phenomenon. This fluctuation is more pronounced in the first few weeks of the orbit, but as the simulation time increases, the effects of MT and gravitational radiation allow us to identify long-term evolutionary features from the fluctuations. However, the distinctive periodic oscillation effect does not occur in the geodesic of Kerr space–times, nor is it present in non-spinning binary systems using the PN method. We speculate that this effect arises from the spin terms $\boldsymbol{a}_{\rm SO}$, $\boldsymbol{a}_{\rm SS}$, $\boldsymbol{a}_{\rm SOPN}$ in the PN orbital dynamics described in equation (2), derived from Tagoshi et al. (2001) using the harmonic gauge condition. Furthermore, we find that the changes in e_r does not decrease in higher PN order relative acceleration terms (below 4 PN), when using equations from different PN orders to reproduce the same r_p and T. This suggests that higher PN order terms involving the spin parameter χ_2 should be considered, or it may indicate a subtle connection between harmonic coordinates and Boyer–Lindquist coordinates.

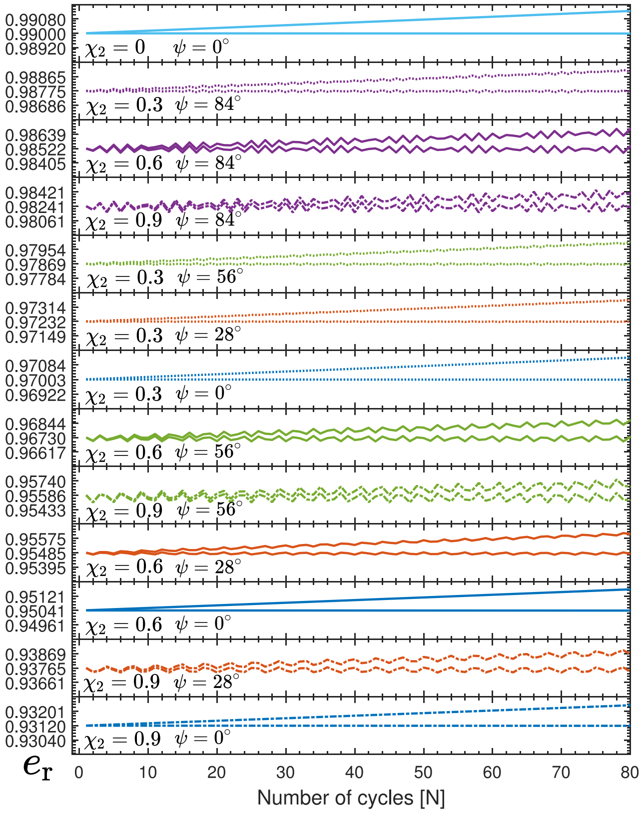

Figure 5. The evolution of the radial eccentricity e_r with and without MT. In each panel, the higher curve represents the evolution of $e_r^{\rm MT}$ with MT, and the lower one represents the evolution of e_r^* without MT. The different line colours correspond to the same initial latitude ψ_0, and different line styles denote the same IMBH spin parameters χ_2.

Fig. 6 shows that the orbital period becomes longer when MT is introduced, and the increase is larger for higher ψ_0 and lower χ_2. This result can be inferred from the increase of e_r. We give the average values and the maximum jitter difference of e_r and T in Table 1. The lower χ_2 and higher initial ψ_0 lead to higher $\bar{e}_r$ and $\overline{T}$. However, the higher χ_2 and initial ψ_0 enhance the jitter difference of the Δe_r and ΔT.

We note that the relationship between $\bar{e}_r$ and $\overline{T}$ and the relationship between Δe_r and ΔT can be explained by Kepler's law even though the EOMs include PN corrections. Using Kepler's period expression $T \propto a^{3/2}$, where semimajor axis $a = (r_a + r_p)/2$, and applying a first-order expansion for $\Delta T \ll \overline{T}$, we can get

$$\frac{\overline{T}_1}{\overline{T}_2} = \left(\frac{\bar{r}_{p1}}{\bar{r}_{p2}} \frac{1-\bar{e}_{r2}}{1-\bar{e}_{r1}}\right)^{3/2} = \left(\frac{\bar{r}_{a1}}{\bar{r}_{a2}} \frac{1+\bar{e}_{r2}}{1+\bar{e}_{r1}}\right)^{3/2} \simeq \left(\frac{1-\bar{e}_{r2}}{1-\bar{e}_{r1}}\right)^{3/2},$$

$$\frac{\Delta T}{\overline{T}} \simeq \frac{3}{2} \frac{\Delta r_a + \Delta r_p}{\bar{r}_a + \bar{r}_p} \simeq \frac{3}{2} \frac{\Delta e_r}{1-\bar{e}_r}. \tag{24}$$

Downloaded from https://academic.oup.com/mnras/article/543/4/3503/8287737 by guest on 06 February 2026

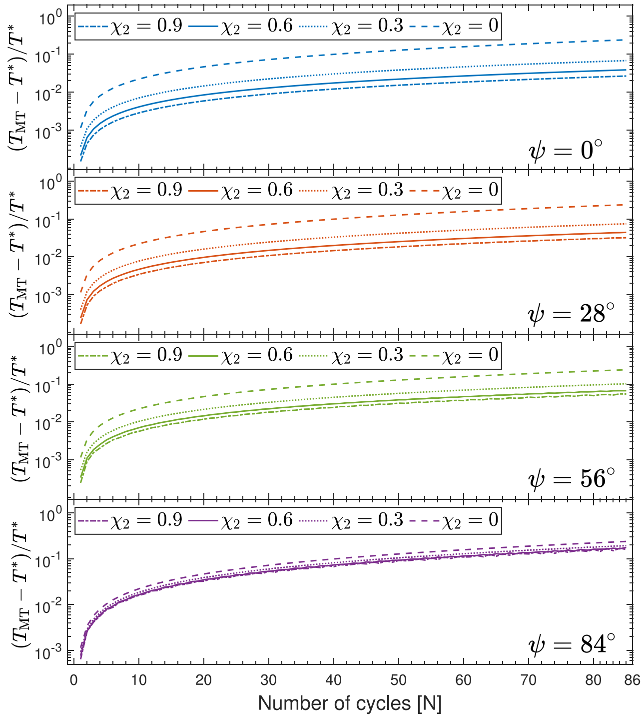

Figure 6. The evolution of $(T_{\rm MT} - T^*)/T^*$ due to the MT process, where $T^*(\rm N)$ denotes the period without MT process. In contrast, $T_{\rm MT}(\rm N)$ represents the period with MT ($\xi_0 = 3.98 \times 10^{-3}$). We give the influence of different χ_2 under identical initial ψ_0.

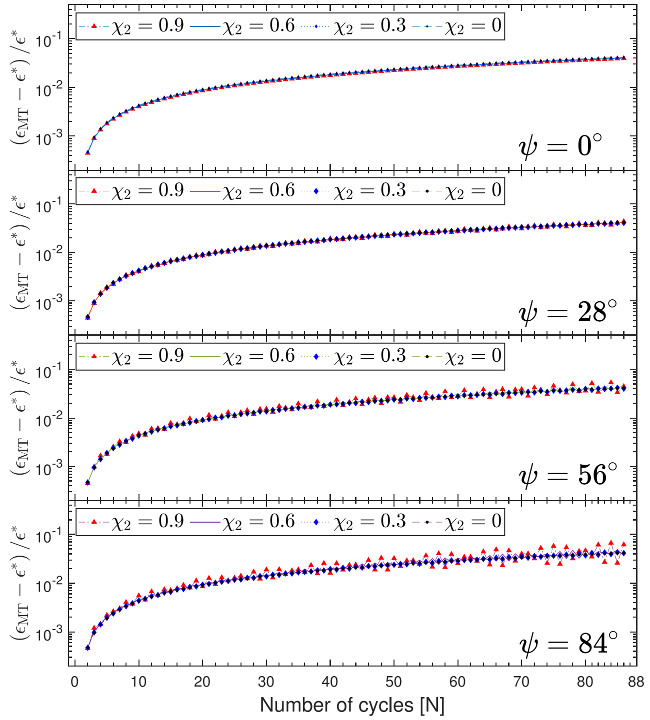

Figure 7. The evolution of $(\epsilon_{\rm MT} - \epsilon^*)/\epsilon^*$ due to the MT process, where $\epsilon_{\rm MT}$ denotes ϵ with MT ($\xi_0 = 3.98 \times 10^{-3}$), and ϵ^* denotes ϵ without MT. For the same initial ψ_0, the results for different χ_2 are shown in a single subfigure. In the top panel, where $\psi_0 = 0°$, the four lines do not overlap; the lower the χ_2, the greater the value.

Table 1. The Average Radial Eccentricity $\bar{e}_{\rm r}$ And The Difference $e_{\rm rmax} - \bar{e}_{\rm r}$, And The Average Period $\overline{T}$ And The Ratio Of The Difference $(T_{\rm max} - \overline{T})/\overline{T}$.

	$\chi_2 = 0$	$\chi_2 = 0.3$	$\chi_2 = 0.6$	$\chi_2 = 0.9$
$\bar{e}_{\rm r} - 0.99$				
$\psi_0 = 0°$	0	−0.0200	−0.0396	−0.0588
$\psi_0 = 28°$	0	−0.0177	−0.0352	−0.0525
$\psi_0 = 56°$	0	−0.0113	−0.0228	−0.0344
$\psi_0 = 84°$	0	−0.0023	−0.0048	−0.0077
$e_{\rm rmax} - \bar{e}_{\rm r}$				
$\psi_0 = 0°$	5.358e-6	5.019e-6	4.984e-6	4.954e-6
$\psi_0 = 28°$	5.358e-6	2.146e-5	7.786e-5	1.959e-4
$\psi_0 = 56°$	5.358e-6	5.164e-5	2.168e-4	5.223e-4
$\psi_0 = 84°$	5.358e-6	7.477e-5	2.904e-4	6.508e-4
$\overline{T}/\rm hr$				
$\psi_0 = 0°$	76.460	14.911	7.0774	4.3667
$\psi_0 = 28°$	76.460	16.772	8.1180	5.0305
$\psi_0 = 56°$	76.460	24.730	13.055	8.3270
$\psi_0 = 84°$	76.460	56.415	42.455	32.573
$(T_{\rm max} - \overline{T})/\overline{T}$				
$\psi_0 = 0°$	7.992e-4	2.511e-4	1.501e-4	1.080e-4
$\psi_0 = 28°$	7.992e-4	1.158e-3	2.602e-3	4.850e-3
$\psi_0 = 56°$	7.992e-4	3.588e-3	9.925e-3	1.789e-2
$\psi_0 = 84°$	7.992e-4	9.162e-3	2.961e-2	5.620e-2

The above two equations provide good fit to the results presented in Table 1. These relationships can also help us calculate the effects of MT and gravitational radiation.

As described in equation (24). We get $\delta\overline{T}_{\rm GW+MT}/\overline{T} \approx 10^{-3}$ and $\delta\overline{T}_{\rm GW}/\overline{T} \approx 10^{-5}$. By comparing with $(T_{\rm max} - \overline{T})/\overline{T}$ in Table 1, we find that within 10 to 10^2 cycles, the change of period by the MT process completely masks the PN jitter effect, so no obvious jitter effect is found in Fig. 6.

Finally, since the MT rate depends sensitively on the ratio of the WD's radius to the Roche lobe radius near pericentre, we use the dimensionless overflow parameter

$$\epsilon := \frac{R_{\rm WD} - R_{\rm Lp}}{R_{\rm WD}} = 1 - \frac{r_{\rm p}\, C_{\rm L}(q)}{R_{\rm WD}\,(M_{\rm WD})}, \tag{25}$$

to assess how PN orbital effects influence MT and its rate. In Fig. 7, different values of χ_2 and ψ_0 have almost no effect on $(\epsilon_{\rm MT} - \epsilon^*)/\epsilon^*$; the periodic oscillations caused by the PN method are tightly concentrated around a single curve on the logarithmic plot. This indicates that spin is not strongly related to the growth of $\epsilon_{\rm MT}$ under MT.

For the change of pericentre distance $r_{\rm p}$, we do not need to draw its figure separately, because it is closely related to parameter ϵ. The relationship between $\Delta\epsilon$ and $\Delta r_{\rm p}$ can be expressed using a first-order Taylor expansion ($\Delta\epsilon \ll \epsilon$, $\Delta r_{\rm p} \ll r_{\rm p}$):

$$\frac{\Delta\epsilon}{1-\epsilon} \simeq -\frac{\Delta r_{\rm p}}{r_{\rm p}} - \frac{\Delta\left(C_{\rm L}/R_{\rm WD}\right)}{C_{\rm L}/R_{\rm WD}}, \tag{26}$$

where $\Delta\left(C_{\rm L}/R_{\rm WD}\right)$ reflects the change of $M_{\rm WD}$ and $M_{\rm IMBH}$. First, if without the MT process, the mass of WD and the mass ratio q will not change, i.e. $\Delta\left(C_{\rm L}/R_{\rm WD}\right)$ is zero. Therefore, ϵ only changes with $r_{\rm p}$. Because $\epsilon \ll 1$, the relative change $\Delta\epsilon/\epsilon$ is

$$\frac{\Delta\epsilon}{\epsilon} \simeq -\frac{\Delta r_{\rm p}}{r_{\rm p}\epsilon} \gg -\frac{\Delta r_{\rm p}}{r_{\rm p}}. \tag{27}$$

When χ_2 and ψ_0 are large, a jitter $\Delta r_{\rm p}/r_{\rm p} \sim 10^{-4}$ can alter $\epsilon \sim 10^{-3}$ by over 10 per cent, significantly impacting the MT rate upon

Downloaded from https://academic.oup.com/mnras/article/543/4/3503/8287737 by guest on 06 February 2026

reconsideration of the MT process. This reflects that even a very small change in r_p can have a big impact on MT rate.

Secondly, the MT process causes $\Delta\,(C_\mathrm{L}/R_\mathrm{WD})$ to gradually increase the relative deviation of the overflow parameter ϵ_MT from its value without MT, ϵ^*, as shown in Fig. 7. To understand the importance of $\Delta\,(C_\mathrm{L}/R_\mathrm{WD})$, we give the first-order expansion by $\Delta M_\mathrm{WD}/M_\mathrm{WD}$, using equations (8) and (16):

$$-\frac{\Delta\,(C_\mathrm{L}/R_\mathrm{WD})}{C_\mathrm{L}/R_\mathrm{WD}} \simeq -\frac{2+q\gamma}{3}\frac{\Delta M_\mathrm{WD}}{M_\mathrm{WD}} > 0. \tag{28}$$

Here, Δ represents the difference between the MT process and the process without MT. From the results of numerical calculation, we find $|\Delta M_\mathrm{WD}/M_\mathrm{WD}| \gg \left|\Delta r_\mathrm{p}/r_\mathrm{p}\right|$. Therefore, by equation (26),

$$\frac{\epsilon_\mathrm{MT}-\epsilon^*}{\epsilon^*} \simeq -\frac{\Delta\,(C_\mathrm{L}/R_\mathrm{WD})}{C_\mathrm{L}/R_\mathrm{WD}}\frac{1}{\epsilon^*} \simeq \frac{2+q\gamma}{3}\left|\frac{\Delta M_\mathrm{WD}/M_\mathrm{WD}}{\epsilon^*}\right| > 0. \tag{29}$$

This equation accurately reproduces the trend in Fig. 7. Since the MT rate remains largely insensitive to the IMBH's spin, the PN-induced periodic oscillations converge tightly around a single curve in the logarithmic plot.

Through numerical simulations, we quantify the per-orbit variations in both pericentre distance r_p and overflow parameter ϵ. For each orbit number N, we define these variations as $\delta r_\mathrm{p} = r_\mathrm{p}(\mathrm{N}) - r_\mathrm{p}(\mathrm{N}-1)$ for the pericentre distance, $\delta\epsilon = \epsilon(\mathrm{N}) - \epsilon(\mathrm{N}-1)$ for the outflow parameter. After averaging over multiple orbital cycles, we find distinct evolutionary trends depending on the physical processes included: First, GW emission alone, the per-orbit variations are $\delta\bar{r}_\mathrm{p}^\mathrm{GW}/\bar{r}_\mathrm{p} \approx -3.3\times10^{-8}$ and $\delta\bar{\epsilon}^\mathrm{GW}/\bar{\epsilon} \approx 5.5\times10^{-6}$. Secondly, combined GW emission and MT process, the per-orbit variations are $\delta\bar{r}_\mathrm{p}^\mathrm{GW+MT}/\bar{r}_\mathrm{p} \approx -1.7\times10^{-8}$ and $\delta\bar{\epsilon}^\mathrm{GW+MT}/\bar{\epsilon} \approx 4.6\times10^{-4}$.

We draw several key conclusions from our analysis. First, the orbital decay driven by GW emission is slowed by the MT process. This is evident from the fact that the pericentre shift, $\delta\bar{r}_\mathrm{p}^\mathrm{GW+MT}$, is less negative than the pure GW-driven shift, $\delta\bar{r}_\mathrm{p}^\mathrm{GW}$. Secondly, the outflow evolution is strongly enhanced when MT is active. The change in outflow parameter, $\delta\bar{\epsilon}^\mathrm{GW+MT}$, far exceeds that from GWs alone, $\delta\bar{\epsilon}^\mathrm{GW}$. This means the mass stripping process rapidly widens the gap between the WD's radius and its Roche lobe. The underlying physics can be understood through two competing effects: First, as the WD loses mass, its radius R_WD increases following the mass–radius relation (equation 8). Secondly, the Roche radius R_L scales with mass ratio as $q^{1/3}$ (equation 16). Since MT reduces q, the Roche radius R_L shrinks slightly. The final result is that R_WD expands much faster than R_L contracts, creating a positive feedback loop that dramatically boosts the MT rate. This explains why the relative mass-loss rate $|\delta M_\mathrm{WD}/M_\mathrm{WD}|$ dominates over the pericentre variation $\left|\delta r_\mathrm{p}/r_\mathrm{p}\right|$ – a hallmark of WD donors that distinguishes them from COs whose radius shrink upon mass-loss. Therefore, for WDs, the orbital dynamics of MT cannot be ignored.

5 LONG-TERM EVOLUTION WITH MT

Applying the PN method for calculations is computationally expensive, especially for long-duration simulations. Consequently, we employ a Keplerian orbital approximation and time-average approach to efficiently evaluate the long-term evolution.

First, we analyse the combined effects of the MT process and gravitational radiation on the long-term orbital evolution, as described in Section 5.1.1. To calculate the transferred mass δM_WD from the WD over one orbital period, we use the MT rate $\dot{m}_1$, as detailed in Section 5.1.2 and Appendices B and C. Secondly, we orbital-average the parameters and analyse the long-term MT effects on a Keplerian elliptical orbit in Section 5.2. Thirdly, we verify the accuracy of our long-term calculations through short-term numerical calculations in Section 5.3.

5.1 Relevance of the MT effects

5.1.1 The relative importance of MT and gravitational radiation

In this section, we use the second method in Section 3.3 to calculate the orbital evolution with MT. According to equation (20), the MT acceleration $\boldsymbol{f}_\mathrm{MT}^\mathcal{B}$ is

$$\boldsymbol{f}_\mathrm{MT}^\mathcal{B} = \left(-\tfrac{\dot{m}_1}{m_1}\right) r\,\dot{f}_\mathrm{N}(1-q)\tilde{h}\boldsymbol{\lambda}. \tag{30}$$

We can give the instantaneous change $\dot{a}$ using $\dot{p}$ and $\dot{e}$ in equation (4). In this case, using the periodic integral of equation (30), we provide the secular change rate of the orbital semimajor axis $\left\langle\dot{a}_\mathrm{MT}^\mathcal{B}\right\rangle_\mathrm{sec}$, which can be expressed as

$$\left\langle\dot{a}_\mathrm{MT}^\mathcal{B}\right\rangle_\mathrm{sec} = \left(-\frac{\delta M_\mathrm{WD}}{M_\mathrm{WD}}\right)\sqrt{\frac{GM_\mathrm{WD}}{c^2a_\mathrm{r}}\frac{c}{\pi}\frac{1+e_\mathrm{r}}{1-e_\mathrm{r}}}(1-q)\sqrt{\frac{1+q}{q}}\tilde{h}, \tag{31}$$

where δM_WD represents the transferred mass of the WD during each orbital period. Here, $\langle\cdots\rangle_\mathrm{sec}$ is the periodic average operator.

In Section 3.3, we have assumed an MT rate $\dot{m}_1$ without providing a formula to calculate it. Based on the assumptions made by Sepinsky et al. (2007b), we propose that the MT rate $\dot{m}_1$ at high eccentricity $e_\mathrm{r} \lesssim 1$, can be expressed as $\dot{M}_\mathrm{WD} := \dot{M}_0\delta(f)$, where $\dot{M}_0$ is a quantity related to the orbit to be determined. Therefore, the mass stripped from WD in one cycle is

$$\delta M_\mathrm{WD} = \int_{-\pi}^{\pi}\dot{M}_0\,\delta(f)\dot{f}_\mathrm{N}^{-1}\mathrm{d}f \simeq \dot{M}_0\sqrt{\frac{a_\mathrm{r}^3}{Gm}}\frac{(1-e_\mathrm{r})^{3/2}}{(1+e_\mathrm{r})^{1/2}}. \tag{32}$$

Conversely, quantity $\dot{M}_0$ can be expressed in terms of δM_WD:

$$\dot{M}_0 \simeq \frac{\delta M_\mathrm{WD}}{T}2\pi\frac{(1+e_\mathrm{r})^{1/2}}{(1-e_\mathrm{r})^{3/2}}. \tag{33}$$

In addition, the average change in the semimajor axis due to quadrupole gravitational radiation $\langle\dot{a}_\mathrm{GW}\rangle_\mathrm{sec}$ is given by Peters (1964):

$$\langle\dot{a}_\mathrm{GW}\rangle_\mathrm{sec} = -\left(\frac{GM_\mathrm{WD}}{c^2a_\mathrm{r}}\right)^3\frac{64}{5}c\frac{1+q}{q^2}\frac{1+\frac{73}{24}e_\mathrm{r}^2+\frac{37}{96}e_\mathrm{r}^4}{(1-e_\mathrm{r}^2)^{7/2}}. \tag{34}$$

Because $\delta M_\mathrm{WD} < 0$, MT causes the orbit to expand outwards; we have $\langle\dot{a}_\mathrm{GW}\rangle_\mathrm{sec} < 0 < \left\langle\dot{a}_\mathrm{MT}^\mathcal{B}\right\rangle_\mathrm{sec}$. To identify which is the dominant process that determines the evolution of a, we calculate the change ratio $\left|\dot{a}_\mathrm{MT}^\mathcal{B}/\dot{a}_\mathrm{GW}\right|_\mathrm{sec}$, which is given by

$$\begin{aligned}\left|\frac{\dot{a}_\mathrm{MT}^\mathcal{B}}{\dot{a}_\mathrm{GW}}\right|_\mathrm{sec} &= \left(-\frac{\delta M_\mathrm{WD}}{M_\mathrm{WD}}\right)\sigma^{-1},\\ \sigma &= \tilde{\lambda}^{-5/2}q\frac{64}{5}\pi\frac{1+\frac{73}{24}e_\mathrm{r}^2+\frac{37}{96}e_\mathrm{r}^4}{(1+e_\mathrm{r})^{9/2}}\frac{\sqrt{1+q}}{(1-q)\tilde{h}},\end{aligned} \tag{35}$$

where $\tilde{\lambda} := r_\mathrm{p}/(Gm_2/c^2) \approx 7.875$, $q = 3.75\times10^{-7}$, $e_\mathrm{r} = 0.99$, and $\tilde{h} = 1$ under the orbital conditions specified in Section 4. Following this condition, we find $\sigma = 1.7\times10^{-8}$.

For gravitational radiation to dominate, the system should satisfy $\left|\dot{a}_\mathrm{MT}^\mathcal{B}/\dot{a}_\mathrm{GW}\right|_\mathrm{sec} < 1$, which implies $|\delta M_\mathrm{WD}| < 1.7\times10^{-8}M_\mathrm{WD}$ per period. Under the above orbital conditions with $M_\mathrm{WD} = 0.15\,\mathrm{M}_\odot$ and $T \sim 76\,\mathrm{h}$, this leads to $\left|\dot{M}_\mathrm{WD}\right|_\mathrm{sec} < 2.94\times10^{-7}\mathrm{M}_\odot\,\mathrm{yr}^{-1}$. This represents an exceptionally low MT rate. For $\left\langle\dot{a}_\mathrm{MT}^\mathcal{B}\right\rangle_\mathrm{sec} = -\langle\dot{a}_\mathrm{GW}\rangle_\mathrm{sec}$, we can get $|\delta M_\mathrm{WD}| \propto -\langle\dot{a}_\mathrm{GW}\rangle_\mathrm{sec}(1-e_\mathrm{r})$ using equation (31). The factor $(1-e_\mathrm{r})$ is a small amount arises from the integral of the MT

Downloaded from https://academic.oup.com/mnras/article/543/4/3503/8287737 by guest on 06 February 2026

rate in equation (32). Therefore, the low transferred mass $|\delta M_{\rm WD}|$ is due to the high eccentricity.

Our above conclusion differs from that of Wang et al. (2022). Their $\dot{M}_{\rm WD}$ corresponds to our $\dot{M}_0$ in equation (33); however, $\dot{M}_0 < 0$ does not represent an instantaneous MT rate. They neglected the factor $(1 - e_{\rm r})^{-3/2} \gg 1$ for $\dot{M}_0$. As a result, they suggest that $|\delta M_{\rm WD}| > 10^{-3} M_{\rm WD}$ is required for the MT process to dominate, i.e. $\left|\dot{a}^{\mathcal{B}}_{\rm MT}/\dot{a}_{\rm GW}\right|_{\rm sec} > 1$, based on their parameters.

5.1.2 *Simplification of MT model*

To investigate the orbital evolution induced by $\boldsymbol{f}^{\mathcal{B}}_{\rm MT}$, it is essential to estimate the $\delta M_{\rm WD}$. While direct numerical integration of the MT rate (equations 12 and 13) is possible, this approach obscures the underlying dependence of $\delta M_{\rm WD}$ on key system parameters: the pericentre distance $r_{\rm p}$, orbital eccentricity e, and the masses of the WD ($M_{\rm WD}$), and IMBH ($M_{\rm IMBH}$). We therefore develop a simplified analytic treatment.

The MT process depends critically on the relative size of the WD compared to its Roche lobe. We characterize this through the dimensionless parameter $\varepsilon = (R_{\rm WD} - R_{\rm L})/R_{\rm WD}$. Note that ε varies throughout the eccentric orbit as the binary separation changes. This is distinct from the parameter ϵ introduced earlier, where $\epsilon = \varepsilon(D = r_{\rm p}) \ll 1$.

For our $\delta M_{\rm WD}$ calculation, we focus exclusively on the adiabatic MT component (equation 13), neglecting the isothermal contribution (equation 12). This simplification is justified because isothermal transfer only becomes significant far from pericentre. Our delta-function approximation for the MT rate makes dynamical effects negligible away from pericentre.

To enable integration over the orbital phase and determine the total mass stripped per orbital period, we first develop a simplified expression for the instantaneous MT rate $\dot{m}_1$. This takes the form

$$\dot{m}_1 \simeq -H(\varepsilon)\cdot 2\pi \cdot W(K,\Gamma)\cdot (G M_{\rm IMBH})^2 \,\frac{C_{\rm L}^3}{\sqrt{\mathcal{R}_0}} \times \left(\sum_{m=0}^{\infty} \mathcal{S}_m \varepsilon^m\right)\left(\sum_{n=0}^{\infty} \mathcal{U}_{\varepsilon n}\varepsilon^n\right), \qquad (36)$$

where $W(K,\Gamma) = F(K,\Gamma)\cdot\left[K^{-\frac{1}{\Gamma}}(\Gamma-1)/\Gamma\right]^{\frac{3\Gamma-1}{2(\Gamma-1)}}$. Detailed definitions of the coefficients $\mathcal{R}_0$, $\mathcal{S}_m$, and $\mathcal{U}_{\varepsilon n}$ are provided in Appendix B.

For a Keplerian elliptical orbit, the integral of $\dot{m}_1$ over a full period can be rearranged as

$$\delta M_{\rm WD} \simeq \int_{-\pi}^{\pi} \dot{m}_1 \dot{f}_{\rm N}^{-1}\,{\rm d}f = C_{\dot{m}_1}\sqrt{\frac{p^3}{Gm}}\sum_{n=0}^{\infty} C_{\varepsilon{\rm n}}\int_{-f_0}^{f_0}\frac{\varepsilon(f)^n\,{\rm d}f}{(1+e\cos f)^2}, \qquad (37)$$

where coefficients $C_{\dot{m}_1}$ and $C_{\varepsilon{\rm n}}$ are derived in Appendix C. The critical phase f_0 satisfying $R_{\rm L}(f_0) = R_{\rm WD}$, i.e. $\varepsilon(f_0) = 0$. The function $f_0(e, \epsilon)$ in equation (C9) is due to $\varepsilon(f_0) = 0$ and the variable $\epsilon = \varepsilon(f = 0)$. The definite integral can be expressed in terms of the Appell hypergeometric function, $\mathrm{AF1}(\alpha;\beta,\beta';\gamma;x,y)$ (Olver et al. 2010). After the integral processing, the function $\delta M_{\rm WD}(\epsilon, e, M_{\rm WD}, q)$ is

$$\delta M_{\rm WD} \simeq \frac{4\,C_{\dot{m}_1} r_{\rm p}^{3/2}}{\sqrt{Gm}}\sqrt{\frac{\epsilon}{2e}}\sum_{n=0}^{\infty}\sum_{m=0}^{\infty} C_{\varepsilon{\rm n}}\binom{n}{m}(-1)^m(1-\epsilon)^m \times \mathrm{AF1}\left[\frac{1}{2};\frac{1}{2},m+2;\frac{3}{2};\frac{1+e}{2e}\epsilon,\epsilon\right]. \qquad (38)$$

The stripping mass is directly related to the outflow parameter ϵ. This simplified yet physically complete model enables efficient computation while maintaining the essential physics of the MT process.

5.2 Long-term orbital effects in Newtonian elliptical orbits

To evaluate the long-term orbital evolution, we also require the secular change rate of orbital eccentricity. For MT, $\langle \dot{e}^{\mathcal{B}}_{\rm MT}\rangle_{\rm sec}$ is obtained using equations (4b) and (30). For gravitational radiation, $\langle \dot{e}_{\rm GW}\rangle_{\rm sec}$ is taken from Peters (1964). They are

$$\begin{aligned}\langle \dot{e}^{\mathcal{B}}_{\rm MT}\rangle_{\rm sec} &= \left(-\frac{\delta M_{\rm WD}}{M_{\rm WD}}\right)\sqrt{\frac{GM_{\rm WD}}{c^2 a_{\rm r}}}\frac{c(1+e_{\rm r})}{\pi a_{\rm r}}(1-q)\sqrt{\frac{1+q}{q}}\tilde{h},\\ \langle \dot{e}_{\rm GW}\rangle_{\rm sec} &= -\left(\frac{GM_{\rm WD}}{c^2 a_{\rm r}}\right)^3\frac{304}{15}\frac{c}{a_{\rm r}}\frac{1+q}{q^2}\frac{e_{\rm r}\left(1+\frac{121}{304}e_{\rm r}^2\right)}{(1-e_{\rm r}^2)^{5/2}}.\end{aligned} \qquad (39)$$

For the pericentre distance, using $\langle \dot{r}_{\rm p}\rangle_{\rm sec} \simeq (1-e)\langle \dot{a}\rangle_{\rm sec} - a\langle \dot{e}\rangle_{\rm sec}$

$$\begin{aligned}\left\langle \dot{r}^{\mathcal{B}}_{\rm pMT}\right\rangle_{\rm sec} &= 0, \qquad (40)\\ \left\langle \dot{r}_{\rm pGW}\right\rangle_{\rm sec} &= -\left(\frac{GM_{\rm WD}}{c^2 a_{\rm r}}\right)^3\frac{64}{5}c\frac{1+q}{q^2}\frac{\left(1-\frac{7}{12}e_{\rm r}+\frac{7}{8}e_{\rm r}^2+\frac{47}{192}e_{\rm r}^3\right)}{(1-e_{\rm r})^{3/2}(1+e_{\rm r})^{7/2}}.\end{aligned}$$

The zero pericentre shift from MT arises because our delta-function model concentrates all mass-loss at pericentre.

Assuming $\gamma = 1$, the orbital period is approximately $\langle \dot{T}\rangle_{\rm sec} \simeq 3\pi\sqrt{a/Gm}\,\langle \dot{a}\rangle_{\rm sec} = 3T\,\langle \dot{a}\rangle_{\rm sec}/2a$. Hence, we have

$$\begin{aligned}\langle \dot{T}^{\mathcal{B}}_{\rm MT}\rangle_{\rm sec} &= \left(-\frac{\delta M_{\rm WD}}{M_{\rm WD}}\right)3\frac{1+e_{\rm r}}{1-e_{\rm r}}(1-q), \qquad (41)\\ \langle \dot{T}_{\rm GW}\rangle_{\rm sec} &= -\left(\frac{GM_{\rm WD}}{c^2 a_{\rm r}}\right)^{5/2}\frac{64}{5}3\pi\sqrt{\frac{1+q}{q^3}}\frac{1+\frac{73}{24}e_{\rm r}^2+\frac{37}{96}e_{\rm r}^4}{(1-e_{\rm r}^2)^{7/2}}.\end{aligned}$$

Now, we can make qualitative predictions about the long-term evolution:

(i) If the pericentre distance $r_{\rm p} \geq R_{\rm WD}/C_{\rm L}$ (i.e. $\epsilon \leq 0$), the Roche lobe is underfilled, and the MT rate is negligible. In this case, we can assume that orbital decay is driven only by gravitational radiation, i.e. $\delta M_{\rm WD} = 0$ and $\dot{a}^{\mathcal{B}}{}_{\rm MT} = 0$. Consequently, a, e, T, and $r_{\rm p}$ all decrease.

(ii) When $r_{\rm p} < R_{\rm WD}/C_{\rm L}$ (i.e. $\epsilon > 0$), and $0 < \left|\dot{a}^{\mathcal{B}}{}_{\rm MT}/\dot{a}_{\rm GW}\right|_{\rm sec} < 1$, gravitational radiation still dominates. The Roche lobe overflow. In this case, a, e, T, and $r_{\rm p}$ continue to decrease. However, ϵ gradually increases due to the radius–mass relationship of the WD (see Section 4.3 for details). Thus, according to equation (38), $|\delta M_{\rm WD}|$ and $\left|\dot{a}^{\mathcal{B}}{}_{\rm MT}/\dot{a}_{\rm GW}\right|_{\rm sec}$ gradually increase.

(iii) As $\left|\dot{a}^{\mathcal{B}}{}_{\rm MT}/\dot{a}_{\rm GW}\right|_{\rm sec} \to 1$, both a and T reach their minimum values simultaneously. Similarly, as $\left|\dot{e}^{\mathcal{B}}{}_{\rm MT}/\dot{e}_{\rm GW}\right|_{\rm sec} \to 1$, the eccentricity e reaches its minimum value. The times at which a and T reach their minima differ slightly from the time when e does, as the change rates due to gravitational radiation follow different formulae.

(iv) Beyond the threshold $\left|\dot{a}^{\mathcal{B}}{}_{\rm MT}/\dot{a}_{\rm GW}\right|_{\rm sec} = 1$, the parameters a, T, and e will increase according to the equations in Sections 5.1.1 and 5.2. At this point, MT begins to dominate. However, $\delta M_{\rm WD}$ continues to rise as described by equation (38), and $r_{\rm p}$ continues to decrease as given by equation (40).

In the absence of other mechanisms, the MT process remains dominant without reverting to gravitational radiation dominance. Since $\langle \dot{r}_{\rm p}\rangle_{\rm sec} = \left\langle \dot{r}^{\mathcal{B}}_{\rm pMT}\right\rangle_{\rm sec} + \langle \dot{r}_{\rm pGW}\rangle_{\rm sec} \leq 0$ always holds according

Downloaded from https://academic.oup.com/mnras/article/543/4/3503/8287737 by guest on 06 February 2026

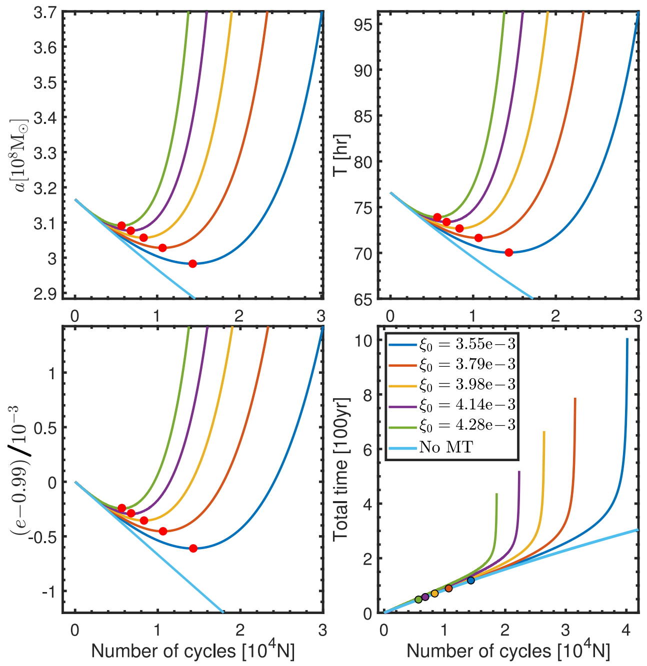

Figure 8. The synchronous evolution of a, T, e, and total time, respectively. The red marks indicate the points where a, T, and e reach their minimum values, and the coloured marks indicate total time reach its inflection value. The sky-blue curves (without markers) show evolution considering GW emission; they exhibit monotonic behaviour without any minima or inflection points.

to equation (40), we infer that the MT process of a WD in a bound high-eccentricity orbit around an IMBH is inherently irreversible.

Therefore, the long-term evolution for $\boldsymbol{f}^{\mathcal{B}}_{\mathrm{MT}}$ may lead to two possible outcomes:

(i) Tidal disruption scenario: The WD will be tidally disrupted if its pericentre distance r_p shrinks below the critical tidal radius r_t. Following established theory (Rees 1988), this occurs when $r_\mathrm{p} < r_\mathrm{t} \simeq R_\mathrm{WD}\,(M_\mathrm{IMBH}/M_\mathrm{WD})^{1/3}$. In our framework, this condition translates to a critical overflow disruption threshold $\epsilon_\mathrm{t}(q)$. For systems with extreme mass ratios ($q \ll 1$), this threshold approaches $\epsilon_\mathrm{t} = 1 - C_\mathrm{L} q^{-1/3} \sim 0.465$.

(ii) Ejection scenario: The WD may escape the system entirely if its orbital eccentricity reaches or exceeds unity ($e \geq 1$) before reaching the disruption threshold ($\epsilon < \epsilon_\mathrm{t}$).

The actual outcome depends sensitively on the initial conditions: First, systems starting near the critical ϵ_t boundary (initial ϵ_0 is slightly smaller than ϵ_t) overwhelmingly favour tidal disruption. WD will be tidally disrupted before the eccentricity reaches 1. Secondly, systems beginning with much lower initial overflow parameter $\epsilon_0 \ll \epsilon_\mathrm{t}$ typically lead to ejection. We also note that for $\boldsymbol{f}^{\mathcal{A}}_{\mathrm{MT}} = \boldsymbol{0}$, the case follows the description in Zalamea et al. (2010); tidal disruption is inevitable.

For numerical simulation, we consider spinless WD and IMBH with initial conditions: $e_0 = 0.99$, $\epsilon_0 = 0$, $m_{10} = 0.15\,\mathrm{M}_\odot$, and $m_{20} = 4 \times 10^5\mathrm{M}_\odot$. The dimensionless surface equivalent depth ξ_0 in equations (10) and (11) is used to adjust δM_WD, with values $\xi_0 \times 10^3 = 3.55$, 3.79, 3.98, 4.14, and 4.28.

In Fig. 8, we show the evolution of a, T, e, and the total elapsed time, respectively. Initially, with $\epsilon = 0$, gravitational radiation dominates, causing a, T, and e to decrease. After reaching the minimum, the three parameters begin to increase as the MT effect becomes dominant. The lower the initial value of ξ_0, the longer time it takes to reach the minimum, and the lower the minimum values. The evolution of the total elapsed time shows that, in the absence of the MT process, the slope decreases with increasing orbital cycles, corresponding to the decline in T due to gravitational radiation. After the inflection point, where the MT process becomes dominant, the slope increases, corresponding to the rise in T due to the MT effect. The red point on each curve marks the transition from GW-dominated evolution to an MT-dominated one. Fig. 8 is consistent with the evolution we predicted earlier in this section.

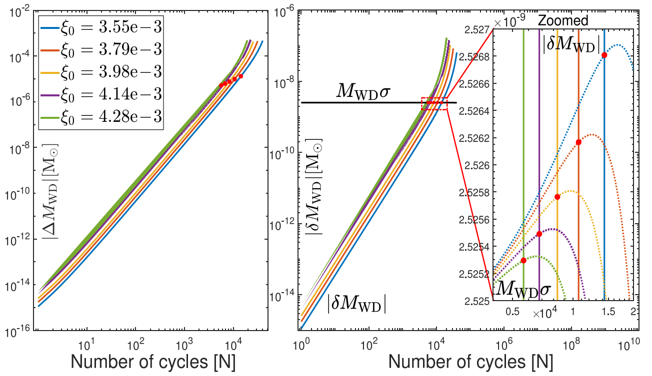

Figure 9. The evolution of M_WD over time due to the MT process. Left panel: cumulative mass-loss $|\Delta M_\mathrm{WD}|$ showing the total mass transferred from the WD between the initial state (cycle 0) and cycle N, calculated as $|M_\mathrm{WD}(\mathrm{N}) - M_\mathrm{WD}(0)|$. Right panel: per-cycle transferred mass $|\delta M_\mathrm{WD}|$ showing the mass lost by the WD in each individual cycle, calculated as $|M_\mathrm{WD}(\mathrm{N}) - M_\mathrm{WD}(\mathrm{N}-1)|$. The black curves represent different ξ_0 parameter values in the $M_\mathrm{WD}\sigma$ function. These curves are nearly indistinguishable at this scale due to their close clustering. The zoomed inset provides a magnified view comparing $|\delta M_\mathrm{WD}|$ (solid line) and $M_\mathrm{WD}\sigma$ (dashed line). The red markers indicate critical points where both orbital separation a and orbital period T reach their minimum values. These occur at the intersections of the $|\delta M_\mathrm{WD}|$ and $M_\mathrm{WD}\sigma$ curves.

In Fig. 9, we show the evolution of M_WD. The smaller ξ_0 requires more cycles to achieve the same mass, because it results in a lower MT rate $|\dot{m}_1|$. Although ξ_0 differs for each line, when $\left|\dot{a}^{\mathcal{B}}_{\mathrm{MT}}/\dot{a}_{\mathrm{GW}}\right|_{\mathrm{sec}} \to 1$, δM_WD remains almost unchanged (i.e. the values of red points in the right panel are nearly the same). This is because the size of σ in equation (35) is only related to q, e_r, and r_p. In the right panel, $M_\mathrm{WD}\sigma(\mathrm{N})$ shows little change (The black lines show curves for different values of ξ_0 of the function $M_\mathrm{WD}\sigma$, which are clustered together, with $\sigma \approx 1.7 \times 10^{-8}$). This function is closely tied to the initial conditions, and since all our evolutions use the same initial orbital parameters, the function's initial value is the same for each dashed line.

In Fig. 10, we show the evolution of overflow parameter $\epsilon(\mathrm{N})$. The presence or absence of MT significantly affects ϵ. From equations (26) and (28), the slope $\mathrm{d}\epsilon/\mathrm{dN}$ is about $\epsilon(\mathrm{N}) - \epsilon(\mathrm{N}-1)$ equal to $\left|\delta r_\mathrm{p}/r_\mathrm{p}\right| + 2/3\,|\delta M_\mathrm{WD}/M_\mathrm{WD}|$. The integral for $\epsilon(\mathrm{N})$ with $\epsilon(\mathrm{N}=0) = 0$ is

$$\begin{aligned}\epsilon(\mathrm{N}) &\simeq 1 - \frac{r_\mathrm{p}(\mathrm{N})}{r_\mathrm{p}(0)}\left(\frac{M_\mathrm{WD}(\mathrm{N})}{M_\mathrm{WD}(0)}\right)^{\frac{2+\gamma q(\mathrm{N})}{3}} \\ &\simeq -\frac{\Delta r_\mathrm{p}(\mathrm{N})}{r_\mathrm{p}(\mathrm{N})} - \frac{2+\gamma q(\mathrm{N})}{3}\frac{\Delta M_\mathrm{WD}(\mathrm{N})}{M_\mathrm{WD}(\mathrm{N})}, \qquad (42)\end{aligned}$$

where cumulative quantity $\Delta r_\mathrm{p}(\mathrm{N})$ is $r_\mathrm{p}(\mathrm{N}) - r_\mathrm{p}(0)$, and $\Delta M_\mathrm{WD}(\mathrm{N})$ is $M_\mathrm{WD}(\mathrm{N}) - M_\mathrm{WD}(0)$.

Downloaded from https://academic.oup.com/mnras/article/543/4/3503/8287737 by guest on 06 February 2026

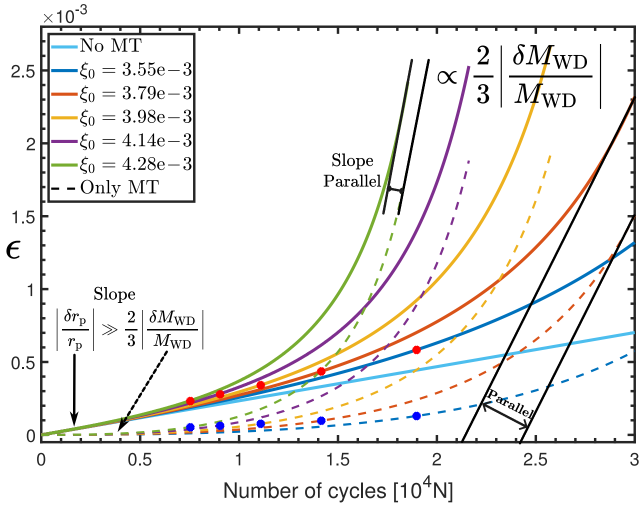

Figure 10. The evolution of $\epsilon = 1 - r_{\rm p}C_{\rm L}/R_{\rm WD}$ on long time-scale. The sky blue solid line is the evolution of ϵ without MT. The solid lines in other colours are the cases where both gravitational radiation and the MT process are considered (equation 42). The dashed lines are the function $1 - (M_{\rm WD}({\rm N})/M_{\rm WD}(0))^{(2+\gamma q({\rm N}))/3}$. The red and blue marks indicate the points where semimajor axis a reach the minimum.

Because the initial orbital parameters are the same, the initial slopes of solid lines in Fig. 10 are similar. For comparison, we also plot the function obtained by excluding the change in $r_{\rm p}$ (dashed line). This situation corresponds to considering only MT, without considering the change of GW emission for $r_{\rm p}$. When the MT effect is weak, ϵ is very small, and gravitational radiation dominates, causing $\left|\delta r_{\rm p}/r_{\rm p}\right| \gg |\delta M_{\rm WD}/M_{\rm WD}|$. According to equation (40), the change in $r_{\rm p}$ is entirely governed by GW emission. Therefore, the initial slope of the dashed line is nearly zero, reflecting that the MT effect is very weak at the beginning. Correspondingly, when the MT effect dominates, $\left|\delta r_{\rm p}/r_{\rm p}\right| \ll |\delta M_{\rm WD}/M_{\rm WD}|$; this relationship has also been shown in the numerical simulations in Section 4.3. Therefore, the slopes for the solid and dashed lines start to converge to $2/3\,|\delta M_{\rm WD}/M_{\rm WD}|$. The fundamental reason for this relationship is the radius–mass relationship of the WD shown in equation (8).

5.3 Verification of long-term results

In Sections 5.1 and 5.2, we computed the evolution of Newtonian elliptical orbits. In Section 4, we include the effects of PN dynamics terms, specifically the contributions of $\mathcal{A}$, $\mathcal{B}$, and the accelerations $\boldsymbol{a}_{\rm SO}$, $\boldsymbol{a}_{\rm SS}$, and $\boldsymbol{a}_{\rm SOPN}$ in equation (2). In long-term evolution, we observe minima in the evolution of orbital parameters (Fig. 8), and the MT rate approaches consistency near these minima (Fig. 9). In order to verify the correctness of the long-term results, it is necessary to obtain the same conclusions in short-term calculations. Orbital parameters (such as a, T, and e) should also reach their minima under relativistic corrections. When MT and gravitational radiation are in equilibrium, the transferred mass per cycle, $\delta M_{\rm WD}$, should remain unaffected by ξ_0, i.e. $|\delta M_{\rm WD}| = M_{\rm WD}\sigma$, when $\left|\dot{a}^{\mathcal{B}}{}_{\rm MT}/\dot{a}_{\rm GW}\right|_{\rm sec} = 1$. We aim to investigate the minimum of a during short-term evolution using parameters from Section 5.2, and analyse $\delta M_{\rm WD}$ near $a_{\rm min}$. In these short-term calculations, we do not assume a delta function for the MT rate $\dot{M}_{\rm WD}$ like equation (32) (we use equations 12 and 13), nor do we use the time-averaged orbital parameter change rate per cycle (we use equation 4). As these phenomena occur near the minimum, we focus on the evolution over 100 cycles to verify these conclusions. The initial orbital parameters for the short-term calculation are adjusted to correspond to those of the first few cycles before the minimum.

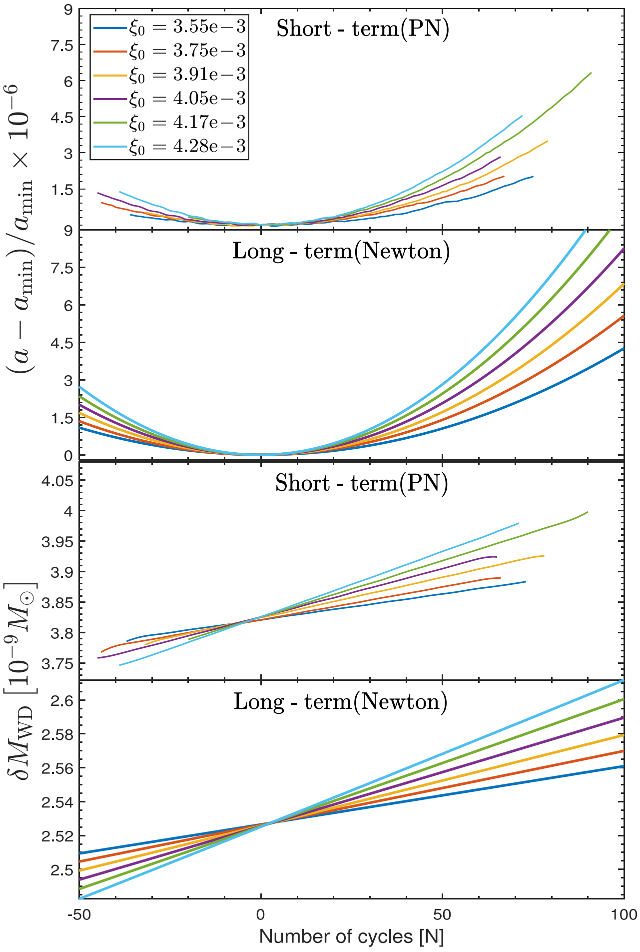

Figure 11. Comparison of the short-term and long-term evolution of $(a - a_{\rm min})/a_{\rm min}$ and $\delta M_{\rm WD}$. The short-term evolution uses the PN results from Section 4.3. The long-term evolution uses the Newtonian elliptical orbit results from Section 5.2. The x-axis is set to ${\rm N}(a_{\rm min}) = 0$.

In Fig. 11, we compare the short-term and long-term evolution of $(a - a_{\rm min})/a_{\rm min}$ and $\delta M_{\rm WD}$. Different surface densities parameter ξ_0 lead to varying minimum semimajor axis values $a_{\rm min}$. We normalize the results by the ratio $(a - a_{\rm min})/a_{\rm min}$. As ξ_0 increases, the rate of change of a accelerates, indicating that larger surface density of WD correspond to stronger MT effects.

We also show the variation of $\delta M_{\rm WD}$ near $a_{\rm min}$ in Fig. 11. According to equation (35), the value of $\delta M_{\rm WD}$ near $a_{\rm min}$ is independent on ξ_0. Therefore, for the same initial values of $r_{\rm p0}$, $e_{\rm r0}$, and q_0, the transferred mass $|\delta M_{\rm WD}|$ near $a_{\rm min}$ should converge into $M_{\rm WD}\sigma$. This convergence is well demonstrated in Fig. 11 for both short-term and long-term evolution. The reasoning behind this behaviour is explained in Fig. 9 (the quantity $M_{\rm WD}\sigma$ hardly changes) for long-term evolution, and it is confirmed from short-term evolution in Fig. 11.

Therefore, we confirm that the MT rate can be represented as a delta function at high eccentricity, and the time-averaged form can be used to calculate the evolution well. Furthermore, in the absence of effects other than MT and gravitational radiation, the evolution of orbital parameters inevitably exhibits extremal points.

Downloaded from https://academic.oup.com/mnras/article/543/4/3503/8287737 by guest on 06 February 2026

6 IMPACT ON GW SIGNAL AND DETECTION

As shown in Fig. 8, after the same evolution time around the IMBH, the orbital period of the WD with MT and gravitational radiation is longer than that with only gravitational radiation. When transferred mass $|\delta M_{\mathrm{WD}}|$ exceeds the limit value $M_{\mathrm{WD}}\sigma$ in equation (35), the period can even increase over time. Because of the change of period, the MT process induces a phase shift in the GW signal. Over a sufficiently long observational time, the accumulated phase difference due to MT can be detected. In the following text, we evaluate whether the MT could induce an accumulative phase shift as large as 1 rad over a period of $t_{\mathrm{obs}} = 5$ yr. Such a phase shift would be detectable by LISA and other space-based GW detectors (Kocsis, Yunes & Loeb 2011; Derdzinski et al. 2019; Zwick et al. 2022; Zhang et al. 2025).

Our orbit is highly eccentric, resulting in a non-linear evolution of the orbital phase over time, which complicates the calculation of the phase shift. In the GW waveform, significant change of the amplitude occurs near pericentre over very short durations, appearing as periodic pulses in the time domain (Poisson & Will 2014; Hughes et al. 2021; McCart, Osburn & Burton 2021). Since the period T changes very slowly due to the MT process, and the phase of each cycle always spans 2π, it is unnecessary to compute the exact phase as a function of time during each period for our purposes. Instead, we can estimate the period of each cycle, which is sufficient to address the problem. We can demonstrate that (Appendix D), for the same number of cycles, the difference in total time is directly proportional to the difference in phase.

By the proof in Appendix D, under the adiabatic approximation, we can simplify the calculation of phase evolution when two key conditions are met: (1) The number of orbital cycles N is significantly large. (2) The single orbital period T_{N} is much shorter than the cumulative duration of all previous cycle. When these conditions hold, we can approximate the total phase change by replacing continuous time t with the sum of all previous orbital periods. Here, integer N represents the number of cycles where the MT effect causes a phase lag of 1 rad.

The integer N satisfies the following inequality:

$$0 \le \frac{|\Delta u_g|}{2\pi}\,\frac{1-\varsigma_{\mathrm{N}}}{\varsigma_{\mathrm{N}}} - \frac{\sum_{\mathrm{k}=1}^{\mathrm{N}-1} T_{\mathrm{k}}\varsigma_{\mathrm{k}}}{T_{\mathrm{N}}\varsigma_{\mathrm{N}}} \le 1, \tag{43}$$

where Δu_g represents the phase difference we want (in our goal, $\Delta u_g = -1$), ς_{k} represents the difference between the period with and without MT in the kth cycle, i.e. $\varsigma_{\mathrm{k}} := (T_{\mathrm{k}} - T_{\mathrm{k}}{}^{*})/T_{\mathrm{k}} > 0$. Here, the superscript asterisk indicates that MT is not considered. Inequality (43) is equivalent to Inequality (D6a). For the integer N is calculated from Inequality (43), if the total time for the first $(\mathrm{N}-1)$ cycles is less than the observation time t_{obs} (in our goal, $t_{\mathrm{obs}} = 5$ yr), the phase shift caused by MT is observable within t_{obs}.

For a fixed mass combination, such as $m_1 = 0.15\,\mathrm{M}_{\odot}$, $m_2 = 4 \times 10^5\mathrm{M}_{\odot}$, $q = 3.75 \times 10^{-7}$, we use the long-term evolution of Newtonian elliptical orbits as described in Section 5.2. Therefore, only parameters e_0, ϵ_0, and ξ_0 need to be adjusted. The initial values of e_0 and ϵ_0 reflecting different initial periods and pericentre distances. We fix the variable $\xi_0 = 3.55 \times 10^{-3}$. Table 2 shows the time required for the phase difference to reach 1 rad. Table 3 shows the time required for the semimajor axis a to reach its minimum.

In both Tables 2 and 3, the time required to observe the desired phase shift Δu_g increases with increasing e_0 and decreasing ϵ_0. These time variations are related to the strength of MT. Increasing eccentricity e with a constant pericentre distance r_{p} reduces the critical phase f_0 over which MT occurs (equation C9), shortening the Roche lobe overflow time in one period and decreasing the transferred mass δM_{WD} (equation 38). This results in a weaker MT effect and a longer required time. Conversely, decreasing the pericentre distance r_{p} at constant eccentricity e increases ϵ, the Roche radius R_{L} decreases, leading to an increase in δM_{WD}. This strengthens the MT effect and reduces the required time.

Table 2. The time required for the phase difference to reach 1 rad, for the different initial e_0 and ϵ_0, with same $\xi_0 = 3.55 \times 10^{-3}$. The time unit is year.

e_0 ϵ_0	0.980	0.982	0.984	0.986	0.988	0.990	0.992	0.994
0	7.188	8.170	9.427	11.087	13.367	16.674	21.846	30.934
0.30e-4	4.267	4.785	5.436	6.280	7.413	9.013	11.437	15.521
0.60e-4	2.945	3.286	3.713	4.263	4.999	6.032	7.587	10.186
0.90e-4	2.266	2.524	2.847	3.262	3.816	4.593	5.760	7.707
1.20e-4	1.858	2.068	2.330	2.667	3.117	3.748	4.694	6.272
3.51e-4	0.847	0.941	1.059	1.210	1.412	1.695	2.119	2.826
3.73e-4	0.809	0.899	1.011	1.156	1.349	1.619	2.024	2.699
3.95e-4	0.775	0.861	0.969	1.107	1.292	1.551	1.938	2.584

Table 3. The time required for the semimajor axis a reaches its minimum value due to gravitational radiation and the MT process, for the different initial e_0 and ϵ_0, with same $\xi_0 = 3.55 \times 10^{-3}$. The time unit is year.

e_0 ϵ_0	0.980	0.982	0.984	0.986	0.988	0.990	0.992	0.994
3.51e-4	4.132	4.842	5.779	7.061	8.898	11.692	16.324	25.081
3.73e-4	2.147	2.514	3.003	3.668	4.620	6.078	8.487	13.047
3.95e-4	0.213	0.246	0.294	0.353	0.445	0.585	0.806	1.240

When the initial overflow parameter ϵ_0 is small, the time required for the phase difference to reach 1 rad (Table 2) is shorter than the time it takes for the semimajor axis a to reach its minimum (Table 3). However, for sufficiently large ϵ_0 (as shown in the last row of Tables 2 and 3), this trend reverses: the phase lag takes longer to reach 1 rad than the time needed for the semimajor axis to reach its minimum. This reversal arises because the phase difference accumulates gradually from an initial value of zero, whereas the MT process begins with a finite $\epsilon_0 > 0$, implying an initially strong MT effect. Therefore, when ϵ_0 is large, the orbital evolution rapidly becomes MT-dominated even before the phase difference becomes significant. In such scenarios, the GW signals could reveal not only the accumulated phase lag due to MT, but also the dynamical transition from GW-dominated to MT-dominated evolution.

For sufficiently large overflow ϵ_0 and small eccentricity e_0, the phase shift can be detected within the observation time t_{obs}. Our calculations indicate that for an initial eccentricity $e_0 \simeq 0.99$, the overflow parameter should exceed 10^{-4} to allow detection within t_{obs}. However, the corresponding pericentre distance $r_{\mathrm{p}} = (1-\epsilon)R_{\mathrm{WD}}/C_{\mathrm{L}}$ changes only slightly between $\epsilon = 10^{-4}$ and $\epsilon = 0$. This illustrates that even a tiny variation in pericentre distance r_{p} can lead to a significant difference in phase evolution time-scales, as reflected in Table 2. Therefore, the detectability of MT-induced signatures in GW signals is extremely sensitive to the precise value of ϵ_0.

7 DISCUSSION

7.1 Implications for QPEs

After our analysis, we conclude that the MT process may cause the WD to escape the gravitational potential of the IMBH (Section 5.2),

Downloaded from https://academic.oup.com/mnras/article/543/4/3503/8287737 by guest on 06 February 2026

potentially explaining the disappearance of the QPE signal in GSN 069, as reported by Miniutti, G. et al. (2023a, b). GSN 069, the first galactic nucleus to exhibit QPEs, was identified in 2018 December. These high-amplitude soft X-ray bursts recur approximately every 9 h, lasting about 1 h, with X-ray count rates increasing by up to two orders of magnitude from a stable quiescent level. However, following the XMM6 observation, eruptions have not been detected in subsequent exposures from 2020 May to 2021 December (XMM7–XMM11). The QPE reappeared in XMM12 observation in 2022 July after disappearing for 2.0 ± 0.5 yr (Miniutti, G. et al. 2023b). The new light curve features differ markedly from the previous ones.

To estimate the MT rate in the QPE light curve, we use the model of light curve for the partial TDE from the tidal stripping proposed by Rees (1988) and Ulmer (1999). The accretion luminosity of the stripped material falling back to the IMBH is $L(t) = \tilde{\eta}\dot{M}_{\rm IMBH}(t)c^2$, where $\tilde{\eta} = 0.1$ is the typical radiative efficiency (King 2020). The peak rate of mass gain of IMBH is $\delta M_{\rm WD}/3P_{\rm min}$, where $P_{\rm min}$ is the shortest Keplerian orbital period (Ulmer 1999; Wang et al. 2019). Thus, we can give a relationship between the peak of the light curve $L_{\rm peak}$ and the transferred mass $\delta M_{\rm WD}$ per cycle by the WD:

$$\delta M_{\rm WD} \simeq 2.5 \times 10^{-8}{\rm M}_{\odot} \left(\tfrac{\tilde{\eta}}{0.1}\right)^{-1} \left(\frac{L_{\rm peak}}{10^{42}\,{\rm erg\,s^{-1}}}\right) \left(\tfrac{P_{\rm min}}{1{\rm ks}}\right). \tag{44}$$

Based on the initial parameters provided in Sections 4 and 5, if $\delta M_{\rm WD}$ has the value given by equation (44), the MT effect on the orbit becomes dominant over gravitational radiation ($\delta M_{\rm WD}$ exceeds the value indicated by the red points in the right panel of Fig. 9).

In our model, when MT becomes dominant, the orbital period and eccentricity increase (Fig. 8), and the WD finally escapes from the gravitational potential of the IMBH. The lifetime of the WD–IMBH system, when MT dominates, is much shorter than the gravitational radiation time-scale, i.e. $t_{\rm life} \sim (1-e)/\langle \dot{e} \rangle_{\rm sec} \ll t_{\rm GW} \sim \left| (r_{\rm p} - R_{\rm t}) / \langle \dot{r}_{\rm pGW} \rangle_{\rm sec} \right|$ (use equations 39 and 40). The escape time-scale is approximately 10 to 10^2 yr. Higher surface densities parameter ξ_0 results in higher transferred mass $\delta M_{\rm WD}$, causing the WD to escape the system on a shorter time-scale. Therefore, for a low-mass WD core that has been stripped of its outer low-density surface, the time required to enter and escape the system will be short in 10 yr.

In addition, the MT rate is highly sensitive to the pericentre distance. For this escape to occur, the initial pericentre distance must be sufficiently large to avoid tidal disruption, i.e. $r_{\rm p}$ satisfies $\epsilon_0 = 1 - r_{\rm p}C_{\rm L}/R_{\rm WD} \ll \epsilon_{\rm t} \sim 1 - C_{\rm L}q^{-1/3}$ (see Section 5.2 for details).

The mechanism developed in our work accounts only for the dynamical escape of the WD from the gravitational potential of IMBH. The observed recurrence or reappearance of QPEs likely involves additional physical processes not captured in our model. One plausible explanation is the perturbative influence of external massive bodies – such as nearby high-speed moving stars (10–10^2 M$_{\odot}$), stellar-mass BHs (10^2 M$_{\odot}$), or even intermediate-mass BHs (10^4 M$_{\odot}$), which may induce gravitational focusing or orbital re-injection of the escaping WD. Some studies have considered the von Zeipel–Lidov–Kozai (ZLK) effect, which is the perturbation of the primary-secondary orbital system by a third party (such as another star or an IMBH) (Bode & Wegg 2013; Lei, Hanlun & Gong, Yan-Xiang 2022; Maeda & Okawa 2025). Through the ZLK cycle, the eccentricity and inclination of the orbit can be significantly adjusted, causing the WD to occasionally approach the primary BH, triggering the emission of QPEs.

7.2 The assumptions for MT

Equation (35) provides the MT rate when gravitational radiation and MT are in equilibrium. In this subsection, we will show that our MT rate is consistent with the estimates in King (2020, 2022), which use the gravitational radiation losses $(\dot{J}/J)_{\rm GW}$ to drive the MT rate.

According to King (2022, 2023), the dynamical stability of MT arises from the conservation of orbital angular momentum on a dynamical time-scale, which is much shorter than that for gravitational radiation losses. The accretion disc reaches an effectively steady state after a few orbital periods. After this, the disc passes almost all its angular momentum back to the orbit. This is the reabsorption of the original angular momentum of the mass transferred to the IMBH. As a result, conservation of orbital angular momentum forces the binary separation to increase, i.e. $\langle \dot{a}^{\mathcal{B}}_{\rm MT} \rangle_{\rm sec} > 0$. Our analysis of orbital evolution builds upon the orbital angular momentum analysis from King (2022) and the eccentric orbital dynamics with MT from Sepinsky et al. (2007b). Finally, we present a new possible scenario for orbital evolution.

We reconsider the condition $\langle \dot{R}_{\rm L}/R_{\rm L} - \dot{R}_{\rm WD}/R_{\rm WD} \rangle = 0$ in King (2022) and recalculate the expression using definitions $\varepsilon = 1 - C_{\rm L}D/R_{\rm WD}$ and $\epsilon = 1 - C_{\rm L}r_{\rm p}/R_{\rm WD}$:

$$\begin{aligned}\frac{\dot{R}_{\rm L}}{R_{\rm L}} - \frac{\dot{R}_{\rm WD}}{R_{\rm WD}} &= -\frac{\dot{\varepsilon}}{1-\varepsilon} = \frac{\dot{D}}{D} - \left(\frac{\dot{\epsilon}}{1-\epsilon} + \frac{\dot{r}_{\rm p}}{r_{\rm p}}\right) \qquad (45)\\ &= \frac{\dot{D}}{D} - \frac{\dot{m}_1}{m_1}\left[\frac{m_1}{R_{\rm WD}}\frac{\partial R_{\rm WD}}{\partial m_1} - \frac{q}{C_{\rm L}}\frac{\partial C_{\rm L}}{\partial q}(1+\gamma q)\right].\end{aligned}$$

Thus, we got the relationship between $\dot{\epsilon}$ and $\dot{r}_{\rm p}$ from $\dot{J}$:

$$\frac{\dot{\epsilon}}{1-\epsilon} = \frac{\dot{m}_1}{m_1}\left[\frac{\partial \ln R_{\rm WD}}{\partial \ln m_1} - \frac{\partial \ln C_{\rm L}}{\partial \ln q}(1+\gamma q)\right] - \frac{\dot{r}_{\rm p}}{r_{\rm p}}, \tag{46a}$$

$$\frac{\dot{r}_{\rm p}}{r_{\rm p}} = -\frac{\dot{m}_1}{m_1}\frac{2(1-\gamma q^2) + q(1-\gamma)}{1+q} - \frac{\dot{e}}{1+e} + \frac{2\dot{J}}{J}. \tag{46b}$$

If taking $R_{\rm WD} \propto m_1^{\zeta_1}$ and $C_{\rm L} \propto q^{\zeta_2}$, we obtain $\partial \ln R_{\rm WD}/\partial \ln m_1 = \zeta_1$ and $\partial \ln C_{\rm L}/\partial \ln q = \zeta_2$. Under the conditions $M_{\rm WD} \ll M_{\rm Ch}$ and $q \ll 1$, we can assume $\zeta_1 \rightarrow -1/3$ (equation 8) and $\zeta_2 \rightarrow 1/3$ (equation 16). Thus, if we further take $\gamma = 1$, which represents the conservation of mass, equation (46a) reduces to equation (12) in King (2022). The last term of equation (46b), the change in angular momentum, is driven only by gravitational radiation, which is much longer than the dynamical scale. The second term, the change in eccentricity, has additional MT effect, which further increases the MT rate.

King (2022) sets $\langle \dot{\epsilon}_{\rm MT} \rangle_{\rm sec} = 0$ in equation (45) in order to keep the MT rate stable in the long time, and show the effect of gravitational radiation losses $\dot{J}/J$ is to drive MT. And based on this, the orbit needs to be expanded (i.e. increases in semimajor axis, period, and eccentricity). But this setting is not the only possible choice for orbital expansion. Assuming orbital evolution starts from $\epsilon_0 = 0$ (as shown in Figs 8, 9, and 10), the transferred mass per cycle $|\delta M_{\rm WD}|$ always increases, and the orbital period also increases due to MT dominance; the change of the period is faster than the change of $|\delta M_{\rm WD}|$ (when the eccentricity approaches 1, the period approaches infinity).

The average MT rate $|\delta M_{\rm WD}/T|$ may reaches a maximum value and then decreases when the orbit expands. This reduction in average MT rate must require the MT process leading to orbit expansion.

Alternatively, the setting that the pericentre distance $r_{\rm p}$ remains unchanged, i.e. $\langle \dot{r}_{\rm pMT} \rangle_{\rm sec} = 0$ in equation (40), can also allow to orbital expansion. As shown in Section 3.3, the analysis of $J_{\rm orb}$ has given an expression for the component $\mathcal{S}$ (equation 20). From

Downloaded from https://academic.oup.com/mnras/article/543/4/3503/8287737 by guest on 06 February 2026

equation (4) for $\dot{p}$ and $\dot{e}$, the contribution of $\mathcal{S}$ is much larger than that of $\mathcal{R}$ at high eccentricity. Therefore, under different settings for component $\mathcal{R}$, the evolution of a, T, and e will not be different. They still evolve as shown in Fig. 8.

We set $\langle \dot{r}_{\mathrm{pMT}} \rangle_{\mathrm{sec}} = 0$ in this paper. For highly eccentric orbits, as discussed in Section 3.3, the acceleration $\boldsymbol{f}^{\mathcal{B}}_{\mathrm{MT}}$ is primarily significant near pericentre. Equation (21) shows that $\boldsymbol{f}^{\mathcal{B}}_{\mathrm{MT}}$ has almost no contribution to $\langle \dot{r}_{\mathrm{pMT}} \rangle_{\mathrm{sec}}$, taking $\langle \dot{r}_{\mathrm{pMT}} \rangle_{\mathrm{sec}} = 0$ at high eccentricity more reasonable than $\langle \dot{\epsilon}_{\mathrm{MT}} \rangle_{\mathrm{sec}} = 0$ in King (2022).

We can explain the orbital difference between the two settings: (i) setting equation (46a) to zero corresponds to $\langle \dot{\epsilon}_{\mathrm{MT}} \rangle_{\mathrm{sec}} = 0$, and (ii) setting equation (46b) to zero corresponds to $\langle \dot{r}_{\mathrm{pMT}} \rangle_{\mathrm{sec}} = 0$. However, only one of equations (46a) or (46b) can be set to zero, since $\dot{m}_1 \neq 0$ with MT. First, if $\langle \dot{\epsilon}_{\mathrm{MT}} \rangle_{\mathrm{sec}} = 0$, then $\langle \dot{r}_{\mathrm{pMT}} \rangle_{\mathrm{sec}} > 0$; MT leads to an increase in the pericentre distance, the orbital pericentre decay caused by gravitational radiation will be slowed down significantly. Secondly, if $\langle \dot{r}_{\mathrm{pMT}} \rangle_{\mathrm{sec}} = 0$, then $\langle \dot{\epsilon}_{\mathrm{MT}} \rangle_{\mathrm{sec}} > 0$, we have discussed the evolution of ϵ in this setting in Fig. 10.

To drive the MT rate, we average $\dot{J}_{\mathrm{orb}} / J_{\mathrm{orb}}$ in equation (17) over one orbital period and apply equation (32) to include δM_{WD}, accounting for gravitational radiation losses (Peters 1964):

$$\begin{aligned}
\left\langle \frac{\dot{J}_{\mathrm{orb}}}{J_{\mathrm{orb}}} \right\rangle_{\mathrm{MT\ sec}} &= \left(\frac{\delta M_{\mathrm{WD}}}{M_{\mathrm{WD}}} \right) \sqrt{\frac{G M_{\mathrm{WD}}}{c^2 a_{\mathrm{r}}} \frac{1}{2\pi} \frac{c}{a_{\mathrm{r}}}} (1-q) \sqrt{\frac{1+q}{q}} \tilde{h}, \\
\left\langle \frac{\dot{J}_{\mathrm{orb}}}{J_{\mathrm{orb}}} \right\rangle_{\mathrm{GW\ sec}} &= - \left(\frac{G M_{\mathrm{WD}}}{c^2 a_{\mathrm{r}}} \right)^3 \frac{32}{5} \frac{c}{a_{\mathrm{r}}} \frac{1+q}{q^2} \frac{1+\frac{7}{8}e_{\mathrm{r}}^2}{(1-e_{\mathrm{r}}^2)^{5/2}}.
\end{aligned} \tag{47}$$

Assuming $\langle \dot{J}_{\mathrm{orb}} / J_{\mathrm{orb}} \rangle_{\mathrm{MTsec}} \simeq \langle \dot{J}_{\mathrm{orb}} / J_{\mathrm{orb}} \rangle_{\mathrm{GWsec}}$, we obtain

$$\left| \frac{\delta M_{\mathrm{WD}}}{T} \right| \simeq \frac{M_{\mathrm{WD}}}{T} \tilde{\lambda}^{-5/2} q \frac{64}{5} \pi \frac{1+\frac{7}{8}e_{\mathrm{r}}^2}{(1+e_{\mathrm{r}})^{5/2}} \frac{\sqrt{1+q}}{(1-q)\tilde{h}}. \tag{48}$$

Here, $|\delta M_{\mathrm{WD}}/T|$ derived using this equation is the same as $(-\dot{M}_2)$ in equation (15) of King (2022). Equation (48) is similar to equation (35) for $\left| \dot{a}^{\mathcal{B}}{}_{\mathrm{MT}} / \dot{a}_{\mathrm{GW}} \right|_{\mathrm{sec}} = 1$. Therefore, the MT rate from King (2022) is consistent with our view that gravitational radiation and MT are equilibrium.

7.3 Mass-loss and angular momentum transfer

In Section 3.3, we derived the form of MT acceleration $\boldsymbol{f}^{\mathcal{B}}_{\mathrm{MT}}$, but we assume the conservation of mass and angular momentum in the mathematical treatment in the following sections. If these assumptions are relaxed, i.e. $\gamma < 1$, $\tilde{f} \neq 0$, and $\tilde{g} \neq 0$, the time required for WD ejection may change. However, we find that the lifetime $t_{\mathrm{life}} \sim (1-e) / \langle \dot{e} \rangle_{\mathrm{sec}}$ for the WD to escape is largely insensitive to the factor $\tilde{h}$. From equation (35), when MT balances gravitational radiation, the transferred mass scales as $|\delta M_{\mathrm{WD}}| \sim M_{\mathrm{WD}} \sigma \propto \tilde{h}^{-1}$. Meanwhile, the secular rate of change of eccentricity due to MT (equation 39) satisfies $\langle \dot{e}^{\mathcal{B}}_{\mathrm{MT}} \rangle_{\mathrm{sec}} \propto |\delta M_{\mathrm{WD}} / M_{\mathrm{WD}}| \, \tilde{h} \propto \sigma \tilde{h}$. Combining these relations reveals that the eccentricity evolution rate is effectively independent of $\tilde{h}$, as the dependence cancels out. Consequently, the escape time-scale t_{life}, which is closely linked to the eccentricity evolution, is not significantly affected by variations in factor $\tilde{h}$.

In addition, the non-conservation of orbital angular momentum may also affect the stripping mass; this helps us understand the evolution of WD. However, we do not know the exact values of these coefficients. We will not discuss the specific motion of MT flow in detail in this paper. We only make assumptions about the coefficients in equation (20). For the factor $\tilde{h}$, a zeroth expansion in the small mass ratio limit ($q \ll 1$) is $\tilde{h} = 1 - \gamma \tilde{f} + \mathcal{O}(q)$. The contribution from $\tilde{g}$ appears only in combination with q and can thus be neglected to leading order. Thus, we temporarily ignore the second term in equation (17). As an example, we take a typical parameter combination: $\gamma = \tilde{f} = 1/2$ (half of the mass escapes from the system, taking with it half of its specific angular momentum); this yields $\tilde{h} = 3/4$. Under this condition, the transferred mass required to balance GW losses (equation 35) increases relative to the conservative case ($\tilde{h} = 1$). Quantitatively, for $\tilde{h} = 3/4$, the required δM_{WD} increases by approximately 33 per cent. This implies a longer evolutionary path from $\epsilon = 0$ to equilibrium, though the time-scale remains broadly comparable.

An extreme scenario where $\tilde{h} \ll 1$ would require $\gamma \sim 1$ (most of the mass retained in the system) and $\tilde{f} \sim 1$ (almost no angular momentum is reconverted into orbital angular momentum); this combination that seems physically implausible. In high-eccentricity systems, the accretion disc circularizes on a few orbital periods, with a typical circular radius close to the orbital pericentre. As the WD continues to perturb the disc during each pericentre passage, the disc structure is periodically destabilized, facilitating the transfer of a non-negligible fraction of angular momentum back to the orbit. Such systems are unlikely to exhibit strongly non-conservative angular momentum behaviour.

7.4 Relativistic orbital correction for the transferred mass

In Section 5.1.2, for Keplerian elliptical orbits, equation (38) gives the transferred mass δM_{WD} during each orbital period. However, for high eccentricity ($e_{\mathrm{r}} \sim 0.99$) and small pericentre distance ($\tilde{\lambda} = r_{\mathrm{p}}/(G m_2/c^2) \sim 8$), this result should be corrected to account for the effects due to GR.

Using PN approximation, the $\dot{f}_{\mathrm{N}}$ in equation (37) should be replaced by $\mathrm{d}f/\mathrm{d}t$ in equation (4c). When the companion star ($q \ll 1$) has a high velocity near pericentre, the effect of relativistic corrections is significant; the geodesic equation in curved space–time becomes more applicable. If we use geodesic equations in Schwarzschild space–time instead, we can adopt $\mathrm{d}t/\mathrm{d}\psi$ from Cutler, Kennefick & Poisson (1994) and Martel (2004) to replace $\dot{f}_{\mathrm{N}}^{-1}$. Here, ψ is a phase parameter that controls radial motion. The final result for δM_{WD} is then given by

$$\begin{aligned}
\delta M_{\mathrm{WD}} \simeq \sum_{k=0}^{\infty} \Bigg\{ & F_k(\hat{p}) \cdot (1+e)^k \sqrt{1 + \frac{4(1-e^2)}{\hat{p}(\hat{p}-4)}} \times \\
& \frac{4\, C_{\dot{m}_1} r_{\mathrm{p}}^{3/2}}{\sqrt{Gm}} \sqrt{\frac{\epsilon}{2e}} \sum_{n=0}^{\infty} \sum_{m=0}^{\infty} C_{\varepsilon \mathrm{n}} \binom{n}{m} (-1)^m (1-\epsilon)^m \\
& \times \mathrm{AF1} \left[\frac{1}{2}; \frac{1}{2}, m-k+2; \frac{3}{2}; \frac{1+e}{2e}\epsilon, \epsilon \right] \Bigg\},
\end{aligned} \tag{49}$$

where the series $F_k(\hat{p})$ is derived in Appendix C. Here, $\hat{p}$ satisfies $p = \hat{p}(Gm/c^2) = r_{\mathrm{p}}(1+e)$, with $e = (r_{\mathrm{a}} - r_{\mathrm{p}})/(r_{\mathrm{a}} + r_{\mathrm{p}})$. The detailed derivation of equation (49) is provided in Appendix C.

The relativistic correction to the Schwarzschild space–time geodesic introduces the coefficients $F_k(\hat{p})(1+e)^k$ and $1 + 4(1-e^2)/\hat{p}(\hat{p}-4)$, which reduce to 1 in the 0PN limit. The coefficient $F_k(\hat{p})(1+e)^k$ is positive for any k, and for bound orbit that will not fall into central BH, i.e. $0 < e < 1$, $\hat{p} > 4$, we have $4(1-e^2)/\hat{p}(\hat{p}-4) > 0$. These coefficients collectively enhance δM_{WD} compared to equation (38), which is due to the orbital precession effect caused by GR. Since the orbital precession due to the Schwarzschild metric is prograde, the precession angle during one orbital period $\Delta\varphi$ is positive. This positive $\Delta\varphi$ increases the time interval during which $R_{\mathrm{WD}} > R_{\mathrm{L}}$, i.e. $\mathrm{d}t/\mathrm{d}\psi > \dot{f}_{\mathrm{N}}^{-1}$. Here, the expression for $dt/d\psi$ is provided in equation (C10). Because f_0

Downloaded from https://academic.oup.com/mnras/article/543/4/3503/8287737 by guest on 06 February 2026

satisfies $R_{\rm WD} = C_{\rm L} D(f_0)$ and we substitute D with $p/(1 + e\cos\psi)$, the value of f_0 remains consistent with equation (C9). The definite integral of $dt/d\psi$ from $-f_0$ to f_0 must be greater than that of $\dot{f}_{\rm N}^{-1}$.

As orbital eccentricity increases with same pericentre distance, the angular phase evolves more slowly, reflected by an increase in $dt/d\psi$ (see equation C10). This results in a longer pericentre interaction time and consequently enhances MT per orbit. For a quantitative example, a representative system with $m_1 = 0.15\,{\rm M}_\odot$, $q = 3.75 \times 10^{-7}$, $\epsilon = 5 \times 10^{-3}$, and $e = 0.985$, the relative difference in transferred mass between relativistic and Newtonian calculations is $(\delta M_{\rm WD}^{\rm R} - \delta M_{\rm WD}^{\rm NR})/\delta M_{\rm WD}^{\rm NR} \simeq 65$ per cent, where 'R' and 'NR' denote the relativistic and non-relativistic cases, respectively. This discrepancy highlights the importance of relativistic corrections in systems with extreme eccentricity and high velocity, where even subtle changes in orbital dynamics significantly affect MT efficiency.

The transferred mass per cycle, $\delta M_{\rm WD}$, obtained from equation (49), is consistent with that from our short-term PN orbital simulations (Section 4). These simulations incorporate the MT acceleration $\boldsymbol{f}_{\rm MT}^{\mathcal{B}}$ (equation 30) and the mass-loss rate $\dot{m}_1$ (equations 12 and 13). The deviation between the two approaches remains below 5 per cent, confirming the accuracy of the relativistic treatment.

7.5 Contribution of WD spin angular momentum

For a typical spin parameter of WD $\chi_1 \sim 0.1$, the corresponding orbital perturbation scales as $\chi_1 q$, rendering the resulting orbital modulation subdominant. The low spin value $\chi_1 \sim 0.1$ is expected, as the structure of WDs is supported by electron degeneracy pressure; excessive spin would lead to centrifugal forces exceeding gravitational binding, causing structural instability or disintegration (Poisson & Will 2014). Therefore, given the extreme mass ratio $q \ll 1$, the orbital influence of the WD's spin – through spin–orbit ($\boldsymbol{a}_{\rm SO}$), spin–spin ($\boldsymbol{a}_{\rm SS}$), and spin–PN ($\boldsymbol{a}_{\rm SOPN}$) acceleration terms – is negligible.

In contrast to the PN spin correction, the MT process exerts a more substantial influence on the dimensionless parameter $A = \Omega_1^2 D^3/Gm$, as introduced in Section 3.2. This parameter enters both the effective potential-density (equation 9) and the Lagrange point condition (equation B4), both of which are ultimately used to derive the transferred mass per orbit. These expressions are further expanded into series of $\delta M_{\rm WD}$ in equations (38) and (49). The impact of A manifests directly through the coefficients of these expansions. We first estimate the size of A at pericentre:

$$A = \frac{\Omega_1^2 r_{\rm p}^3}{Gm} = \left(\frac{R_{\rm WD}\Omega_1}{c}\right)^2 \left(\frac{R_{\rm WD}}{r_{\rm p}}\right)^{-2} \left(\frac{Gm}{c^2 r_{\rm p}}\right)^{-1}$$
$$= \frac{5}{4896}\frac{q}{1+q}\left(\frac{1-\epsilon}{C_{\rm L}}\right)^3 \frac{M_{\rm WD}^{4/3}}{{\rm M}_\odot M_{\rm Ch}^{1/3}}\left(\frac{\chi_1}{\tilde{\gamma}}\right)^2 = \frac{\varpi}{1+q}(1-\epsilon)^3, \tag{50}$$

where ϖ and $\tilde{\gamma}$ are given in equations (B12) and (B13).

For a representative system with $M_{\rm WD} = 0.15\,{\rm M}_\odot$, $q = 3.75 \times 10^{-7}$, $\epsilon = 5 \times 10^{-3}$, $\chi_1 = 0.1$, and $\tilde{\gamma} = 0.5$, we find $A = 1.86 \times 10^{-5} \gg \chi_1 q \sim 10^{-8}$. For coefficient $D_{\varepsilon 1}$ in equation (B16), we see that $\varpi C_{\rm L}/D_{\varepsilon 1} \gg \chi_1 q$. Therefore, the orbital effect induced by the spin of the WD is much weaker than the effect due to MT. However, $10^{-5} D_{\varepsilon 1}$ is still very small compared to $D_{\varepsilon 1}$, making it negligible.

7.6 Mass-loss through the L2 Lagrange point

In binary systems where the primary is significantly more massive than the secondary, MT from the secondary to the primary is typically dynamically stable, occurring through the inner Lagrange point L1. However, if the system evolves rapidly, mass-loss may also occur through the outer Lagrange point L2 (Linial & Sari 2017, 2023). It is essential to evaluate the conditions under which this L2 MT occurs.

Using the results of Sepinsky et al. (2007a), the position of the L2 point can be determined. In the limit of an extreme mass ratio ($q \to 0$), its distance from the donor is nearly identical to that of the L1 point. Generally, the equipotential surface volume at L2 exceeds that at L1. Assuming a small amount of mass is transferred, the WD's radius closely approximates the Roche radius at both L1 and L2. Therefore, the Roche radius $R_{\rm L2}$ at L2 can be estimated via a Taylor expansion around the calculated Roche radius $R_{\rm L1}$ at L1 (equation 16). We can approximate the volumetric radius by (Ritter 1988; Linial & Sari 2017)

$$R_{\rm L2} - R_{\rm L1} \approx \frac{\phi_2 - \phi_1}{GM_{\rm WD}/R_{\rm WD}^2} > 0, \tag{51}$$

where ϕ_2 is the potential at point L2, which can be approximated using the potential function

$$\phi(D, \tilde{X}_{\rm D}) = -\frac{Gm_2}{D}\left(\frac{q}{\tilde{X}_{\rm D}} + \frac{1}{2}A(1+q)\tilde{X}_{\rm D}^2 + \frac{1}{1-\tilde{X}_{\rm D}} - \tilde{X}_{\rm D}\right), \tag{52}$$

where $\tilde{X}_{\rm D} = \tilde{X}/D$. Thus, the approximate value of $\phi_2 - \phi_1$ is

$$\phi_2 - \phi_1 \approx \phi(D, -\tilde{X}_1) - \phi(D, \tilde{X}_1) = 2\frac{Gm_2}{D}\frac{\tilde{X}_1^3}{1-\tilde{X}_1^2}. \tag{53}$$

For $A \to 0$ at pericentre, the result of $\phi_2 - \phi_1$ is $GM_{\rm WD}/D$. So we can get $(R_{\rm L2} - R_{\rm L1})/R_{\rm WD} \approx R_{\rm WD}/D$. We define dimensionless overflow parameter $\varepsilon_{1,2} := \left(R_{\rm WD} - R_{\rm L1,2}\right)/R_{\rm WD}$ at L1 and L2, so $\varepsilon_1 - \varepsilon_2 \approx R_{\rm WD}/D$.

If MT through L2 is non-negligible, the condition is (i) MT occurs at L2, i.e. $R_{\rm L2} < R_{\rm WD}$; it means $\varepsilon_2 > 0$ and $\varepsilon_1 > R_{\rm WD}/D$; (ii) the magnitude of ε_1 and ε_2 must be comparable, i.e. $(\varepsilon_1 - \varepsilon_2)/\varepsilon_1 \sim \mathcal{O}(10^{-1})$. Conversely, if $\varepsilon_1 < R_{\rm WD}/D$ or $\varepsilon_1 \sim R_{\rm WD}/D$, i.e. $\varepsilon_2 < 0$ or $\varepsilon_1 \gg \varepsilon_2$, MT through L2 can be neglected.

Here, we consider the regime in which the transferred mass $\delta M_{\rm WD}$ per cycle is very small – consistent with the amounts required to produce QPEs (see Section 7.1 for a detailed discussion). For typical QPEs, $\delta M_{\rm WD} \sim 10^{-8}$–$10^{-6}\,{\rm M}_\odot$. Numerical results in Figs 9 and 10 show that, for systems where the WD remains bound, $\delta M_{\rm WD} < 2 \times 10^{-7}{\rm M}_\odot$ and $\varepsilon_1 < 3 \times 10^{-3} < R_{\rm WD}/r_{\rm p} \sim 3.95 \times 10^{-3}$. This indicates that from the onset of MT ($\varepsilon_1 > 0$) to the time it escapes from the system ($e > 1$), the condition $\varepsilon_2 < 0$ or $\varepsilon_1 \gg \varepsilon_2$ holds throughout. Therefore, in the analysis of this article, MT from L2 is not considered.

7.7 Impact of GR on the Roche radius

In EMRI systems, the intense gravitational field of the IMBH significantly alters tidal forces compared to Newtonian expectations. This affects the transferred mass of each cycle. The relativistic Roche radius is smaller than its Newtonian counterpart at the same orbital separation. Determining this relativistic Roche radius is complex, necessitating the use of Fermi normal coordinates (FNCs) to account for the curved space–time's gravitational potential. In FNCs, the space–time geometry of the BH is expanded in the vicinity of a timelike geodesic that approximately tracks the CM motion of the star and debris (Fishbone 1973; Marck 1983; Ishii, Shibata & Mino 2005; Cheng & Evans 2013; Cheng & Bogdanović 2014; Banerjee et al. 2019; Maeda, Gupta & Okawa 2023).

Downloaded from https://academic.oup.com/mnras/article/543/4/3503/8287737 by guest on 06 February 2026

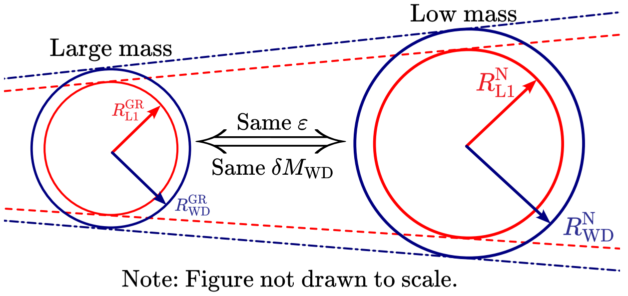

Figure 12. Schematic diagram explaining the mass compensation relation of GR and Newton in Section 7.7. GR corrections reduce the Roche radius compared to the Newtonian case at fixed pericentre distance.

Incorporating fully relativistic MT is complex, thus we compensate from different perspectives. In our model, the Roche radius is used solely to estimate the transferred mass per orbit. This is introduced via the overflow parameter $\varepsilon = (R_{\mathrm{WD}} - R_{\mathrm{L}})/R_{\mathrm{WD}}$, which quantifies the extent to which the WD overfills its Roche lobe. Our analysis begins with the observed periodicity of QPEs, requiring the orbital period to match observations. As a result, the pericentre distance and eccentricity are constrained by our previous results (Sections 4and 5). Within this framework, the transferred mass can be modulated not only by adjusting orbital parameters (r_{p} and e), but also by varying the WD mass, which directly affects its radius R_{WD}.

Importantly, as shown in Fig. 12, at a fixed orbital separation, a more massive WD (with smaller radius) under the relativistically corrected Roche radius yields a similar MT effect (same ε) to a less massive WD (with larger radius) under the Newtonian approximation. Thus, the relativistic correction to the Roche radius can be interpreted as effectively increasing the WD mass at a fixed pericentre. We can therefore estimate the additional mass required for the WD to reach the same overflow ε as in the Newtonian case.

To achieve the same overflow ε, the radius of WD should decrease proportionally, i.e. $R^{\mathrm{GR}}_{\mathrm{WD}}/R^{\mathrm{N}}_{\mathrm{WD}} = R^{\mathrm{GR}}_{\mathrm{L1}}/R^{\mathrm{N}}_{\mathrm{L1}} < 1$. The relativistic correction to the Roche radius can be estimated by considering the shift in the location of the Lagrange point L1 under relativistic gravity. Neglecting the change in the overall shape of the Roche lobe, we assume that the variation in the Roche radius is proportional to the change in the distance between the L1 point and the CM of the WD, i.e. $R_{\mathrm{L1}} \propto \tilde{X}_1$. This approximation offers a practical method to quantify the relativistic modification to the Roche limit without necessitating a comprehensive geometric analysis of the Roche lobe.

By constructing the quadrupole tidal tensor in FNCs, the corresponding gravitational potential can be derived. Utilizing the formalism presented by Marck (1983), Ishii et al. (2005), and Cheng & Evans (2013), the relativistic correction to the position of the Lagrange point L1 in the Schwarzschild metric is computed by solving $\nabla\phi^{\mathrm{GR}} = 0$. Here, the corrected potential in FNCs is

$$\phi^{\mathrm{GR}}(D, \tilde{X}_{\mathrm{D}}) = -\frac{Gm_2}{D}\left[\frac{q}{\tilde{X}_{\mathrm{D}}} + \frac{1}{1-\tilde{X}_{\mathrm{D}}} - \tilde{X}_{\mathrm{D}} + \frac{1}{2}\hat{\mathrm{C}}\tilde{X}^2_{\mathrm{D}}\right], \tag{54}$$

where $\hat{\mathrm{C}} = 3\hat{L}^2/\hat{D}^2$ (Quadrupole moment correction in GR) and $D = \hat{D}Gm_2/c^2$. Specifically, the shift in distance between L1 and the WD's CM can be expressed as a series expansion:

$$\tilde{X}^{\mathrm{GR}}_1 = \tilde{X}^{\mathrm{N}}_1\left[1 - \mathrm{K}_1(q)\frac{\hat{L}^2}{\hat{r}^2_{\mathrm{p}}} + \mathrm{K}_2(q)\frac{\hat{L}^4}{\hat{r}^4_{\mathrm{p}}} + O\left(\frac{\hat{L}^6}{\hat{r}^6_{\mathrm{p}}}\right)\right], \tag{55}$$

where $\hat{r}_{\mathrm{p}}$ is the dimensionless pericentre distance parameter, i.e. $\hat{r}_{\mathrm{p}} = \hat{p}/(1+e)$, and $\hat{L}$ is the dimensionless orbital angular momentum. For marginally bound orbits with $\hat{E} \to 1$, then $\hat{L}^2 \to \hat{p}^2/(\hat{p}-4)$. These dimensionless quantities arise in relativistic geodesic calculations (Cheng & Evans 2013).

In the extreme mass-ratio limit ($q \to 0$), the coefficients $\mathrm{K}_1(0) = \mathrm{K}_2(0) = 1/2$. For pericentre $\hat{r}_{\mathrm{p}} = 7.875$, the ratio $R^{\mathrm{GR}}_{\mathrm{L1}}/R^{\mathrm{N}}_{\mathrm{L1}} \approx \tilde{X}^{\mathrm{GR}}_1/\tilde{X}^{\mathrm{N}}_1 \approx 0.9$. This reflects the fact that the Roche radius in GR is smaller than in the Newtonian case, due to the stronger gravitational field in GR. From equation (8), $R^{\mathrm{GR}}_{\mathrm{WD}}/R^{\mathrm{N}}_{\mathrm{WD}} = R^{\mathrm{GR}}_{\mathrm{L1}}/R^{\mathrm{N}}_{\mathrm{L1}}$ implies $M^{\mathrm{GR}}_{\mathrm{WD}}/M^{\mathrm{N}}_{\mathrm{WD}} = \left(R^{\mathrm{GR}}_{\mathrm{WD}}/R^{\mathrm{N}}_{\mathrm{WD}}\right)^{-3} \approx 1.43$. Therefore, a WD with mass $0.15\mathrm{M}_{\odot}$ (in the Newtonian case) have mass $0.21\mathrm{M}_{\odot}$ in the relativistic case to produce the same transferred mass. In this way, relativistic corrections to the tidal field are effectively incorporated.

In addition, the spin of the IMBH modulates the tidal field as a function of latitude, potentially leading to periodic variations in the MT rate near pericentre for inclined (non-equatorial) orbits. However, the spin-induced tidal effects are both complex and expected to be subdominant in the regimes considered here. For this reason, they are neglected in the present analysis.

8 SUMMARY AND CONCLUSION

In this paper, we investigate the orbital evolution of high-eccentricity WD–IMBH systems under the influence of MT. We adopt the formulations developed by Sepinsky et al. (2007a, b) to derive the governing equations and perform numerical analyses. Our treatment of angular momentum follows insights from QPE studies by King (2020, 2022, 2023). We give the MT-induced acceleration $\boldsymbol{f}_{\mathrm{MT}}$ using the analysis of the time derivative of orbital angular momentum J_{orb} (Section 3.3). We use the perturbed Kepler method to calculate the orbital parameter evolution, and use the Roche lobe model to determine the MT rate $\dot{M}_{\mathrm{WD}}$. Our conclusions come from the analysis of the evolution under these dynamical formulas.

We calculate the evolution where the orbits are relativistically precessed and the IMBH has spin, and analyse the impact of MT on the orbits in this case in Section 4. We find that, despite using the PN approach, the trajectory of the WD closely follows the geodesic motion expected in Kerr space–time, with only jitter induced by spin-dependent acceleration terms (see Table 1 and Fig. 5). Furthermore, our results suggest that, as predicted, MT offsets the effects of gravitational radiation in eccentricity and orbital period, and greatly promotes the MT process itself. The change in overflow parameter far exceeds that from GWs alone, which means the mass stripping process rapidly widens the gap between the WD's radius and its Roche radius.

We find that the effects of gravitational radiation on the semimajor axis a, period T, and eccentricity e are counteracted by MT. When MT and gravitational radiation on the semimajor axis a reach equilibrium, (i.e. the average change rate of a due to the two processes can cancel each other out), the transferred mass δM_{WD} per cycle in equation (35) is very small, due to the high eccentricity of the orbit. Our simulations show that under such conditions, the orbital parameters a, T, and e reach minimum values during evolution, as shown in Fig. 8. When considering only MT and gravitational radiation, and the initial pericentre distance is far from the tidal radius, the WD will escape the gravitational potential of the

Downloaded from https://academic.oup.com/mnras/article/543/4/3503/8287737 by guest on 06 February 2026

IMBH. Our results suggest a qualitatively different picture of long-term orbital evolution compared to previous studies, highlighting the importance of including both MT feedback and relativistic corrections in models of WD–IMBH systems.

We anticipate that the MT process may impart sufficient recoil to cause the WD to escape the gravitational influence of IMBH, which could naturally explain the disappearance of QPE signal (Miniutti, G. et al. 2023b). Our analysis suggests that systems with higher per-orbit transferred mass, $\delta M_{\rm WD}$, are more susceptible to rapid escape, shortening the time-scale for the WD to leave the system. We find that the amount of transferred mass is highly sensitive to the difference between the WD radius and the Roche radius, such that even small variations in this gap can produce large changes in the transferred mass per cycle.

We find that MT effects can imprint observable signatures on the GW signal. As MT perturbs the orbital eccentricity and extends the orbital period, a cumulative phase delay emerges when compared with a system driven solely by GW emission. In particular, we introduce Inequality (43), which provides an analytic criterion for estimating the phase shift induced by MT. Over a 5-yr GW observation period, we compute the accumulated phase shift (Table 2) and the time at which a reaches its minimum (Table 3). Our results show that, for systems with modest initial eccentricity and sufficiently large pericentre distance, the MT-induced phase shift could be detectable by future GW observatories.

Incorporating MT dynamics into waveform models is thus crucial for accurate source characterization in eccentric EMRIs. MT modifies the phase evolution of the GW signal, affecting key observable parameters such as the component masses, eccentricity, and orbital evolution history. It also reveals the intricate interplay between GW-driven inspiral and MT-driven orbital expansion, offering a more complete picture of the lifecycle of WD–IMBH binaries. To fully capture the MT signature, joint EM and GW observations are essential, with space-based GW detectors triggered alerts playing a critical role in identifying and monitoring these events (Sesana et al. 2008; Holley-Bockelmann et al. 2020; Torres-Orjuela et al. 2024; Li et al. 2025).

ACKNOWLEDGEMENTS

We appreciate Yucheng Yin, Han Yan, and Di Wang for insightful discussions. We also thank the anonymous referee for their constructive and insightful comments that have improved the clarity and quality of this manuscript. JY is supported by the National Key Research and Development Program of China (grant No. 2021YFC2203003), the National Natural Science Foundation of China (grant No. 12247101), and the '111 Center' under grant No. B20063. XC is supported by the Natural Science Foundation of China (grant No. 12473037).

DATA AVAILABILITY

The data underlying this article will be shared on reasonable request to the corresponding author.

REFERENCES

Amaro-Seoane P., 2018, Living Rev. Relativ., 21, 4

Amaro-Seoane P., Gair J. R., Freitag M., Miller M. C., Mandel I., Cutler C. J., Babak S., 2007, Class. Quantum Gravity, 24, R113

Amaro-Seoane P. et al., 2017, Laser Interferometer Space Antenna, preprint (arXiv:1702.00786), https://arxiv.org/abs/1702.00786

Arcodia R. et al., 2022, A&A, 662, A49

Arcodia R. et al., 2024, A&A, 690, A80

Arcodia R. et al., 2021, Nature, 592, 704

Banerjee P., Paul S., Shaikh R., Sarkar T., 2019, Phys. Lett. B, 795, 29

Barack L., Cutler C., 2004, Phys. Rev. D, 69, 082005

Barsanti S., 2024, PhD thesis, Università degli Studi di Roma 'La Sapienza'

Berry C. P. L., Gair J. R., 2012, in Auger G., Binétruy P., Plagnol E., eds, ASP Conf. Ser. Vol. 467, Extreme-mass-ratio Bursts from the Galactic Centre. Astron. Soc. Pac., San Francisco, p. 185

Blanchet L., 2024, Living Rev. Relativ., 27, 4

Bode J. N., Wegg C., 2013, MNRAS, 438, 573

Bogdanović T., Cheng R. M., Amaro-Seoane P., 2014, ApJ, 788, 99

Cehula J., Pejcha O., 2023, MNRAS, 524, 471

Chakraborty J., Kara E., Masterson M., Giustini M., Miniutti G., Saxton R., 2021, ApJ, 921, L40

Chen X., Maxted P. F. L., Li J., Han Z., 2017, MNRAS, 464, 1874

Chen X., Qiu Y., Li S., Liu F. K., 2022, ApJ, 930, 122

Cheng R. M., Bogdanović T., 2014, Phys. Rev. D, 90, 064020

Cheng R. M., Evans C. R., 2013, Phys. Rev. D, 87, 104010

Cufari M., Coughlin E. R., Nixon C. J., 2022, ApJ, 929, L20

Cutler C., Kennefick D., Poisson E., 1994, Phys. Rev. D, 50, 3816

Danby J. M. A., 1962, Fundamentals of Celestial Mechanics. Macmillan, New York

Derdzinski A. M., D'Orazio D., Duffell P., Haiman Z., MacFadyen A., 2019, MNRAS, 486, 2754

Dosopoulou F., Kalogera V., 2016, ApJ, 825, 70

Efroimsky M., 2002, Equations for the orbital elements. Hidden symmetry, Preprint No.arXiv:1844, Institute for Mathematics and Its Applications, University of Minnesota

Efroimsky M., 2005, Annals of the New York Academy of Sciences, 1065, 346

Efroimsky M., Goldreich P., 2003, J. Math. Phys., 44, 5958

Efroimsky M., Goldreich P., 2004, A&A, 415, 1187

Fishbone L. G., 1973, ApJ, 185, 43

Fitzpatrick P.M., 1970, Principles of Celestial Mechanics. Academic Press, New York

Fitzpatrick R., 2012, An Introduction to Celestial Mechanics. Cambridge Univ. Press, Cambridge

Freitag M., 2001, Class. Quantum Gravity, 18, 4033

Fujita R., Hikida W., 2009, Class. Quantum Gravity, 26, 135002

Gair J. R., 2009, Class. Quantum Gravity, 26, 094034

Gair J. R., Babak S., Sesana A., Amaro-Seoane P., Barausse E., Berry C. P. L., Berti E., Sopuerta C., 2017, J. Phys. Conf. Ser., 840, 012021

Garain D., Sarkar T., 2024, Partial tidal disruptions of spinning eccentric white dwarfs by spinning intermediate mass black holes. Planetary and Space Science, 113–114, 78–99. https://arxiv.org/abs/2401.17031

Giustini Margherita, Miniutti Giovanni, Saxton Richard D., 2020, A&A, 636, L2

Giustini Margherita et al., 2024, A&A, 692, A15

Hills J. G., 1988, Nature, 331, 687

Hils D., Bender P. L., 1995, ApJ, 445, L7

Holley-Bockelmann K. et al., 2020, Getting Ready for LISA: The Data, Support and Preparation Needed to Maximize US Participation in Space-Based Gravitational Wave Science, preprint (arXiv:2012.02650), https://arxiv.org/abs/2012.02650

Hughes S. A., Warburton N., Khanna G., Chua A. J. K., Katz M. L., 2021, Phys. Rev. D, 103, 104014

Ishii M., Shibata M., Mino Y., 2005, Phys. Rev. D, 71, 044017

Istrate A. G., Tauris T. M., Langer N., Antoniadis J., 2014, A&A, 571, L3

Ivanov P. B., Papaloizou J. C. B., 2007, A&A, 476, 121

Jackson B., Arras P., Penev K., Peacock S., Marchant P., 2017, ApJ, 835, 145

King A., 2020, MNRAS, 493, L120

King A., 2022, MNRAS, 515, 4344

King A., 2023, MNRAS, 520, L63

Kocsis B., Yunes N., Loeb A., 2011, Phys. Rev. D, 84, 024032

Kolb U., Ritter H., 1990, A&A, 236, 385

Krolik J. H., Linial I., 2022, ApJ, 941, 24

Lei Hanlun, Gong Yan-Xiang, 2022, A&A, 665, A62

Li Z., Chen X., Chen H.-L., Han Z., 2019, ApJ, 871, 148

Downloaded from https://academic.oup.com/mnras/article/543/4/3503/8287737 by guest on 06 February 2026

Li E.-K. et al., 2025, Rep. Prog. Phys., 88, 056901
Linial I., Sari R., 2017, MNRAS, 469, 2441
Linial I., Sari R., 2023, ApJ, 945, 86
Lu W., Quataert E., 2023, MNRAS, 524, 6247
Lubow S. H., Shu F. H., 1975, ApJ, 198, 383
Luminet J. P., Pichon B., 1989, A&A, 209, 103
Maeda K.-i., Okawa H., 2025, Phys. Rev., 112, 044014
Maeda K.-i., Gupta P., Okawa H., 2023, Phys. Rev. D, 108, 123041
Marchant Pablo, Pappas Kaliroë M. W., Gallegos-Garcia Monica, Berry Christopher P. L., Taam Ronald E., Kalogera Vicky, Podsiadlowski Philipp, 2021, A&A, 650, A107
Marck J. A., 1983, Proc. R. Soc. A, 385, 431
Martel K., 2004, Phys. Rev. D, 69, 044025
McCart J., Osburn T., Burton J. Y. J., 2021, Phys. Rev. D, 104, 084050
Menou K., Haiman Z., Kocsis B., 2008, New Astron. Rev., 51, 884
Miniutti G., Giustini M., Arcodia R., Saxton R. D., Read A. M., Bianchi S., Alexander K. D., 2023a, A&A, 670, A93
Miniutti G., Giustini M., Arcodia R., Saxton R. D., Chakraborty J., Read A. M., Kara E., 2023b, A&A, 674, L1
Miniutti G. et al., 2019, Nature, 573, 381
Murray C. D., Dermott S. F., 2000, Solar System Dynamics. Cambridge Univ. Press, Cambridge
Olver F., Lozier D., Boisvert R., Clark C., 2010, The NIST Handbook of Mathematical Functions. Cambridge Univ. Press, Cambridge
Pavlovskii K., Ivanova N., 2015, MNRAS, 449, 4415
Peters P. C., 1964, Phys. Rev., 136, B1224
Poisson E., Will C. M., 2014, Gravity: Newtonian, Post-Newtonian, Relativistic. Cambridge Univ. Press, Cambridge
Rees M. J., 1988, Nature, 333, 523
Ritter H., 1988, A&A, 202, 93
Schmidt W., 2002, Class. Quantum Gravity, 19, 2743
Sepinsky J. F., Willems B., Kalogera V., 2007a, ApJ, 660, 1624
Sepinsky J. F., Kalogera B. Willems V., Rasio F. A., 2007b, ApJ, 667, 1170
Sesana A., Vecchio A., Eracleous M., Sigurdsson S., 2008, MNRAS, 391, 718
Seymour P. A. H., 1984, Phys. Bull., 35, 73
Speri L., 2024, PhD thesis: Advancing Gravitational Wave Astronomy: Novel Methodologies for Data Analysis and Waveform Modelling of Nanohertz and Millihertz Signals. Humboldt University of Berlin, Mathematisch-Naturwissenschaftliche Fakultat, (accessed 27 August 2025).
Sterne T. E., 1960, An Introduction to Celestial Mechanics. Interscience Tracts on Physics and Astronomy, Interscience Publishers, New York
Sun M., Arras P., 2018, ApJ, 858, 14
Tagoshi H., Ohashi A., Owen B. J., 2001, Phys. Rev. D, 63, 044006
Torres-Orjuela A. et al., 2024, GWnext 2024: Meeting Summary, preprint (arXiv:2406.03498), https://arxiv.org/abs/2406.03498
Ulmer A., 1999, ApJ, 514, 180
Wang Di, 2024, A&A, 687, A295
Wang Y. Y., Wang F. Y., Zou Y. C., Dai Z. G., 2019, ApJ, 886, L22
Wang M., Yin J., Ma Y., Wu Q., 2022, ApJ, 933, 225
Zalamea I., Menou K., Beloborodov A. M., 2010, MNRAS, 409, L25
Zhang Z.-H., Liu T., Yu S., Guo Z.-K., 2025, Phys. Rev. D, 111, 043049.
Zhao Z. Y., Wang Y. Y., Zou Y. C., Wang F. Y., Dai Z. G., 2022, A&A, 661, A55
Zwick L., Derdzinski A., Garg M., Capelo P. R., Mayer L., 2022, MNRAS, 511, 6143

APPENDIX A: A SHORT REVIEW OF THE PERTURBED KEPLER METHOD

The literature on the Perturbed Kepler Method is extensive (Sterne 1960; Danby 1962; Fitzpatrick 1970; Efroimsky 2002; Efroimsky & Goldreich 2003, 2004; Fitzpatrick 2012; Poisson & Will 2014; Dosopoulou & Kalogera 2016). Here, we provide a brief overview of the formalism (Poisson & Will 2014), focusing on approaches that do not employ Lagrangian or Hamiltonian mechanics.

The first time derivative of $\boldsymbol{r}$ and $\boldsymbol{v}$ are

$$\frac{\mathrm{d}\boldsymbol{r}}{\mathrm{d}t} = \frac{\partial \boldsymbol{r}_{\mathrm{Kepler}}}{\partial f}\frac{\mathrm{d}f}{\mathrm{d}t} + \sum_a \frac{\partial \boldsymbol{r}_{\mathrm{Kepler}}}{\partial \mu^a}\frac{\mathrm{d}\mu^a}{\mathrm{d}t} = \boldsymbol{v}_{\mathrm{Kepler}}\ \left(f(t), \mu^a(t)\right),$$

$$\frac{\mathrm{d}\boldsymbol{v}}{\mathrm{d}t} = \frac{\partial \boldsymbol{v}_{\mathrm{Kepler}}}{\partial f}\frac{\mathrm{d}f}{\mathrm{d}t} + \sum_a \frac{\partial \boldsymbol{v}_{\mathrm{Kepler}}}{\partial \mu^a}\frac{\mathrm{d}\mu^a}{\mathrm{d}t} = \boldsymbol{a},$$

where $\mu^a = (p, e, \omega, \Omega, \iota)$. For Perturbed Kepler method, we further obtain

$$\frac{\partial \boldsymbol{r}_{\mathrm{Kepler}}}{\partial f}\left(\frac{df}{dt} - \dot{f}_{\mathrm{N}}\right) + \sum_a \frac{\partial \boldsymbol{r}_{\mathrm{Kepler}}}{\partial \mu^a}\frac{d\mu^a}{dt} = \boldsymbol{0},$$

$$\frac{\partial \boldsymbol{v}_{\mathrm{Kepler}}}{\partial f}\left(\frac{df}{dt} - \dot{f}_{\mathrm{N}}\right) + \sum_a \frac{\partial \boldsymbol{v}_{\mathrm{Kepler}}}{\partial \mu^a}\frac{d\mu^a}{dt} = \boldsymbol{f},$$

where $\dot{f}_{\mathrm{N}}$ is defined as in equation (6). The six equations describe the time evolution of six unknown functions $(p, e, f, \omega, \Omega, \iota)$. From a mathematical perspective, each of these functions has a solution. However, solving the equations directly is complex and challenging (Dosopoulou & Kalogera 2016).

The vectors $\boldsymbol{r}_{\mathrm{Kepler}}$ and $\boldsymbol{v}_{\mathrm{Kepler}}$ are not conserved quantities in a classical Kepler orbit, but they can be combined by various conserved quantities, such as orbital energy E and orbital angular momentum $\boldsymbol{J}_{\mathrm{orb}}$. They can yield additional conserved quantities, the orbital period T and the Laplace–Runge–Lenz (LRL) vector $\boldsymbol{A}$. By defining an orthogonal frame (x, y, z) with basis vectors $\boldsymbol{e}_x$, $\boldsymbol{e}_y$, and $\boldsymbol{e}_z$, where the origin is at m_2, we align the $\boldsymbol{e}_x$ with the pericentre and set $\boldsymbol{e}_z$ perpendicular to the orbit plane (different from basis vectors $\boldsymbol{e}_X$, $\boldsymbol{e}_Y$, and $\boldsymbol{e}_Z$). In this frame, $\dot{\boldsymbol{e}}_x = \dot{\boldsymbol{e}}_y = \dot{\boldsymbol{e}}_z = \boldsymbol{0}$ in a classical Kepler orbit. These conserved quantities allow us to readily derive the df/dt and $d\mu^a/dt$.

We define the energy per unit reduced mass $\mathcal{E}$, the orbital angular momentum per unit reduced mass $\boldsymbol{h}$, and the LRL vector $\boldsymbol{A}$ as follows:

$$\mathcal{E} = \tfrac{E}{\mu} = \tfrac{v^2}{2} - \tfrac{Gm}{r}, \quad \boldsymbol{h} = \tfrac{\boldsymbol{J}_{\mathrm{orb}}}{\mu} = \boldsymbol{r} \times \boldsymbol{v}, \quad \boldsymbol{A} = \tfrac{\boldsymbol{v}\times\boldsymbol{h}}{Gm} - \tfrac{\boldsymbol{r}}{r}. \tag{A1}$$

For Newtonian gravity, we have the following orbital representation:

$$r = \frac{h^2/Gm}{1 + \sqrt{1 + \frac{2\mathcal{E}h^2}{G^2m^2}}\cos f}, \tag{A2}$$

where we can define semilatus rectum p and eccentricity e,

$$p = \frac{h^2}{Gm}, \quad e = \sqrt{1 + \frac{2\mathcal{E}h^2}{G^2m^2}}, \quad r = \frac{p}{1 + e\cos f}. \tag{A3}$$

We get $\mathcal{E}$ using the velocity expression $v^2 = \dot{r}^2 + (h/r)^2$:

$$\mathcal{E} = \frac{\dot{r}^2}{2} + \frac{h^2}{2r^2} - \frac{Gm}{r}. \tag{A4}$$

Therefore, we obtain dr/dt using equations (A3) and (A4):

$$\dot{r} = \sqrt{\frac{Gm}{p}}e\sin f. \tag{A5}$$

According to the perturbation theory, the expression of velocity $\boldsymbol{v}$ remains consistent with Kepler's original form $\boldsymbol{v}_{\mathrm{Kepler}}$:

$$\boldsymbol{v} = \boldsymbol{v}_{\mathrm{Kepler}}\ \left(f(t), \mu^a(t)\right) = \frac{\mathrm{d}}{\mathrm{d}t}(r\boldsymbol{n}) = \dot{r}\boldsymbol{n} + r\dot{f}_{\mathrm{N}}\boldsymbol{\lambda}, \tag{A6}$$

Thus, with $\boldsymbol{r} = r\boldsymbol{n}$, we give the time derivative $d\boldsymbol{n}/dt$:

$$\frac{\mathrm{d}\boldsymbol{n}}{\mathrm{d}t} = \dot{f}_{\mathrm{N}}\boldsymbol{\lambda}. \tag{A7}$$

Downloaded from https://academic.oup.com/mnras/article/543/4/3503/8287737 by guest on 06 February 2026

Substituting $\boldsymbol{v}$ into $\boldsymbol{h}$ in equation (A1), and using equation (A3), we obtain

$$\boldsymbol{h} = r^2 \dot{f}_{\rm N} \boldsymbol{\ell}, \quad \dot{f}_{\rm N} = \frac{\boldsymbol{h}\cdot\boldsymbol{\ell}}{r^2} = \sqrt{\frac{Gm}{p^3}}\,(1+e\cos f)^2\,. \tag{A8}$$

This is consistent with equation (6). In addition, the vectors $\boldsymbol{n}$, $\boldsymbol{\lambda}$, and $\boldsymbol{\ell}$ can be expressed in terms of the vectors $\boldsymbol{e}_x$, $\boldsymbol{e}_y$, and $\boldsymbol{e}_z$,

$$\begin{bmatrix}\boldsymbol{n}\\ \boldsymbol{\lambda}\\ \boldsymbol{\ell}\end{bmatrix} = \begin{bmatrix}\cos f & \sin f & 0\\ -\sin f & \cos f & 0\\ 0 & 0 & 1\end{bmatrix}\begin{bmatrix}\boldsymbol{e}_x\\ \boldsymbol{e}_y\\ \boldsymbol{e}_z\end{bmatrix}. \tag{A9}$$

Due to the orthogonality of $(\boldsymbol{n}, \boldsymbol{\lambda}, \boldsymbol{\ell})$ and $(\boldsymbol{e}_x, \boldsymbol{e}_y, \boldsymbol{e}_z)$, we can get

$$\langle \boldsymbol{n}, \dot{\boldsymbol{n}}\rangle = \left\langle \boldsymbol{\lambda}, \dot{\boldsymbol{\lambda}}\right\rangle = \left\langle \boldsymbol{\ell}, \dot{\boldsymbol{\ell}}\right\rangle \equiv 0, \tag{A10a}$$

$$\langle \boldsymbol{e}_x, \dot{\boldsymbol{e}}_x\rangle = \left\langle \boldsymbol{e}_y, \dot{\boldsymbol{e}}_y\right\rangle = \langle \boldsymbol{e}_z, \dot{\boldsymbol{e}}_z\rangle \equiv 0. \tag{A10b}$$

The LRL vector $\boldsymbol{A}$ is a eccentricity vector defined by $\boldsymbol{r}$ and $\boldsymbol{v}$:

$$\begin{aligned}\boldsymbol{A} &= \frac{\boldsymbol{v}\times\boldsymbol{h}}{Gm} - \frac{\boldsymbol{r}}{r} = \left(\frac{v^2}{Gm} - \frac{1}{r}\right)\boldsymbol{r} - \frac{\boldsymbol{r}\cdot\boldsymbol{v}}{Gm}\boldsymbol{v} \\ &= \left(\frac{r^3 \dot{f}_{\rm N}^2}{Gm} - 1\right)\boldsymbol{n} - \frac{r^2 \dot{r} \dot{f}_{\rm N}}{Gm}\boldsymbol{\lambda} = e\,(\cos f\,\boldsymbol{n} - \sin f\,\boldsymbol{\lambda}) = e\boldsymbol{e}_x.\end{aligned} \tag{A11}$$

Therefore, we can establish the relationship between orbital parameters f, p, e, ω, Ω, ι, and the conserved quantities $\boldsymbol{h}$, $\boldsymbol{A}$, $\boldsymbol{e}_x$, $\boldsymbol{e}_y$, $\boldsymbol{e}_z$ as follows:

$$\begin{aligned} &p := \frac{h^2}{Gm}, \quad \cos f := \boldsymbol{n}\cdot\boldsymbol{e}_x, \quad \sin\iota\sin\Omega := \boldsymbol{e}_z\cdot\boldsymbol{e}_X, \\ &e := A, \quad \cos\iota := \boldsymbol{e}_z\cdot\boldsymbol{e}_Z, \quad \sin\iota\sin\omega := \boldsymbol{e}_x\cdot\boldsymbol{e}_Z.\end{aligned} \tag{A12}$$

Taking the time derivative on both sides of the equations, we get

$$\begin{aligned} &\dot{e} = \dot{A}, \quad \dot{f} = -\frac{\dot{\boldsymbol{n}}\cdot\boldsymbol{e}_x + \boldsymbol{n}\cdot\dot{\boldsymbol{e}}_x}{\sin f}, \quad \dot{\omega} = \frac{(\dot{\boldsymbol{e}}_x + \cot\iota\sin\omega\,\dot{\boldsymbol{e}}_z)\cdot\boldsymbol{e}_Z}{\sin\iota\cos\omega}, \\ &\dot{p} = \frac{2h}{Gm}\dot{h}, \quad \dot{\iota} = -\frac{\dot{\boldsymbol{e}}_z\cdot\boldsymbol{e}_Z}{\sin\iota}, \quad \dot{\Omega} = \frac{\dot{\boldsymbol{e}}_z\cdot(\boldsymbol{e}_X + \cot\iota\sin\Omega\,\boldsymbol{e}_Z)}{\sin\iota\cos\Omega}.\end{aligned} \tag{A13}$$

Therefore, we now need to relate the external force $\boldsymbol{f}$ to $\dot{\boldsymbol{h}}$, $\dot{\boldsymbol{A}}$, $\dot{h}$, $\dot{A}$, $\dot{\boldsymbol{e}}_z$, and $\dot{\boldsymbol{e}}_x$. The form of $\boldsymbol{f}$ is $\boldsymbol{f} = \mathcal{R}\boldsymbol{n} + \mathcal{S}\boldsymbol{\lambda} + \mathcal{W}\boldsymbol{\ell}$. We can calculate $\dot{\boldsymbol{h}}$ and $\dot{\boldsymbol{A}}$ using equation (A1):

$$\frac{\mathrm{d}\boldsymbol{h}}{\mathrm{d}t} = \frac{\mathrm{d}\boldsymbol{r}}{\mathrm{d}t}\times\boldsymbol{v} + \boldsymbol{r}\times\frac{\mathrm{d}\boldsymbol{v}}{\mathrm{d}t} = \boldsymbol{r}\times\boldsymbol{f} = -r\,(\mathcal{S}\boldsymbol{\ell} - \mathcal{W}\boldsymbol{\lambda})\,, \tag{A14a}$$

$$\begin{aligned}\frac{\mathrm{d}\boldsymbol{A}}{\mathrm{d}t} &= \frac{\boldsymbol{a}\times(\boldsymbol{r}\times\boldsymbol{v}) + \boldsymbol{v}\times(\boldsymbol{r}\times\boldsymbol{a})}{Gm} - \left(\frac{\boldsymbol{v}}{r} - \frac{\dot{r}}{r^2}\boldsymbol{r}\right) \\ &= \frac{\boldsymbol{f}\times\boldsymbol{h} + \boldsymbol{v}\times(\boldsymbol{r}\times\boldsymbol{f})}{Gm} \\ &= \frac{1}{Gm}\left[2h\mathcal{S}\boldsymbol{n} - (h\mathcal{R} + r\dot{r}\mathcal{S})\boldsymbol{\lambda} - r\dot{r}\mathcal{W}\boldsymbol{\ell}\right] \\ &= \frac{1}{Gm}\{[2h\mathcal{S}\cos f + (h\mathcal{R} + r\dot{r}\mathcal{S})\sin f]\,\boldsymbol{e}_x \\ &\quad + [2h\mathcal{S}\sin f - (h\mathcal{R} + r\dot{r}\mathcal{S})\cos f]\,\boldsymbol{e}_y - r\dot{r}\mathcal{W}\boldsymbol{e}_z\}\,.\end{aligned} \tag{A14b}$$

We then calculate $\dot{h}$ and $\dot{A}$ using equations (A8), (A11), and (A14), along with the orthogonality condition (A10):

$$\frac{\mathrm{d}h}{\mathrm{d}t} = \frac{\mathrm{d}\boldsymbol{h}}{\mathrm{d}t}\cdot\boldsymbol{\ell} + \boldsymbol{h}\cdot\frac{\mathrm{d}\boldsymbol{\ell}}{\mathrm{d}t} = \frac{\mathrm{d}\boldsymbol{h}}{\mathrm{d}t}\cdot\boldsymbol{\ell} = r\mathcal{S}, \tag{A15a}$$

$$\begin{aligned}\frac{\mathrm{d}A}{\mathrm{d}t} &= \frac{\mathrm{d}\boldsymbol{A}}{\mathrm{d}t}\cdot\boldsymbol{e}_x + \boldsymbol{A}\cdot\frac{\mathrm{d}\boldsymbol{e}_x}{\mathrm{d}t} = \frac{\mathrm{d}\boldsymbol{A}}{\mathrm{d}t}\cdot\boldsymbol{e}_x \\ &= \frac{1}{Gm}\left[2h\mathcal{S}\cos f + (h\mathcal{R} + r\dot{r}\mathcal{S})\sin f\right].\end{aligned} \tag{A15b}$$

And calculate $\dot{\boldsymbol{e}}_z = \mathrm{d}\boldsymbol{\ell}/\mathrm{d}t$ (equation A9) and $\dot{\boldsymbol{e}}_x$ using equations (A14) and (A15):

$$\frac{\mathrm{d}\boldsymbol{e}_z}{\mathrm{d}t} = \frac{1}{h}\left(\frac{\mathrm{d}\boldsymbol{h}}{\mathrm{d}t} - \frac{\mathrm{d}h}{\mathrm{d}t}\boldsymbol{e}_z\right) = -\frac{r\,\mathcal{W}}{h}\boldsymbol{\lambda}, \tag{A16a}$$

$$\begin{aligned}\frac{\mathrm{d}\boldsymbol{e}_x}{\mathrm{d}t} &= \frac{1}{A}\left(\frac{\mathrm{d}\boldsymbol{A}}{\mathrm{d}t} - \frac{\mathrm{d}A}{\mathrm{d}t}\boldsymbol{e}_x\right) = \frac{1}{GmA}\times \\ &\quad \left\{[2h\mathcal{S}\sin f - (h\mathcal{R} + r\dot{r}\mathcal{S})\cos f]\,\boldsymbol{e}_y - r\dot{r}\mathcal{W}\boldsymbol{e}_z\right\}.\end{aligned} \tag{A16b}$$

Therefore, the equation (A13) changes to

$$\dot{p} = \tfrac{2h}{Gm} r\mathcal{S}, \tag{A17a}$$

$$\dot{e} = \tfrac{h}{Gm}\left[\sin f\mathcal{R} + \left(2\cos f + \tfrac{r\dot{r}}{h}\sin f\right)\mathcal{S}\right], \tag{A17b}$$

$$\dot{f} = \tfrac{h}{r^2} + \tfrac{h}{GmA}\left[\cos f\mathcal{R} - \left(2\sin f - \tfrac{r\dot{r}}{h}\cos f\right)\mathcal{S}\right], \tag{A17c}$$

$$\dot{\iota} = \tfrac{r}{h}\cos(\omega + f)\mathcal{W}, \tag{A17d}$$

$$\dot{\Omega} = \tfrac{r}{h}\sin(\omega + f)\csc\iota\mathcal{W}, \tag{A17e}$$

$$\begin{aligned}\dot{\omega} &= \frac{h}{GmA}\left[-\cos f\mathcal{R} + \left(2\sin f - \frac{r\dot{r}}{h}\cos f\right)\mathcal{S}\right. \\ &\quad \left. - e\cot\iota\frac{Gmr}{h^2}\left(\frac{h\dot{r}\sec\omega}{GmA} + \tan\omega\cos(\omega + f)\right)\mathcal{W}\right].\end{aligned} \tag{A17f}$$

From equations (A7) and (A16), we obtain $\mathrm{d}\boldsymbol{n}/\mathrm{d}t$ and $\mathrm{d}\boldsymbol{\ell}/\mathrm{d}t$. We can also get $d\boldsymbol{\lambda}/dt$ in terms of $\boldsymbol{e}_x = \cos f\,\boldsymbol{n} - \sin f\,\boldsymbol{\lambda}$ (equation (A9)), using $\dot{\boldsymbol{e}}_x$ (A16b), $\dot{\boldsymbol{n}}$ (A7), and $\dot{f}$ (A17c):

$$\begin{aligned}\frac{\mathrm{d}\boldsymbol{\lambda}}{\mathrm{d}t} &= -\frac{\dot{\boldsymbol{e}}_x + \dot{f}\,(\sin f\,\boldsymbol{n} + \cos f\,\boldsymbol{\lambda}) - \cos f\,\dot{\boldsymbol{n}}}{\sin f} \\ &= -\dot{f}_{\rm N}\boldsymbol{n} + \frac{r\dot{r}\mathcal{W}}{GmA}\csc f\,\boldsymbol{\ell}.\end{aligned} \tag{A18}$$

We obtain the final form in equations (4) and (5) by substituting the following expressions into equations (A17), (A7), (A18), and (A16):

$$\begin{aligned} &r = \frac{p}{1 + e\cos f}, \quad \dot{r} = \sqrt{\frac{Gm}{p}}\,e\sin f, \\ &\dot{f}_{\rm N} = \sqrt{\frac{Gm}{p^3}}\,(1 + e\cos f)^2\,, \quad h = \sqrt{Gmp}, \quad A = e.\end{aligned} \tag{A19}$$

APPENDIX B: SIMPLIFICATION OF THE MT MODEL

In this appendix, we simplify equation (13) by considering only the process of Roche lobe overflow. We cancel the first and third terms in equation (13), because the density at the Roche radius is much larger than the surface density ($\rho_{\rm L} \gg \rho_{\rm ph}$) and $K^{1/\Gamma}/e \sim F(K, \Gamma)^2$ for $\Gamma = 5/3$. We get

$$\dot{m}_1 \approx -H(\varepsilon)\frac{2\pi}{\sqrt{BC}}F(K, \Gamma)K^{\frac{3\Gamma-1}{2\Gamma}}\rho_{\rm L}^{\frac{3\Gamma-1}{2}}\,, \tag{B1}$$

where $\rho_{\rm L}$ is $\rho(\tilde{Z} = R_{\rm WD} - R_{\rm L})$ can be given by equation (9), and $2\pi/\sqrt{BC}$ can be written in series form:

$$\begin{aligned}\frac{2\pi}{\sqrt{BC}} &= \frac{2\pi D^3}{Gm_2}\frac{1}{\sqrt{\Re\,[\Re - A(1+q)]}} \\ &:= \frac{2\pi D^3}{Gm_2}\frac{1}{\sqrt{\mathcal{R}_0}}\left(\sum_{m=0}^{\infty}\mathcal{S}_m\varepsilon^m\right),\end{aligned} \tag{B2}$$

where $\Re$ is defined as

$$\Re := \frac{q}{\tilde{X}_1^3} + \frac{1}{(1 - \tilde{X}_1)^3}. \tag{B3}$$

Downloaded from https://academic.oup.com/mnras/article/543/4/3503/8287737 by guest on 06 February 2026

Here, dimensionless parameter $\tilde{X}_1$, satisfying $0 < \tilde{X}_1 \ll 1$, represents the fractional distance from the CM of the WD to the first Lagrangian point L1. The position of L1 is determined by the following equation, as presented in Sepinsky et al. (2007a):

$$\frac{q}{\tilde{X}_1{}^2} + \frac{1}{(1-\tilde{X}_1)^2} + 1 - A(1+q)\tilde{X}_1 = 0. \tag{B4}$$

Equation (9) can be organized into the following form:

$$\rho_{\mathrm{L}}^{\frac{3\Gamma-1}{2}} = \left(\frac{\Gamma-1}{K\Gamma}\frac{Gm_2}{D}C_{\mathrm{L}}\right)^{\frac{3\Gamma-1}{2(\Gamma-1)}} \left(\hat{\rho}_{\mathrm{ph}}^{\Gamma-1} + \lambda\right)^{\frac{3\Gamma-1}{2(\Gamma-1)}}, \tag{B5}$$

where $\lambda := \lambda_1 + \lambda_O := \sum_{n=1}^{\infty} D_{\varepsilon n}\varepsilon^n$, specifically $\lambda_1 = D_{\varepsilon 1}\varepsilon$. From equation (10), $\hat{\rho}_{\mathrm{ph}}^{\Gamma-1}$ can be defined as

$$\hat{\rho}_{\mathrm{ph}}^{\Gamma-1} := \left(\frac{\Gamma-1}{K\Gamma}\frac{Gm_2}{D}C_{\mathrm{L}}\right)^{-1} \rho_{\mathrm{ph}}^{\Gamma-1} = \frac{q}{C_{\mathrm{L}}^2}\frac{\xi_0}{1-\xi_0}(1-\varepsilon). \tag{B6}$$

Define α to re-express the variable $\hat{\rho}_{\mathrm{ph}}^{\Gamma-1}$,

$$\frac{q}{C_{\mathrm{L}}^2}\frac{\xi_0}{1-\xi_0} := \frac{D_{\varepsilon 1}}{1-\alpha}, \quad \text{where } \alpha := 1 - \left(\frac{q}{C_{\mathrm{L}}^2}\frac{\xi_0}{1-\xi_0}\right)^{-1} D_{\varepsilon 1}. \tag{B7}$$

We can assume that $\lambda_1 + \hat{\rho}_{\mathrm{ph}}^{\Gamma-1} \gg \lambda_O$ near pericentre. Let us define a new series to represent $\hat{\rho}_{\mathrm{ph}}^{\Gamma-1} + \lambda$,

$$\left(\lambda_1 + \hat{\rho}_{\mathrm{ph}}^{\Gamma-1} + \lambda_O\right)^{\frac{3\Gamma-1}{2(\Gamma-1)}} := \left(\sum_{n=0}^{\infty} \mathcal{U}_{\varepsilon n}\varepsilon^n\right). \tag{B8}$$

We can take a first-order expand with respect to λ_O:

$$\begin{aligned}\left(\sum_{n=1}^{\infty} \mathcal{U}_{\varepsilon n}\varepsilon^n\right) &\simeq \left(D_{\varepsilon 1}\frac{1-\alpha\varepsilon}{1-\alpha}\right)^{\frac{3\Gamma-1}{2(\Gamma-1)}} \left(1 + \frac{3\Gamma-1}{2(\Gamma-1)}\frac{\lambda_O}{\lambda_1 + \hat{\rho}_{\mathrm{ph}}^{\Gamma-1}}\right),\\ \frac{\lambda_O}{\lambda_1 + \hat{\rho}_{\mathrm{ph}}^{\Gamma-1}} &= \left(D_{\varepsilon 1}\frac{1-\alpha\varepsilon}{1-\alpha}\right)^{-1}\left(\sum_{n=2}^{\infty} D_{\varepsilon n}\varepsilon^n\right).\end{aligned} \tag{B9}$$

Therefore, the coefficient $\mathcal{U}_{\varepsilon n}$ are given analytically.

We define $\mathcal{S}_0 \equiv 1$, so that $\mathcal{R}_0$ is the zeroth-order approximation of $\Re\,[\Re - A(1+q)]$ with respect to ε. When $q \ll 1$, the simplest solution to equation (B4) for $\tilde{X}_1$ is

$$\tilde{X}_1 \simeq \left(\frac{q}{2 + A(1+q)}\right)^{1/3} = \left(\frac{q}{2 + \varpi(1-\varepsilon)^3}\right)^{1/3}. \tag{B10}$$

Substitute $\tilde{X}_1$ into equation (B3), we obtain $\mathcal{R}_0$:

$$\begin{aligned}\mathcal{R}_0 \simeq &\left[2 + \left(1 - \left(\frac{q}{2+\varpi}\right)^{1/3}\right)^{-3}\right] \times\\ &\left[2 + \varpi + \left(1 - \left(\frac{q}{2+\varpi}\right)^{1/3}\right)^{-3}\right].\end{aligned} \tag{B11}$$

Here, dimensionless ϖ is

$$\begin{aligned}\varpi &= C_{\mathrm{L}}^{-3}\left(\frac{R_{\mathrm{WD}}\Omega_1}{c}\right)^2\left(\frac{GM_{\mathrm{IMBH}}}{c^2 R_{\mathrm{WD}}}\right)^{-1}\\ &\simeq \frac{5}{4896}\frac{q}{C_{\mathrm{L}}^3}\frac{M_{\mathrm{WD}}^{4/3}}{M_{\odot}M_{\mathrm{Ch}}^{1/3}}\left(\frac{\chi_1}{\tilde{\gamma}}\right)^2,\end{aligned} \tag{B12}$$

where $\tilde{\gamma}$ the difference between the WD's moment of inertia and that of a uniform-density sphere. It can be related to $\boldsymbol{S}_1$:

$$|\boldsymbol{S}_1| := \frac{GM_{\mathrm{WD}}^2}{c}\chi_1 := \frac{2}{5}\tilde{\gamma}M_{\mathrm{WD}}R_{\mathrm{WD}}^2\Omega_1. \tag{B13}$$

With $\mathcal{R}_0$ in equation (B11), we can calculate $\mathcal{S}_m$ from equation (B2). Taking the first-order expand of $\mathcal{S}_m$ about ϖ gives a simple expression:

$$\mathcal{S}_0 \simeq 1,\ \mathcal{S}_1 \simeq \frac{3}{4}\varpi Q,\ \mathcal{S}_2 \simeq -\frac{3}{4}\varpi Q,\ \mathcal{S}_3 \simeq \frac{1}{4}\varpi Q,\ \mathcal{S}_4 \simeq \mathcal{O}(\varpi^2),$$

where

$$Q = \frac{4 - 10\times 2^{2/3}q^{1/3} + 12\times 2^{1/3}q^{2/3} - 8q + 2^{2/3}q^{4/3}}{6 - 9\times 2^{2/3}q^{1/3} + 12\times 2^{1/3}q^{2/3} - 8q + 2^{2/3}q^{4/3}} \simeq \frac{2}{3}.$$

Thus, $\mathcal{S}_m$ are entirely influenced by the spin of the WD.

Next, we only need to calculate the $\sum_{n=1}^{\infty} D_{\varepsilon n}\varepsilon^n$. Since λ is given by equation (9), we have

$$\begin{aligned}\lambda = \left(\tfrac{Gm_2}{D}C_{\mathrm{L}}\right)^{-1}\Big\{&\tfrac{Gm_1}{R_{\mathrm{WD}}}\left(\tfrac{R_{\mathrm{WD}}}{R_{\mathrm{WD}}-\tilde{Z}} - 1\right) - \tfrac{1}{2}\Omega_1^2(2R_{\mathrm{WD}} - \tilde{Z})\tilde{Z}\\ &+ \tfrac{Gm_2}{D}\left[\tfrac{\tilde{Z}}{D} + \tfrac{D}{D-R_{\mathrm{WD}}+\tilde{Z}} - \tfrac{D}{D-R_{\mathrm{WD}}}\right]\Big\}.\end{aligned} \tag{B14}$$

where $\tilde{Z} = R_{\mathrm{WD}} - C_{\mathrm{L}}D = R_{\mathrm{WD}}\varepsilon$. Thus, λ can be expressed as

$$\begin{aligned}\lambda = \sum_{n=1}^{\infty} D_{\varepsilon n}\varepsilon^n &= \frac{q}{C_{\mathrm{L}}}\varepsilon - \frac{\varpi C_{\mathrm{L}}}{2}(2-\varepsilon)(1-\varepsilon)\varepsilon\\ &+ \frac{\varepsilon}{1-\varepsilon}\left[1 - \frac{1-\varepsilon}{(1-\varepsilon-C_{\mathrm{L}})(1-C_{\mathrm{L}})}\right].\end{aligned} \tag{B15}$$

Therefore, $D_{\varepsilon n}$ is given by

$$D_{\varepsilon n} = 1 - \frac{1}{(1-C_{\mathrm{L}})^{n+1}} + \frac{q}{C_{\mathrm{L}}{}^2}\delta_{n1} - \frac{\varpi C_{\mathrm{L}}}{2}(2\delta_{n1} - 3\delta_{n2} + \delta_{n3}). \tag{B16}$$

APPENDIX C: TRANSFERRED MASS FOR EVERY ORBITAL PERIOD

Following Appendix B, we adopt a simplified form for $\dot{m}_1$:

$$\dot{m}_1 := C_{\dot{m}_1}\sum_{n=0}^{\infty} C_{\varepsilon n}\varepsilon^n, \tag{C1}$$

where $C_{\dot{m}_1}$ and $C_{\varepsilon n}$ are defined as

$$C_{\dot{m}_1} = -2\pi W(K,\Gamma)\cdot(GM_{\mathrm{IMBH}})^2 C_{\mathrm{L}}^3/\sqrt{\mathcal{R}_0}, \tag{C2a}$$

$$\textstyle\sum_{n=0}^{\infty} C_{\varepsilon n}\varepsilon^n = \left(\sum_{m=0}^{\infty}\mathcal{S}_m\varepsilon^m\right)\left(\sum_{n=0}^{\infty}\mathcal{U}_{\varepsilon n}\varepsilon^n\right). \tag{C2b}$$

We can express the integral of $\dot{m}_1$ for a Keplerian elliptical orbit:

$$\int_{-\pi}^{\pi}\dot{m}_1\dot{f}_{\mathrm{N}}^{-1}\mathrm{d}f = C_{\dot{m}_1}\sqrt{\frac{p^3}{Gm}}\sum_{n=0}^{\infty}C_{\varepsilon n}\int_{-f_0}^{f_0}\frac{\varepsilon^n\mathrm{d}f}{(1+e\cos f)^2}. \tag{C3}$$

Here, ε^n can be rewritten as a function of the angle f:

$$\begin{aligned}\varepsilon^n &= \left(1 - \frac{pC_{\mathrm{L}}}{R_{\mathrm{WD}}}\frac{1}{1+e\cos f}\right)^n\\ &= \sum_{m=0}^{n}\binom{n}{m}\left(-\frac{pC_{\mathrm{L}}}{R_{\mathrm{WD}}}\right)^m\frac{1}{(1+e\cos f)^m}.\end{aligned} \tag{C4}$$

Therefore, δM_{WD} can be written as

$$\begin{aligned}\delta M_{\mathrm{WD}} = &\ C_{\dot{m}_1}\sqrt{\frac{p^3}{Gm}}\sum_{n=0}^{\infty}C_{\varepsilon n}\times\\ &\left[\sum_{m=0}^{n}\binom{n}{m}\left(-\frac{pC_{\mathrm{L}}}{R_{\mathrm{WD}}}\right)^m\int_{-f_0}^{f_0}\frac{df}{(1+e\cos f)^{m+2}}\right].\end{aligned} \tag{C5}$$

The integration result is the Appell Hypergeometric Function AF1$(\alpha;\beta,\beta';\gamma;x,y)$ of two variables, with a series definition

Downloaded from https://academic.oup.com/mnras/article/543/4/3503/8287737 by guest on 06 February 2026

(Olver et al. 2010):

$$\mathrm{AF1}(\alpha;\beta,\beta';\gamma;x,y)=\sum_{m=0}^{\infty}\sum_{n=0}^{\infty}\frac{(\alpha)_{m+n}(\beta)_m(\beta')_{(n)}}{(\gamma)_{m+n}\,m!\,n!}x^m y^n, \tag{C6}$$

where $(q)_n$ denotes the Pochhammer symbol. The integral evaluates to

$$\int_{-f_0}^{f_0}\frac{\mathrm{d}f}{(1+e\cos f)^{m+2}}=\frac{4}{(1+e)^{m+2}}\sin\left(\frac{f_0}{2}\right)\times \tag{C7}$$
$$\mathrm{AF1}\left[\frac{1}{2};\frac{1}{2},m+2;\frac{3}{2};\sin^2\left(\frac{f_0}{2}\right),\frac{2e}{1+e}\sin^2\left(\frac{f_0}{2}\right)\right].$$

Thus, we require the value of $\sin(f_0/2)$. Since we substitute D with $p/(1+e\cos f)$, f_0 satisfies $R_{\mathrm{WD}}=C_{\mathrm{L}}D(f_0)$. To relate p and R_{WD}, we use ϵ as defined in Section 5.1.1:

$$r_{\mathrm{p}}=\frac{p}{1+e}:=(1-\epsilon)\frac{R_{\mathrm{WD}}}{C_{\mathrm{L}}}. \tag{C8}$$

Therefore, f_0 and $\sin(f_0/2)$ can be written as

$$f_0=\sin^{-1}\left[\sqrt{1-\left(1-\frac{1+e}{e}\epsilon\right)^2}\right], \tag{C9}$$

$$\sin\left(\frac{f_0}{2}\right)=\sin\left\{\frac{1}{2}\sin^{-1}\left[\sqrt{1-\left(1-\frac{1+e}{e}\epsilon\right)^2}\right]\right\}\equiv\sqrt{\frac{1+e}{2e}\epsilon}.$$

Substituting $\sin(f_0/2)$ into equation (C7) yields equation (38).

In Schwarzschild space–time, $dt/d\psi$ can be used to substitute $\dot{f}_{\mathrm{N}}^{-1}$ (Cutler et al. 1994; Martel 2004). The primary geodesic equation is

$$\frac{\mathrm{d}t}{\mathrm{d}\psi}=\frac{Gm}{c^3}\frac{\hat{p}^{3/2}}{\hat{x}^2}\frac{\hat{p}\sqrt{\hat{p}-4}}{(\hat{p}-2\hat{x})\sqrt{\hat{p}-4-2\hat{x}}}\sqrt{1+\frac{4(1-e^2)}{\hat{p}(\hat{p}-4)}}, \tag{C10}$$

where $\hat{p}:=p/(Gm/c^2)$ and $\hat{x}:=1+e\cos\psi$ are dimensionless quantities. The pericentre r_{p}, apocentre r_{a}, eccentricity e are defined as

$$r_{\mathrm{p}}=\frac{Gm}{c^2}\frac{\hat{p}}{1+e},\quad r_{\mathrm{a}}=\frac{Gm}{c^2}\frac{\hat{p}}{1-e},\quad e=\frac{r_{\mathrm{a}}-r_{\mathrm{p}}}{r_{\mathrm{a}}+r_{\mathrm{p}}}. \tag{C11}$$

Equation (C8) remains valid. The integral variable in equation (C3) is changed from f to ψ, with ψ_0 satisfying equation (C9). For $\hat{x}\to 0$, a Taylor expansion of equation (C10) is

$$\frac{\hat{p}\sqrt{\hat{p}-4}}{(\hat{p}-2\hat{x})\sqrt{\hat{p}-4-2\hat{x}}}:=\sum_{k=0}^{\infty}F_k(\hat{p})\hat{x}^k,\quad \text{where}\quad F_0=1. \tag{C12}$$

Transferred mass δM_{WD} in equation (C5) then becomes

$$\delta M_{\mathrm{WD}}=\sum_{k=0}^{\infty}\left[F_k(\hat{p})C_{\dot{m}_1}\frac{Gm}{c^3}\hat{p}\sqrt{\frac{(\hat{p}-2)^2-4e^2}{\hat{p}-4}}\times \right. \tag{C13}$$
$$\left.\sum_{n=0}^{\infty}C_{\varepsilon\mathrm{n}}\sum_{m=0}^{n}\binom{n}{m}\left(-\frac{Gm}{c^2}\frac{\hat{p}C_{\mathrm{L}}}{R_{\mathrm{WD}}}\right)^m\int_{-\psi_0}^{\psi_0}\frac{d\psi}{\hat{x}^{(m-k)+2}}\right].$$

We continue using equation (C7) for the integral, so equation (C13) reduces to equation (49).

APPENDIX D: EQUIVALENCE OF PHASE AND PERIOD EVOLUTION IN THE ADIABATIC APPROXIMATION

As described in Section 6, our objective is to detect the cumulative phase shift Δu between systems with and without MT over a finite observation time t_{obs}. Importantly, an exact integration of the orbital phase evolution is not required; rather, an estimate of the orbital period for each cycle suffices for our analysis.

We adopt the standard formalism for eccentric Keplerian orbits. Specifically, we express the true anomaly $f(t)$ as a function of the eccentric anomaly u, where the radial distance is given by $r=a(1-e\cos u)$, and the time evolution is governed by Kepler's equation: $2\pi(t-t_{\mathrm{p}})/T=u-e\sin u$, with $t_{\mathrm{p}}\leq t$ denoting the time of the most recent pericentre passage. The GW waveform $h(f(t))$, initially expressed in terms of the true anomaly f, can be reparametrized in terms of u. Therefore, evaluating the GW phase shift $\Delta f(t)$ is equivalent to computing $\Delta u(t)$. The relation between u and t can be expanded using a Fourier series involving Bessel functions of the first kind $J_n(x)$ (Murray & Dermott 2000):

$$u(t,\mathrm{N})\simeq 2\pi(\mathrm{N}-1)+l_{\mathrm{N}}+\mathcal{J}(l_{\mathrm{N}},e_{\mathrm{N}}), \tag{D1}$$

where

$$l_{\mathrm{N}}:=2\pi\left(t-t_{\mathrm{pN\text{-}1}}\right)/T_{\mathrm{N}},\quad t_{\mathrm{pN\text{-}1}}:=\sum_{\mathrm{k}=1}^{\mathrm{N}-1}T_{\mathrm{k}}, \tag{D2}$$

$$\mathcal{J}(l_{\mathrm{N}},e_{\mathrm{N}}):=\sum_{n=1}^{\infty}\frac{2}{n}J_n(ne_{\mathrm{N}})\sin nl_{\mathrm{N}}. \tag{D3}$$

Here, e_{N} and T_{N} represent the eccentricity and period of the Nth cycle, and $\mathcal{J}(l_{\mathrm{N}}(t),e_{\mathrm{N}})$ represent the non-linear part of the phase evolution caused by eccentricity. Assuming e_{k} and T_{k} are approximately constant within the kth cycle, the Bessel functions show the difference between elliptical and circular orbits.

However, the phase difference $\Delta u(t)$ is not increase monotonically according to the Bessel function. It suddenly increases near pericentre and decreases slowly near apocentre, but satisfies $u(t_{\mathrm{pN}})-u(t_{\mathrm{pN\text{-}1}})=2\pi$. The phase difference $\Delta u(t)$ does not capture the overall effect of the phase change. When $\left[u(t,\mathrm{N})-u(t_{\mathrm{pN}},\mathrm{N})\right]/u(t_{\mathrm{pN}},\mathrm{N})\ll 1$ (i.e. the phase difference near the pericentre), we disregard the series of Bessel functions, yielding

$$\frac{u(t,\mathrm{N})}{2\pi}\simeq\mathrm{N}-1+\left(t-t_{\mathrm{pN\text{-}1}}\right)/T_{\mathrm{N}}. \tag{D4}$$

The phase difference with and without the MT process is

$$\frac{\Delta u}{2\pi}\simeq t\left(\frac{1}{T_{\mathrm{N}}}-\frac{1}{T_{\mathrm{N}}^*}\right)-\left(\frac{t_{\mathrm{pN\text{-}1}}}{T_{\mathrm{N}}}-\frac{t_{\mathrm{pN\text{-}1}}^*}{T_{\mathrm{N}}^*}\right)<0, \tag{D5}$$

where the superscript asterisk indicates that MT process is not considered. Since the $\left\langle\dot{T}_{\mathrm{MT}}^{\mathcal{B}}\right\rangle_{\mathrm{sec}}$ in equation (41) is positive, the MT process leads to a cumulative increase in the orbital period over successive cycles, $T_{\mathrm{N}}\geq T_{\mathrm{N}}^*$ and $t_{\mathrm{pN}}\geq t_{\mathrm{pN}}^*$ always holds.

Therefore, the inequality about the phase difference $\Delta u_g<0$ and equation about required time t_g for our goal (i.e. $\Delta u(t_g)=\Delta u_g$) are

$$\frac{t_{\mathrm{pN\text{-}1}}-t_{\mathrm{pN\text{-}1}}^*}{T_{\mathrm{N}}^*}\leq\frac{\left|\Delta u_g\right|}{2\pi}\leq\frac{t_{\mathrm{pN}}-t_{\mathrm{pN}}^*}{T_{\mathrm{N+1}}^*}, \tag{D6a}$$

$$t_g\left(\frac{1}{T_{\mathrm{N}}}-\frac{1}{T_{\mathrm{N}}^*}\right)-\left(\frac{t_{\mathrm{pN\text{-}1}}}{T_{\mathrm{N}}}-\frac{t_{\mathrm{pN\text{-}1}}^*}{T_{\mathrm{N}}^*}\right)=-\frac{\left|\Delta u_g\right|}{2\pi}. \tag{D6b}$$

For the orbits discussed in Section 5.2, Inequality (D6a) yields a unique integer value for N. Substituting this into equation (D6b) gives the required time t_g. For $\mathrm{N}\gg 1$, $t_g\simeq t_{\mathrm{pN}-1}\simeq t_{\mathrm{pN}-1}^*$. This is the equivalence of phase and periodic changes that we want.

In order to better clarify the meaning of equation (D6), we define $T_{\mathrm{k}}^*:=T_{\mathrm{k}}(1-\varsigma_{\mathrm{k}})<T_{\mathrm{k}}$ and $t_{\mathrm{pN\text{-}1}}\leq t_g:=(1+\lambda_g)t_{\mathrm{pN\text{-}1}}\leq t_{\mathrm{pN}}$. Here, λ_g

Downloaded from https://academic.oup.com/mnras/article/543/4/3503/8287737 by guest on 06 February 2026

represents the difference between $t_{\mathrm{pN\text{-}1}}$ and t_g. From equation (D6b) and the condition $t_{\mathrm{pN\text{-}1}} \le t_g \le t_{\mathrm{pN}}$, we obtain an inequality for λ_g:

$$0 \le \lambda_g = \left(\frac{\left|\Delta u_g\right|}{2\pi} \frac{1-\varsigma_{\mathrm{N}}}{\varsigma_{\mathrm{N}}} - \frac{\sum_{\mathrm{k}=1}^{\mathrm{N}-1} T_{\mathrm{k}} \varsigma_{\mathrm{k}}}{T_{\mathrm{N}} \varsigma_{\mathrm{N}}} \right) \frac{T_{\mathrm{N}}}{t_{\mathrm{pN\text{-}1}}} < \frac{T_{\mathrm{N}}}{t_{\mathrm{pN\text{-}1}}}. \tag{D7}$$

From Inequality (D7), a unique integer N can be determined, which corresponds to the closest value satisfying $\sum_{\mathrm{k}=1}^{\mathrm{N}-1} T_{\mathrm{k}} \varsigma_{\mathrm{k}} / \left[T_{\mathrm{N}}(1-\varsigma_{\mathrm{N}})\right] \simeq \left|\Delta u_g\right| / 2\pi$. If $T_{\mathrm{N}} \ll t_{\mathrm{pN\text{-}1}}$, the factor λ_g can be neglected, and t_g can be replaced with $t_{\mathrm{pN\text{-}1}}$ for the calculation. Solving for N then reduces to finding the unique value of N in Inequality (43).

This paper has been typeset from a TEX/LATEX file prepared by the author.

Downloaded from https://academic.oup.com/mnras/article/543/4/3503/8287737 by guest on 06 February 2026

© The Author(s) 2025.
Published by Oxford University Press on behalf of Royal Astronomical Society. This is an Open Access article distributed under the terms of the Creative Commons Attribution License (https://creativecommons.org/licenses/by/4.0/), which permits unrestricted reuse, distribution, and reproduction in any medium, provided the original work is properly cited.